

POLITECNICO
MILANO 1863

Launch Systems

AA 2024-2025

Professor: Filippo Maggi

Multidisciplinary Design Optimization of a Reusable Airborne Launcher

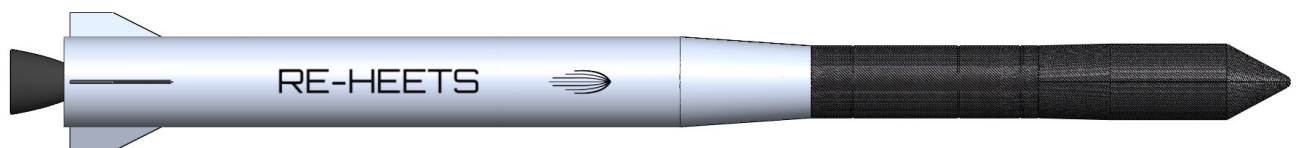
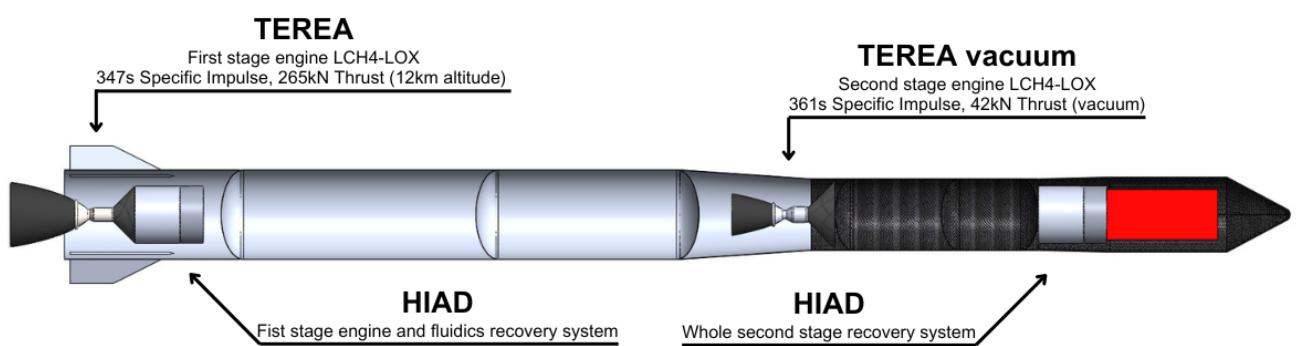
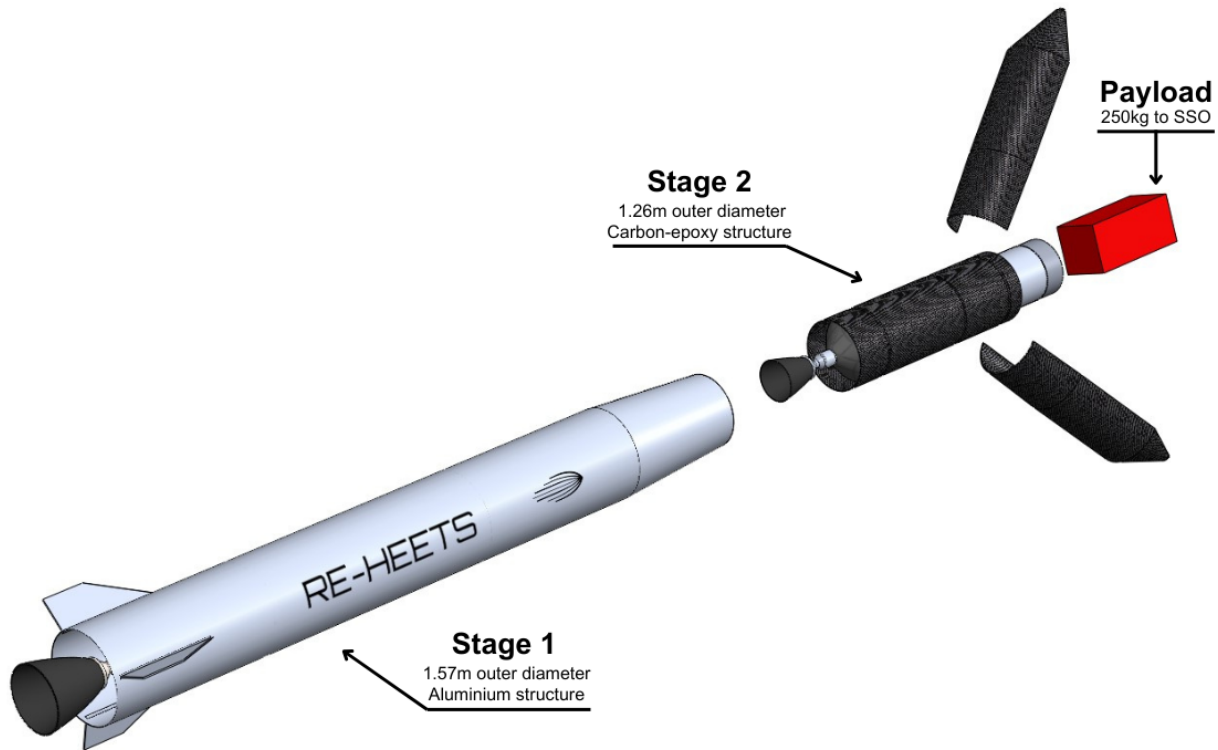
| Person Code | Surname | Name |
|-------------|-----------------|-----------------|
| 10710744 | Bellini | Davide |
| 10795356 | Frassinella | Luca |
| 10706185 | Mensi Weingrill | Edoardo |
| 10973642 | Separovic | Tomislav Marko |
| 10730683 | Nuccio | Gabriele |
| 10737865 | De Marco | Mattia |
| 10728962 | Modelli | Simone |
| 10990413 | Massini | Alessandro |
| 10726898 | Juvara | Matteo Giovanni |
| 10765536 | Mirri | Pietro |

Abstract

This paper presents the design of a reusable airborne launcher through a Multidisciplinary Design Optimization (MDO) process.

The work begins with an extensive state of the art that provides a comprehensive database of data to establish a consistent and accurate baseline. The design process is initiated by presenting the requirements and context of airborne launch. The MDO method employed is outlined, highlighting the design choices and constraints. The preliminary design steps of the launcher are explained in detail, covering essential aspects such as propulsion, structural sizing, aerodynamics, and trajectory optimization. Particular attention is given to the recovery of both the first and second stages. Structural loads and stability are iteratively assessed throughout the design process.

Results are critically analyzed using performance metrics, like profitability and reusability, to ensure that the proposed solutions meet both engineering requirements and the demands of the space launcher market.



Contents

| | | |
|----------|---|-----------|
| 1 | Introduction | 1 |
| 2 | State of the Art | 2 |
| 2.1 | Air Launch To Orbit | 2 |
| 2.2 | Recovery | 2 |
| 2.3 | Multidisciplinary Design Optimization | 3 |
| 2.3.1 | MDO State Of The Art | 4 |
| 3 | Scenario Definition | 5 |
| 3.1 | Mission Requirements and House of Quality | 5 |
| 3.1.1 | Requirements definition | 5 |
| 3.1.2 | House of Quality | 6 |
| 3.2 | Fairing Design and Payload Accommodation | 6 |
| 3.3 | Carrier Aircraft | 7 |
| 3.4 | Launch Location & Deployment Conditions | 7 |
| 4 | Technical Approach | 8 |
| 4.1 | Baseline Approach | 8 |
| 4.1.1 | Configurations choice | 8 |
| 4.2 | MDO Approach | 9 |
| 4.2.1 | LVD problem formulation | 9 |
| 4.2.2 | Block Scheme Definition | 11 |
| 4.3 | Propulsion System | 11 |
| 4.4 | Estimation of Masses and Dimensions | 12 |
| 4.5 | Aerodynamics and Stability | 13 |
| 4.5.1 | Aerodynamics | 13 |
| 4.5.2 | Stability | 14 |
| 4.6 | Trajectory | 15 |
| 4.6.1 | Powered Explicit Guidance | 15 |
| 4.6.2 | Trajectory Optimization | 16 |
| 4.6.3 | Possible Orbits | 16 |
| 4.6.4 | Monte Carlo Analysis | 17 |
| 4.7 | Structural Analysis | 17 |
| 4.7.1 | Loads Estimation | 17 |
| 4.7.2 | Finite Element Analysis | 18 |
| 4.8 | Recovery System | 18 |
| 4.9 | Optimal Configuration Choice | 20 |
| 4.9.1 | Key Performance Indexes | 20 |
| 4.9.2 | Pareto Optimal Solution | 21 |
| 5 | Results | 22 |
| 5.1 | MDO results | 22 |
| 5.2 | Final Configuration | 22 |
| 5.3 | Propulsion Results | 24 |
| 5.4 | Aerodynamic Results | 24 |
| 5.5 | Stability Results | 24 |
| 5.6 | Trajectory Results | 25 |
| 5.7 | Structure Results | 26 |
| 5.7.1 | Finite Element Analysis | 27 |
| 5.8 | Recovery Results | 27 |
| 5.9 | Final Sizing Results | 28 |

| | |
|--|-----------|
| 6 Analysis Of Results and Requirements Compliance | 29 |
| 7 Conclusions and Further Developments | 30 |
| Appendix | i |
| A House Of Quality | i |
| B Baseline Appendix | i |
| B.1 Decision Matrix | i |
| B.2 ΔV Preliminary Estimation | ii |
| C MDO Appendix | ii |
| C.1 Inputs | ii |
| C.2 Configuration ID Bounds | iv |
| C.3 Results | v |
| C.4 Block Scheme Definition | vi |
| D Propulsion System Appendix | vi |
| E Masses estimation Appendix | vii |
| E.1 MER | vii |
| E.2 Centres of mass | x |
| F Aerodynamics Appendix | xii |
| F.1 C_N computation: | xii |
| F.2 C_A computation: | xii |
| F.3 Validation of the body alone geometry aerodynamics | xiv |
| F.4 Body wing tail NKP method | xviii |
| G Stability Appendix | xix |
| H Trajectory Appendix | xix |
| H.1 Power Explicit Guidance | xx |
| I Structures System Appendix | xxii |
| I.1 Thickness Sizing Procedure | xxii |
| J Recovery Appendix | xxiii |
| J.1 HIAD | xxiii |
| J.2 Parachute Recovery | xxviii |
| J.3 Results | xxx |
| K Validation of subsystems Appendix | xxxi |
| K.1 Propulsion system | xxxi |
| K.2 Estimation of masses and dimensions | xxxi |
| L KPI Appendix | xxxii |
| M Authorship Declaration | xli |

List of Figures

| | | |
|------|---|----|
| 3.1 | Geometric guidelines given by NASA ^[1] | 6 |
| 4.1 | Block scheme of the system | 11 |
| 5.1 | MDO configurations | 22 |
| 5.2 | Pareto Plot | 23 |
| 5.3 | Lift Coefficient vs angle of attack | 24 |
| 5.4 | Lift to Drag ratio vs angle of attack | 24 |
| 5.5 | Nominal trajectory pitch | 25 |
| 5.6 | Nominal trajectory altitude | 25 |
| 5.7 | Nominal trajectory vertical velocity | 25 |
| 5.8 | Nominal trajectory horizontal velocity | 25 |
| 5.9 | Possible orbits with full reusability | 26 |
| 5.10 | Orbits discarding the second stage | 26 |
| 5.11 | Axial Force and Bending Moment estimation | 26 |
| 5.12 | Axial Force and Bending Moment with FEM analysis | 26 |
| 5.13 | Displacements and stresses map on the rocket | 27 |
| 5.14 | Maximum Von Mises stresses | 27 |
| 5.15 | Acceleration perceived by the first stage | 27 |
| 5.16 | Acceleration perceived by the second stage | 27 |
| 6.1 | Remaining propellant mass of monte carlo population | 29 |

Appendix Figures

| | | |
|----|--|--------|
| 1 | House Of Quality, Re-Heets Launcher | i |
| 2 | Block Scheme | vi |
| 3 | Thrust of 1 st stage as function of altitude | vii |
| 4 | Specific Impulse of 1 st stage as function of altitude | vii |
| 5 | Preliminary dimensions | x |
| 6 | Shapes for local CM position calculations | x |
| 7 | Crossflow drag coefficient as a function of crossflow Mach number | xii |
| 8 | C_A body for Conical nose with $l_N/d = 3$ and $l_A/d = 8$ | xiv |
| 9 | C_N body for Conical nose with $l_N/d = 3$ and $l_A/d = 8$ | xv |
| 10 | C_A body for Tangent ogive nose with $l_N/d = 3$ and $l_A/d = 6$ | xv |
| 11 | C_N body for Tangent ogive nose with $l_N/d = 3$ and $l_A/d = 6$ | xvi |
| 12 | C_D body and correction for blunt nose with $l/d = 8.91$ | xvi |
| 13 | C_L for the Pegasus launcher body-wing-tail | xvii |
| 14 | C_D vs C_L for the Pegasus launcher body-wing-tail | xviii |
| 15 | Stability Baseline | xix |
| 16 | Example of tail geometry alternatives | xix |
| 17 | Vectors and angles for the azimuth | xix |
| 18 | Possible orbits with no reusability | xix |
| 19 | First stage trajectory angle of attack | xx |
| 20 | First stage Mach number | xx |
| 21 | Launcher Ground Track | xx |
| 22 | Stages recovery CAD models for different configurations and perspectives. (not in scale one in respect to the other) | xxvii |
| 23 | HIADs integrated in the launcher | xxviii |
| 24 | First stage HIAD recovery system detach. | xxviii |
| 25 | Heat flux absorbed by the first stage | xxx |
| 26 | Heat flux absorbed by the second stage | xxx |

| | | |
|----|---|-------|
| 27 | Speed in time of the first stage | xxx |
| 28 | Speed in time of the second stage | xxx |
| 29 | Altitude in time of the first stage | xxxi |
| 30 | Altitude in time of the second stage | xxxi |
| 31 | Table of emissions for different propellant couples | xxxiv |
| 32 | Break Even Point | xxxv |

List of Tables

| | | |
|-----|--|----|
| 3.1 | High level requirements and design influences | 5 |
| 3.2 | Boeing 747-400F Specifications ^[2] | 7 |
| 4.1 | Configurations | 9 |
| 4.2 | Inequality constraints | 10 |
| 4.3 | MERs for tanks | 12 |
| 5.1 | Configurations Optimization Variables | 22 |
| 5.2 | KPI Configuration 12 | 23 |
| 5.3 | Final Configuration optimal variables | 23 |
| 5.4 | Propulsion results: optimal condition for second stage is vacuum | 24 |
| 5.5 | Stability results | 24 |
| 5.6 | Final Launcher Design Results | 28 |
| 5.7 | Overall Mass and Structural Mass indexes | 28 |

Appendix Tables

| | | |
|----|--|-------|
| 1 | Propellant couple decision matrix | ii |
| 2 | Materials decision matrix | ii |
| 3 | Constant Input Parameters for the LVD | iii |
| 4 | Inputs for each configuration. | iv |
| 5 | Bounds for Configuration ID1, ID2, ID3, and ID4 | iv |
| 6 | Bounds for Configuration ID5, ID6, ID7, and ID8 | iv |
| 7 | Bounds for Configuration ID9, ID10, ID11, and ID12 | v |
| 8 | Configurations Optimization Variables | v |
| 9 | Merlin 1C Data ^{[3][4]} | vii |
| 10 | Validation of propulsion block | vii |
| 11 | MERs for tanks | viii |
| 12 | Shrinkage addictions | viii |
| 13 | Insulation mass for cryogenic propellants | viii |
| 14 | Local CM for components | xi |
| 15 | HIAD values used in the sizing | xxiv |
| 16 | Parachute values used in the sizing | xxix |
| 17 | Merlin 1C Data ^{[3][4]} | xxxii |
| 18 | Validation of propulsion block | xxxii |
| 19 | Turnaround times for different configurations. | xxxii |
| 20 | Prices per kg of various materials and propellants. | xxxii |
| 21 | Time to Market KPI for different configurations based on fuel and material combinations. | xxxiv |

Acronyms

B_r Bluntness Ratio
 ε Expansion Ratio

AAO All At Once
ADCS Attitude Determination and Control Subsystem
AoA Angle of Attack

BEP Break Even Point

CoG Centre of Gravity
CoM Centre of Mass

F-TPS Flexible Thermal Protection Structure

GA Genetic Algorithm
GF Gradient Free
GLOM Gross Lift-Off Mass

HEART High-Energy Atmospheric Re-entry Test
HIAD Hypersonic Inflatable Aerodynamic Decelerators
HoQ House of Quality
HULA HIAD United Launch Alliance

IATA International Air Transport Association
IDF Individual Discipline Feasible
IMU Inertial Measurement Unit
IRVE Inflatable Re-entry Vehicle Experiment
IRVE-3 Inflatable Re-entry Vehicle Experiment 3
ISS International Space Station

KPIs Key Performance Indexes

LCH4 Liquid Methane
LEO Low-Earth Orbit
LH2 Liquid hydrogen
LOX Liquid Oxygen
LVD Launch Veichle Design

MAR Mid-Air Retrieval
MDA Multidisciplinary Analysis
MDF Multi Discipline Feasible
MDO Multidisciplinary Design Optimization
MER Mass Estimation Relation

NASA National Aeronautics and Space Administration

OF Oxidizer to Fuel Ratio

PAF Payload Attach Fitting
PEG Power Explicit Guidance

ROI Return On Investment
RP-1 Rocket Propellant 1
SLVs Small Launch Vehicles
SMART Sensible Modular Autonomous Return Technology

SSO Sun-Synchronous Orbit

TEREA Turbo-fed Engine for Reusable and efficient Ascent

TRL Technology Readiness Level

TVC Thrust Vector Control

ULA United Launch Alliance

1 Introduction

This report presents the design process and analysis of a Low-Earth Orbit (LEO) airborne launcher, with a particular focus on reusability and sustainability.

Airborne launchers are gaining attention as an innovative approach to providing cost-effective and flexible access to space. By leveraging air-based deployment strategies, they offer significant advantages in optimizing launch trajectories, increasing mission flexibility, and reducing dependence on extensive ground infrastructure. These features make them a key area of interest in the evolving landscape of space technologies.

The study begins with an in-depth review of existing literature and industry practices, forming the foundation for subsequent design and analysis efforts. The investigation first addresses the state of the art in air-launch-to-orbit systems, highlighting the capabilities and limitations of the few existing technologies. It then extends to reusable launchers and emerging trends in rocket design, including advancements in materials and propulsion systems, as well as the evolving demands of the commercial space market. This comprehensive analysis identifies critical challenges and opportunities, serving as a roadmap for the development process.

Significant emphasis is placed on core design elements, including structural optimization, propellant selection, and recovery system integration. These parameters are in-depth examined using a multidisciplinary approach, enabling the exploration of alternative solutions while addressing the requirements efficiently. The analysis provides valuable insights into the trade-offs between performance, cost, TRLs and reusability. This guides the selection of configurations that best align with mission objectives and customer needs.

In addition, the report details the methodology adopted for evaluating performance metrics such as trajectory optimization, payload capacity, and recovery efficiency. Particular attention is given to the integration of reusable technologies, which represent a cornerstone of the next-future of the space industry. The rationale behind critical design choices is carefully articulated to provide an overview of the decision-making process and to underline the strategic importance of critical design elements.

This work not only aims to contribute to the development of sustainable and cost-effective airborne launcher systems but also presents a flexible procedural framework applicable to various mission profiles and objectives. The proposed strategy is designed to accommodate evolving requirements, providing a foundation for addressing future challenges and integrating new technological advancements. By outlining both an optimized solution and a robust design methodology, this report aspires to advance the state of the art in airborne launch systems and inspire further innovation in the field.

2 State of the Art

2.1 Air Launch To Orbit

Air Launch to Orbit is an alternative approach for deploying payloads in Low-Earth Orbit (LEO). Unlike conventional ground-launched heavy-lift vehicle, this different method consists in launching a small rocket from a conventional aircraft at altitudes typically above 10 km^[5]. The most notable airborne launchers are better explored in the next paragraph.

The first project of an airborne launcher dates back to the dawn of space exploration. In 1958, a US project called "NOTSNIK" made several attempts to air-launch a small satellite into orbit, using a 5-stage, all-solid rocket booster air-launched from the wing of a Douglas F4D-1 Skyray^[6]. None of them succeeded, therefore the program was abandoned. Pegasus, developed by Orbital Science Corporation (now Orbital ATK), is the only airborne launcher with a wide flight heritage. Since 1990 it has placed over 78 satellites in orbit with over 40 launches^[7]. Pegasus is a winged three-stage solid rocket booster, with an optional fourth stage liquid to perform more precise orbit insertions, capable of delivering up to 450 kg in LEO^[8]. With a length and diameter of 16.9 meters and 1.27 meters respectively, it weights approximately 23 tons. The rocket is dropped from a specially modified Lockheed L-1011 transport aircraft, named "Stargazer", at an altitude of 12 km^[6]. There have been other different projects, however all have been commercial failures. Particularly promising was the LauncherOne from Virgin Orbit, that performed its maiden flight on May 2020 but resulted in a failure after few seconds from its deployment. It was a two-stage vehicle powered by RP-1 and LOX, with a payload capability of 300 Kg into LEO^[9]. Nevertheless, the program has been abandoned^[10].

Airborne Launchers offer several advantages, including an increased flexibility since there is no more the constraint of the launch pad. This allows to have a wide range of different strategies for reaching orbit, enabling the selection of the optimal launch location based on the target orbit's inclination^[11]. Also enables to fly over or around launch constraining weather^[12]. Another key advantage of airborne launchers is their cost reduction. For instance, as analysed in Ref.^[7], considering as reference Delta IV mission, to reach an altitude of 12.5 km the rocket burns 37.6% of first stage propellant. Moreover, speaking in terms of ΔV , the rocket's efficiency is limited to 56% due to gravity and drag losses. Skipping the initial flight phase, the launcher vehicle dimensions and overall lift-off mass can be reduced. In the paper another benefit is also highlighted: typically first stage engines need to be optimized at sea-level or a few km above, while their operative range is very wide. This necessity leads to a performance decrement as the rocket ascends. Launching from an higher altitude allows the nozzle to be optimized for a reduced atmospheric pressure enhancing nozzle efficiency. The main constraint for this particular solution is the carrier aircraft, which limits both the dimensions and maximum rocket's mass. That's the reason why current State of the Art focus only on Small Launch Vehicles (SLVs) capable of delivering payloads below 400 kg. In conclusion, airborne launch systems represent a transformative approach to deploying payloads into Low-Earth Orbit, offering unmatched flexibility and cost-efficiency. However, their development remains constrained by the payload capacity limitations imposed by carrier aircraft.

2.2 Recovery

In the last decade a growing interest in recoverable and reusable launchers has taken over the space sector. The techniques for recovering safely a launcher stage are various and usually the recovery of a specific launcher is composed by multiple techniques, tailored to fit exactly the mission profile. Following mission requirements, the recovery segment of the mission has been designed to minimize costs and damages to the structure, while maximizing the Return On Investment (ROI) of each launch. To perform this it has been chosen to proceed with the use of a HIAD device, which shall decelerate the spacecraft enough to allow for a parafoil opening followed by a Mid-Air Retrieval. The HIAD concept has begun to gain traction in the space sector from the start of the new millennium, with the studies form NASA to test this system for future potential use in the Mars environment. Furthermore this concept has been further studied by

the private sector, with companies such as United Launch Alliance (ULA) attempting to implement it in launchers for the recovery of the key components, such as the Vulacinc engines of the Atlas V.

Inflatable Re-entry Vehicle Experiment 3 (IRVE-3) [13] [14] [15]

The first mission to accurately size and test a HIAD in the Earth's atmospheric environment was NASA's IRVE-3. The main objective of the mission was to validate and test the theoretical data obtained from the previous 2 IRVE experiments. IRVE-3 was the first to implement a toroid model for the aeroshell, which would be inflated by a high pressure release of Nitrogen. The shell itself has a 3 meter diameter, a 60° half-cone angle and is composed of 7 toroids covered by a layer of Flexible Thermal Protection Structure (F-TPS). The F-TPS is composed of various layers of Nextel Fabric, followed by Pyrogel felt insulation and a single kevlar film. This prevents the fabric of inflatable components from ripping and shields the component to be recovered from excessive heat while re-entering.

The whole vehicle had a total reentry mass of around 280 kg and had its own Attitude Determination and Control Subsystem (ADCS) composed of cold gas thrusters using Argon and a Centre of Gravity (CoG) offset mechanism to change the aeroshell's lift and drag. The system contained also it's own power and communication system. The flight of the IRVE-3 was successful and the recovered data helped to validate the second generation of F-TPS as well as the use for inflatable decelerators in Earth's atmosphere.

High-Energy Atmospheric Re-entry Test (HEART) [16] [17]

The High-Energy Atmospheric Re-entry Test (HEART) mission was used to further demonstrate the HIAD functionalities and limits by implementing the recovery system on a Cygnus automated cargo spacecraft. The objective of the mission was to safely recover the spacecraft after a resupply mission to the International Space Station. The inflatable aeroshell had a diameter of 8.3 meters and was composed of 12 toroids. The F-TPS had a composition similar to the IRVE-3's F-TPS, with the only difference being in the number and exact composition of the layers in Pyrogel. The whole system weighed around 1300 kg and was included, similarly to the IRVE-3, its own avionics and power subsystems. The system also included around 500 kg of structures, such as the adapter with the spacecraft and the separation devices as well as all the required interface rings. The vehicle's trajectory was designed to be carefully controlled for maximizing heating and pressure in specific points.

HIAD United Launch Alliance (HULA) [18] [19] [20]

The HIAD United Launch Alliance (HULA) mission was designed to validate the recovery of the centaur stage of the Atlas V launcher. The objective was to validate the efficiency of the HIAD system which would then be implemented in the recovery of the Vulcain engine of the Atlas V. The inflatable aeroshell had a diameter of 6 meters and was composed of 9 different toroids. The system is completely integrated in the payload adapter of the Centaur and the inflation uses a blow-down system with a pressurized tank to release gas in the aeroshell.

The system was designed to have its own avionics and communications system as well as the necessary drogue and parafoil to perform the MAR. This is due to the fact that the mission also wanted to validate their whole Sensible Modular Autonomous Return Technology (SMART) approach, which consists in the use of a HIAD, followed by a parafoil deployment and a MAR performed by an helicopter.

2.3 Multidisciplinary Design Optimization

Multidisciplinary Design Optimization (MDO) is a field of engineering that aims to numerical optimize the design of systems involving different modules, often referred to as *disciplines* [21].

To this end, MDO techniques are used in a great amount of fields such automotive, structure or aerospace engineering in order to handle complex problems that, with ordinary design approaches, would be difficult to solve.

One of the main assets of MDO is the ability to manage simultaneously different variables and disciplines, allowing the algorithm to reach a global optimum of the design, which could not be found handling them sequentially [22]. As a matter of fact, in multidisciplinary problems, decisions aimed at refining the

performance of one discipline often conflict with the requirements or objectives of another discipline. In these scenarios, MDO techniques seek to balance the conflicting objectives of different disciplines in order to attain a globally optimal design.

The Launch Vehicle Design (LVD) is highly relevant in this context, given its complexity and the critical importance of optimizing performance relative to cost^[23]. Indeed, the design of new launchers, since the preliminary phases, involves a complete set of disciplines having strong couplings between them and, moreover every decision influences the quality-to-price ratio of the launch service that will potentially be provided to the customer with the resulting vehicle^[24]. LVD is a particular type of MDO since, additionally to the system-level feasibility, it involves a trajectory simulation and optimization. This latter is subjected to strict equality constraints, complex to match, which sensibly restrict the feasibility region of the problem but, since its optimization is responsible for the performance estimation, it has to be carefully managed and taken into account as a additionally difficulty in the optimization process^[23].

Over the years, various formulations of the problem and methods have been developed. In the following section, an overview of the main MDO techniques applied in LVD will be provided.

2.3.1 MDO State Of The Art

Since MDO techniques were first introduced in the field of engineering, numerous methods have been proposed in the literature. This section focuses exclusively on methods utilizing Single-Level Optimizers. Methods based on Multi-Level Optimizers, along with relevant references, will be presented separately to guide interested readers to the appropriate sources.

The most used method in literature is the Multi Discipline Feasible (MDF). The architecture of this method is the closer one to a classical optimization problem: the crucial difference is that in MDF the analysis is conducted through a Multidisciplinary Analysis (MDA) which at each iteration ensures the feasibility of the solution^[22]. Once the MDA is performed, the variables are transmitted to the system level optimizer. In general the method requires feedback between subsystem but, in literature^{[24] [25]} it is possible to identify examples in which no coupling is present. For a full explanation of the method it is possible to consult Ref.^[26] and Ref.^[27].

The second method presented is the Individual Discipline Feasible (IDF)^{[26] [28]}. In this method, the optimizer is responsible for coordinating the interaction between subsystems. By introducing additional coupling variables, it ensures the feasibility of the solution upon convergence^[22]. The primary distinction from the MDF approach lies in the fact that, at each iteration, only the individual feasibility of each subsystem is ensured, without guaranteeing the consistency of the coupling variables.

The last method presented for the Single Level Methods is the All At Once (AAO)^{[29] [30]}. In AAO, the optimization problem and the individual subsystem equations are managed concurrently by the optimizer, which now controls the state variables of each subsystem. As a result, only a disciplinary evaluation is performed at the subsystem level, while the analysis is conducted at the system level^[22]. It is important to note that comparing these methods is not straightforward, as their effectiveness depends on the specific problem and the user's needs. However, a qualitative summary can be found in Ref.^[22].

Regarding Multi-Level Methods, the most notable ones are *Collaborative Optimization*^[31], *Modified Collaborative Optimization*^[32], and *Concurrent SubSpace Optimization*^[33]. As mentioned earlier, these methods will not be analyzed in detail; however, the reader can refer to the cited references for the initial formulations of the mentioned above methods.

To conclude the section, it is worth to spend a word about the major Optimization Algorithm employed in the problem solution; they divide principally in two categories: Gradient-Based and Gradient-Free. Gradient-Based algorithms differentiate the objective function and the constraints in order to find their descent direction, refer to^[34] for a complete description. Gradient Free (GF) algorithm present interest in the MDO field as they do not require a sensitivity analysis of the objective, which can result tedious for such huge problems, and they allow to work with non differentiable functions. One of the most utilized GF is the Genetic Algorithm (GA), a metaheuristic algorithm which works optimizing an objective function computed on a population that evolves following similar rules as the laws of Natural Evolution principle^[35].

3 Scenario Definition

Before starting with the technical approach, it is worth discussing about the definition of the mission requirements and the House of Quality based on customer requirements. The selection of the carrier aircraft will also be discussed, and finally some preliminary considerations about what kind of payload is considered, given the customer constraints.

3.1 Mission Requirements and House of Quality

The design and development of an airborne launcher presents a unique set of technical and operational challenges. The following analysis presents the system requirements derived from the mission high level goals and comprehensive House of Quality (HoQ), enabling a structured correlation between mission needs and system-level design features.

3.1.1 Requirements definition

Establishing a comprehensive set of high level requirements for the mission is crucial, as these significantly constrain and influence the design of the launcher. The key high level requirements and their influences on the design are presented in Table 3.1.

| High Level Requirements | Design Influences |
|---|---|
| The launcher shall be a LEO Airborne Launcher | Weight and T/W ratios Propellant choice and propellant total masses Trajectory precision during all flight phases with particular emphasis on the capability to execute a pitch-up maneuver |
| The first stage shall be recoverable | Recovery system masses and requirements Trajectory design Material selection |
| The launcher shall have a tandem configuration | Configuration design Second stage detachment altitude First stage thrust and propellant masses |
| The launcher shall be able to insert a payload mass of 250 kg in an SSO 98° at 400 km with a minimum accuracy of 10 km and ±0.5 deg | Trajectory accuracy Fairing design Propellant masses Orbit insertion maneuvers |
| The launcher shall be capable of bringing a payload mass of 400 kg to orbit | Fairing dimension Fairing mass Required ΔV |
| The aircraft shall lift-off from a civil aircraft and perform the lift-off from a civil airport | Aircraft selection Launcher release altitude Launcher dimensions |

Table 3.1: High level requirements and design influences

The mission presents nice-to-have requirements, which can be rated or scored based on their importance. These are:

- Short time-to-market, maximum 4-5 years
- Small number of reuses to reach the BEP
- Reusability of the second stage
- Low propellant toxicity

Since these requirements are not mandatory, they have been selected to guide the final choices. They

will influence the initial decisions and be reassessed after the process to quantify their value and rank the resulting solutions.

System and Subsystems Requirements The requirements definition process begins with high-level objectives, structured hierarchically in a tree approach, progressing from the most general to the subsystem level. Each requirement is linked to its parent, ensuring clarity and streamlining the review process.

All requirements are consolidated in the Mission Requirements Document, providing a comprehensive reference: [*Mission-Requirements-Document.xlsx*](#)

3.1.2 House of Quality

The House of Quality is a key tool to align customer requirements with technical specifications. It was applied to translate the mission's high-level and nice-to-have requirements into actionable design priorities. By systematically evaluating their impact on the final solution, this approach aimed to prioritize the design choices which address the mission objectives, while optimizing the performances.

To align design choices with market needs, a competitive analysis was conducted. Different categories of competitors were identified to facilitate a comprehensive comparison between the mission's high-level requirements and the current offerings in the launch market. *Pegasus*, *Northrop Grumman* and *LauncherOne*, *Virgin Orbit* were selected as benchmarks for airborne launches. Additionally, *Falcon 9*, *SpaceX* was included to evaluate reusability constraints. Lastly, *Electron*, *Rocket Lab* was analyzed for its comparable payload mass and incorporation of innovative technologies and materials.

The output of this process translates into a design guideline emphasizing reusability and adaptability to different payload mass capabilities. Particular attention is given to structural masses, which are critical parameters in airborne launchers due to their impact on overall performance and feasibility. The complete HoQ development and results are presented in Appendix A.

3.2 Fairing Design and Payload Accommodation

The nominal payload for the launcher is set by the mission requirements to $M_{payload} = 250 \text{ kg}$. Moreover, the design of the fairing has to be flexible to accommodate a maximum payload of $M_{payload} = 400 \text{ kg}$ in unspecified LEO orbits. To guide the design, this constraint is considered as a volume constraint, which represents a critical parameter in the fairing sizing process.

The first step is to estimate the volume required to host a 400 kg payload. To obtain this value, the average density of satellites has to be computed. From a literature review, the masses and volumes of payloads around 400 kg were tabulated^[36]. The average density was then calculated through a weighted interpolation, prioritizing payloads with masses closer to the target value. After an additionally 20% safety margin the hypothetical payload dimensions are obtained.

The next step is the definition of fairing shape. In literature a widespread range of shapes is used. The team selected a blunted nose cone, as it is a good trade-off between achieving near-optimal aerodynamic efficiency in terms of Drag Coefficient C_d , typical of ogival shapes, and maximizing the payload usable volume^[37]. The suggested Bluntness Ratio (B_r), defined as: $B_r = R_{nose}/R_{fairing}$, to avoid a significant increment in C_d is 0,15.

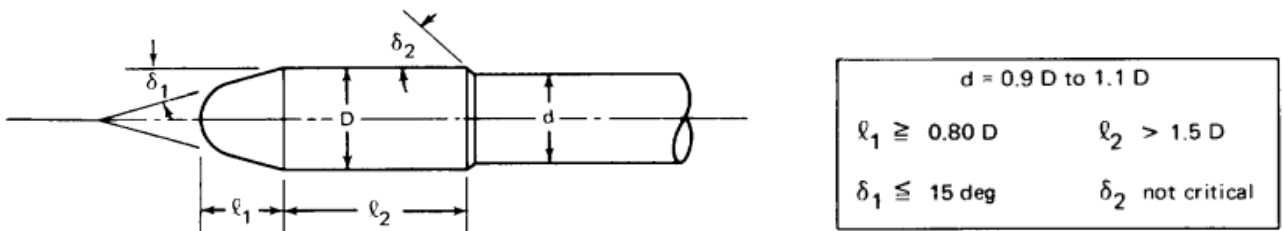


Figure 3.1: Geometric guidelines given by NASA^[1]

Regarding the dimensions, the team followed the geometric indication given by NASA^[1] to obtain a buffet

free shape. Buffeting arises from the separation of the boundary layer and the transition to turbulent flow, which can induce significant aerodynamic loads and vibrations. By following the guidelines presented in Figure 3.1, the fairing was optimized to ensure smoother aerodynamic performance, minimizing flow disturbances and protecting the payload during ascent.

Finally, the payload average volume and the fairing shape are converted into a design constraint on the fairing volume. For instance, each configuration analysed should fill the fairing at least the 50% of the fairing internal volume to ensure an efficient use of space, avoiding an unnecessary increment of mass due to an oversized fairing.

3.3 Carrier Aircraft

The selection of the carrier aircraft is crucial for the overall design of the launcher, as it imposes constraints on the rocket's mass, size and shape. Based on the requirement to avoid any military platform, the team selected as carrier aircraft a modified Boeing 747-400F. The decision has been driven by several factors: the aircraft's well-proven use by Virgin Orbit for Launcher One, its widespread availability across global airline commercial fleets, and its suitability with our mission profile, offering the necessary top speed and payload capacity for a successful deployment, as reported in Table 3.2.

| | |
|-------------------------------------|-----------|
| Maximum Mach Operating | 0.92 |
| Maximum Operational Altitude | 13100 m |
| Maximum Payload | 124330 kg |
| Range with Maximum Payload | 8240 km |

Table 3.2: Boeing 747-400F Specifications^[2]

To reduce aerodynamic disturbances from the aircraft's flow during the launch, the rocket is placed below the wing, where a space is typically allocated for a fifth engine. The modifications that need to be implemented regards mainly the reinforcement in the wing area to allow the wing to sustain the rocket, the separation mechanism for the detachment of the rocket at launch, and a proper weight distribution should be carefully calculated, as the addition of the rocket could affect the aircraft's overall balance and handling.

3.4 Launch Location & Deployment Conditions

First of all, it is crucial to define the Launch Location. To reach the target orbit of our mission, a Sun-Synchronous Orbit (SSO) at 400 km altitude with 98° orbit inclination, the launch needs to be directed towards North-West or South-West, ideally as far away from the equator as possible^[38]. This approach maximizes the launch efficiency, ensuring a lower ΔV loss during orbit insertion.

Another crucial factor in selecting launch location is ensuring safety for people on ground. Both the launcher detachment from the carrier and first stage separation must take place over the ocean. This minimizes the risks associated with falling debris. Furthermore, also the return of the carrier at the take-off airport needs to be taken into consideration. The aircraft's maximum range, considering also the additional payload of the rocket, is crucial to assess the feasibility of the launch location.

Taking into account all the aspects listed above, the team selected as take-off airport Bergen Airport, Flesland, Norway (IATA Airport Code: BGO). With a latitude of 60°17'37" N, and the possibility to launch across Norwegian Sea, it fulfils all the necessary criteria for an optimal launch location, making it an ideal launch site for the mission.

Once the Launch Location has been selected, deployment conditions have been defined based on aircraft performance limits considering velocity, altitude and pitch angle at launch. Looking from existing launch vehicles, a deployment condition at 12000 km altitude and 0.82 Mach with a 28° pitch angle has been selected. According to Boeing 747-400F specifications^[2], this condition is feasible. In addition, achieving a significant pitch angle ensures a reduction in ΔV losses during primary launch phases, as demonstrated by Sarigul-Klijn in Ref.^[12], even if it causes additional modifications to the carrier.

4 Technical Approach

This chapter outlines the technical approach employed for the design of an airborne launcher given the requirements and mission constraints stated in Chapter 3. Starting from an extensive literature review to create a solid baseline, the implementation of the MDO framework to choose the optimal configuration in terms of GLOM will be described. Furthermore, a detailed design for each subsystem is presented, comprising the recovery strategy adopted.

4.1 Baseline Approach

The baseline technique was used to begin the launcher's conceptual design. The development process can be shortened by using a baseline, which is typically another rocket design with high-fidelity data. Various flight-proven technologies have been examined, including previously developed airborne launched projects. The analysis starts with the propellants choice. The two options considered were Liquid Rocket Engine and Solid Rocket Motors, since they are the most reliable technologies for rockets propulsion. Liquid Rocket Engines ensure higher performance in terms of Thrust and Specific Impulse, as well as enhanced orbital accuracy for the upper stages. The drawback of this architecture is the high design complexity. However, given as reference the request in [3.1] and the recovery requirement on the first stage, the team decided to select a liquid propulsion architecture for each stage, prioritizing their performance advantages. Furthermore, this latter choice is reinforced by the fact that second stage recoverability is analysed. At this stage, the team's knowledge is once again primarily driven by the system requirements and the HoQ. Consequently, a more detailed propellants analysis is crucial.

The propellant couples analysed are the ones presented in^[39] and evaluated by looking at their inherent features through a decision matrix. Following the same approach, another decision matrix was constructed to evaluate the choice on the external structure and the tank material. The decision matrices can be consulted in Appendix B.2.

The outcomes of this process are: RP-1-LOX, CH4-LOX and LH2-LOX as propellant couples, 7075 Al alloy and the HS Carbon fiber composite as materials.

4.1.1 Configurations choice

As anticipated before, a careful selection of the most promising configurations to be analysed is mandatory. Taking into account the target orbit altitude, the gravity losses, the launch site losses and the aircraft velocity (defined in Section 3.4) at deployment condition, ΔV_{tot} required to reach the target orbit is estimated through an energetic approach:

$$\Delta V = \Delta V_{orbit} + \Delta V_{gravity} + \Delta V_{launchsite} - \Delta V_{aircraft} \quad (4.1)$$

This energetic approach is to be considered quite inaccurate because of assumptions made, like the gravity losses computed considering a vertical launch.

After calculating the ΔV budget, the minimum number of tandem stages required to accomplish the mission has been determined through an optimal staging analysis. By assuming average specific impulses, typical structural mass indexes, and standard values for the thrust-to-weight (T/W) ratio, the analysis led to the selection of a two-stage tandem configuration.

Among chemical propellants, LOX/LH2 achieves one of the highest specific impulses. However, its low density, complex cryogenic handling, and lower thrust-to-weight ratio make it poorly suited for first stages, which require high thrust, simplicity, and efficient use of space to improve aircraft integration and reduce atmospheric drag.

The chosen carbon composite consists of IM7 fibers and HexPly 8552, a high-performance epoxy matrix designed for aerospace structures. It offers excellent mechanical properties and reliability at high temperatures^[40]. Proceeding with the analysis, a large number of launchers is taken into account to establish a baseline. Both airborne-launched rockets and traditional ones are analysed to obtain a wide, solid and high-fidelity database, used as starting point for launcher's development due to the scarcity of airborne launchers state-of-the-art.

The baseline analysis is conducted comprehensively by consulting different launcher's manuals [9] [41] [42] [43] [44] [45] [46] [47] [48] [49] [50]. This approach ensures flexibility in the design process, enabling a Multidisciplinary Design Optimization (MDO) to evaluate various options. Based on these criteria, the selected configurations are presented in Table 4.1.

| Conf ID | 1 st stg. couple | 1 st stg. material | 2 nd stg. couple | 2 nd stg. material |
|---------|-----------------------------|-------------------------------|-----------------------------|-------------------------------|
| 1 | LOX/RP-1 | Carbon composite | LOX/RP-1 | Carbon composite |
| 2 | LOX/RP-1 | Carbon composite | LOX/LH2 | Carbon composite |
| 3 | LOX/RP-1 | Carbon composite | LOX/LCH4 | Carbon composite |
| 4 | LOX/LCH4 | Carbon composite | LOX/RP-1 | Carbon composite |
| 5 | LOX/LCH4 | Carbon composite | LOX/LH2 | Carbon composite |
| 6 | LOX/LCH4 | Carbon composite | LOX/LCH4 | Carbon composite |
| 7 | LOX/RP-1 | 7075 Al alloy | LOX/RP-1 | Carbon composite |
| 8 | LOX/RP-1 | 7075 Al alloy | LOX/LH2 | Carbon composite |
| 9 | LOX/RP-1 | 7075 Al alloy | LOX/LCH4 | Carbon composite |
| 10 | LOX/LCH4 | 7075 Al alloy | LOX/RP-1 | Carbon composite |
| 11 | LOX/LCH4 | 7075 Al alloy | LOX/LH2 | Carbon composite |
| 12 | LOX/LCH4 | 7075 Al alloy | LOX/LCH4 | Carbon composite |

Table 4.1: Configurations

Although winged configurations were initially considered in the baseline analysis, they were excluded during the design process due to inferior performance compared to non-winged designs.

4.2 MDO Approach

An MDO framework has been implemented to evaluate all the different configurations presented in Table 4.1 using a Genetic Algorithm in order to find the optimum for the LVD problem.

The rationale for these choices is based on the MDO framework's capability to conduct high-level optimization across multiple disciplines, which is particularly suited for the conceptual design phase where detailed subsystem-level iteration is less critical. Furthermore, the GA is identified as the appropriate optimization method as stochastic algorithms eliminate the need for an initial solution, unlike gradient-based methods^[24]. The primary goal of this approach is to identify configurations that maximize performance metrics while meeting design and mission constraints. A more comprehensive overview of the process adopted to find the optimal overall configuration is showcased in Section 4.9.

For this study, the selected MDO architecture is a Multi Discipline Feasible, which, as outlined in Section 2.3, simplifies optimization by focusing solely on design variables and facilitating convergence.

4.2.1 LVD problem formulation

The launch vehicle design problem is formulated as follows^[22]:

$$\text{Minimize: } J(\mathbf{z}) \quad (4.2)$$

$$\text{With respect to: } \mathbf{z} = \{\mathbf{z}_{d_k}, \mathbf{z}_{c_j}\}, \quad k = 1, \dots, n_{stages}, \quad j = 1, \dots, n_{points} \quad (4.3)$$

$$\text{Subject to: } \mathbf{g}_k(\mathbf{z}_{d_k}, \mathbf{z}_{c_j}, \mathbf{x}) \leq 0, \quad (4.4)$$

$$\mathbf{h}_k(\mathbf{x}_f) = 0, \quad (4.5)$$

$$\dot{\mathbf{x}} = \mathbf{s}(\mathbf{z}_{d_k}, \mathbf{z}_{c_k}, \mathbf{x}). \quad (4.6)$$

Where:

- J : objective function.
- \mathbf{z}_d : design variables.
- \mathbf{z}_c : control variables.
- \mathbf{g} : inequality constraints.
- \mathbf{h} : equality constraints.
- \mathbf{x} : state vector (position and velocity of the launch vehicle).
- \mathbf{s} : dynamics of the state vector.
- n_{stages} : number of stages of the launch vehicle.
- n_{points} : number of discretization points of the trajectory.

For each of the twelve configurations, a set of input parameters was defined. Certain parameters, such as the launch height from the carrier, remain constant across all configurations. Others, such as the combustion chamber or tank pressure, are adjusted to suit each configuration (refer to Appendix C.4). The optimization variables selected for the genetic algorithm and the trajectory analysis are as follows:

$$\text{Design Variables: } \mathbf{z}_{d_k} = \{OF, TW, M_p, P_e, D\}_k, \quad k = 1, \dots, n_{stages}, \quad (4.7)$$

$$\text{Control Variables: } \mathbf{z}_{c_j} = \{\theta\}_j, \quad j = 1, \dots, n_{points}. \quad (4.8)$$

Where:

- OF : Oxidizer to fuel ratio.
- M_p : Propellant mass.
- TW : Thrust over weight ratio.
- D : Stage outer diameter.
- P_e : Nozzle exit pressure. For the first stage the optimization variable is the nozzle optimal altitude, z_{opt} , while for the upper stages the optimization variable is the nozzle expansion ratio ε .
- θ : Pitch angle at each discretized point of the first stage trajectory.

The bounds of each design variable are determined by applying shifts from a nominal value based on other space launchers, considering data availability and reliability in the literature: $\pm 20\%$ for M_p , D , and TW ; $\pm 15\%$ for the OF ratio; ± 2 km for the nozzle optimal altitude; and $\pm 35\%$ for the expansion ratio.

Starting from a literature research addressing MDO for Launch Veichle Design^[21], it has been decided to reduce the number of variables to ease the convergence of the genetic algorithm.

The objective function J to be minimized is computed as the product between the Gross Lift-Off Mass (GLOM) and the different penalty components linked to the inequality constraints to be satisfied^[51]. The equality constraints are related to the trajectory optimization which is computed for each individual of the genetic algorithm and are therefore not included in the formulation of the objective, as seen in Section 4.6. The objective function is defined as follows:

$$J(\mathbf{z}) = GLOM \cdot I_c, \quad \text{with } I_c = \prod_{i=1}^{N_c} I_{c_i}, \quad \text{and } I_{c_i} = \begin{cases} 1 & \text{if } p \leq 1, \\ p \cdot 10 & \text{if } p > 1 \end{cases}. \quad (4.9)$$

Where p is the percentage of constraint violation:

$$p = \left| \frac{x_{\min} - x}{x} \right| + 1 \quad (\text{for } x \geq x_{\min}), \quad p = \frac{x - x_{\max}}{x_{\max}} + 1 \quad (\text{for } x \leq x_{\max}). \quad (4.10)$$

Where I_{c_i} is the performance index attributed to the i-th constraint.

The inequality constraints are defined in Table 4.2:

| | x_{\min} | x | x_{\max} |
|------------------------------|------------|---|------------|
| First stage ε_s | 0.06 | ε_{s_1} | 0.16 |
| Second stage ε_s | 0.10 | ε_{s_2} | 0.19 |
| Fairing filling fraction | 0.55 | V_{fil} | 0.90 |
| max q | - | q | 50 kPa |
| Nozzle diameter | - | D_{noz_i} | D_i |
| Diameters ratio | - | D_1/D_2 | 1.20 |
| M_p for re-entry burn | 1 | $M_{p_{\text{left}}} / M_{p_{\text{RE}}}$ | 1.35 |

Table 4.2: Inequality constraints

The objective function is constructed in such a way that when the GLOM is minimized and the performance index of the inequality constraints goes to one, an optimal solution is found.

4.2.2 Block Scheme Definition

A schematic representation of the block scheme used in the development of the MDO is shown in Figure 4.1. For a more complete description of the block scheme, refer to Appendix C.4.

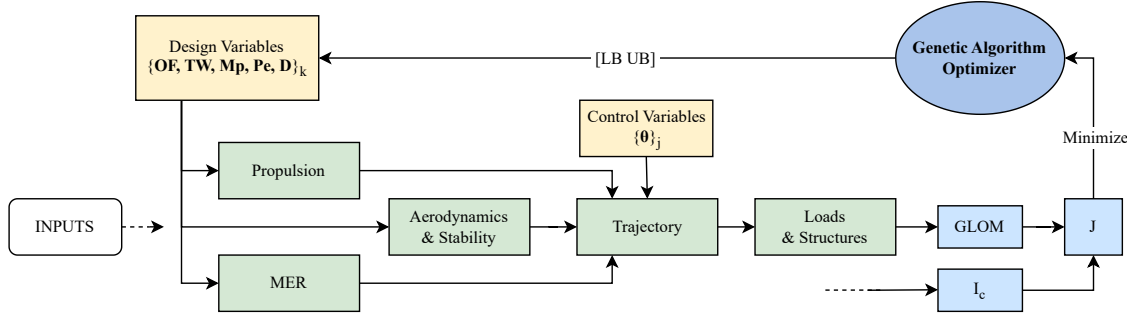


Figure 4.1: Block scheme of the system

In the following sections, a more detailed description of the technical approach for the design of the subsystem blocks in the context of the MDO will be presented.

4.3 Propulsion System

The first step in propulsion system design is architecture selection. Based on mission requirements, and the necessary performance, a pump-fed architecture was selected for both stages. This choice is driven by the large volume of propellant required and the possibility to keep tanks at a lower pressure (around 3 bar). The proper cycle need to be chosen, as it affects the combustion chamber pressure P_c . The gas generator cycle is selected, due to its relative simplicity with respect to the other options and lower inert masses, even if it is slightly less efficient, as P_c is generally lower^[52].

Propulsion Design The variables of the optimization process are the O/F and T/W ratio for both stages, and the P_e . Pressure in the combustion chamber P_c has been selected for each configuration and for each stage from baseline data, looking at flight-proven engines with similar performance and aligned with the requirements of our propulsion system. Only the design process for the 1st stage engine is presented, as the methodology for 2nd stage follows a similar approach.

Using then NASA CEA code, giving as input P_c and O/F for the selected propellant couple, all the thermochemical parameters have been retrieved. From them, and knowing P_e , the following parameters are computed: c^* , nozzle exit velocity v_e , 1st stage expansion ratio ε .

Knowing the T/W ratio, and retrieving from the previous iteration the GLOM, thrust T_{opt} in optimal expansion condition can be computed. Subsequently, the mass flow rate \dot{m} is determined using the thrust equation under optimal expansion conditions. From that, the throat area A_t and nozzle exit area A_e can be retrieved via Equation (4.11):

$$\dot{m} = \frac{T}{v_e} \quad A_t = \frac{c^* \dot{m}}{P_c} \quad A_e = \varepsilon A_t \quad (4.11)$$

For simplicity \dot{m} is assumed to remain constant.

Then the geometry of the engine is derived. For simplicity, in the optimization loop a conical nozzle has been considered, with an $\alpha_{div} = 15^\circ$. Then once the final configuration is chosen, a bell nozzle is implemented with $L_{Bell} = 0.8L_{Conical}$, as it is a good compromise between compactness and efficiency. Considering a characteristic length L^* from Sutton^[52] for each propellant pair, the overall engine length is retrieved. In order to compute the real Thrust and Specific Impulse provided by the engine, 2D-losses λ is calculated once the geometry of the engine is defined.

In conclusion, the primary parameters, Thrust and Specific Impulse, have been calculated via Equation (4.12) as a function of altitude, as seen in Appendix D, taking into account the changes in ambient pressure with increasing height:

$$T = \lambda \dot{m} v_e + (P_e - P_{amb}) A_e \quad Isp = \frac{T}{\dot{m} g_0} \quad (4.12)$$

Regarding 2nd stage design, the flow-chart is the same, with the only difference being that expansion ratio ε needs to be imposed, as the engine will operate in vacuum. Therefore, the 2nd stage engine will never reach optimal expansion conditions, as baseline data indicates that the detachment of the first stage typically occurs at altitudes higher than 80 km. The equations used are the same as above, with the only difference being in Equation (4.12), where P_{amb} is zero.

To validate the propulsion engines described above, the results have been compared in Appendix K.1 with Merlin 1C real data.

4.4 Estimation of Masses and Dimensions

The process of estimating the inert masses and the dimensions of the launcher is a key phase of the development of the design; its objective is to divide the launcher into components, providing an estimate of each mass, and allocating the space for each of them. The procedure followed is the one proposed by Edberg and Costa^[53] involving Mass Estimation Relation (MER), but due to the peculiarity of a recoverable airborne launcher, some correction factors have been applied to adapt the design.

The goals of this part of the development are: to provide an estimate of the total mass (GLOM) to simulate the trajectory, and to use the lengths of the components and their centres of mass to perform the structural sizing. The process is iterative, starting a new iteration with the “real” masses from the previous iteration’s structural sizing until they match with a fixed tolerance. Correction factors for the tanks have been applied based on the mismatch between the masses estimated with the MERs and the ones computed after the structural sizing described in Section 4.7.

Tanks In order to provide a preliminary design, the sizing process of the tanks is led by different considerations. First of all, the volume of each tank has been sized considering a cylindrical shape with elliptical domes (with aspect ratio $AR = 2$). Then some additions are made to take into account both the ullage (3%) and the shrinkage caused by the expansion of the cryogenic propellants:

$$V_{tank} = V_{prop} (1 + \text{ullage} + \text{shrink}) = V_{prop} (1 + \text{ullage} + 3\alpha_{exp}\Delta T) \quad (4.13)$$

Where the specific linear expansion coefficient (α_{exp}) and ΔT are considered for each case.

The possibility of tanks with a common bulkhead has been analysed with the intent of reducing the inert mass. The chosen configuration presents tanks with a common bulkhead for both stages, where the lower dome of the LCH₄ tank extends into the LOX tank. This configuration has shown to be the most promising in reducing inert masses.

Starting from the volumes, the dimensions of the tanks (the height of the cylindrical part h_{cyl} , the height of the domes h_{dome} , the surface A_{tank}) are computed. The heights of the tanks and the diameters are used to size the dimensions of the launcher, while the area A_{tank} is used to compute the insulation mass required by the cryogenic propellant (refer to Appendix E.2).

For what concerns the mass of the tanks, some correction factors have been applied to the MERs. By iterating the design loop it has been noticed that the MERs tend to underestimate the masses computed after the structural analysis, leading to large errors in the dry mass. This can be explained by considering that the volumes of our tanks are small, while the MERs found^[53] are in a considerably wider range of volumes, leading to a possible dispersion of the results for small volumes.

| Component | Original MER ^[53] | Corrected MER (AL) | Corrected MER (CF) |
|------------------|------------------------------|----------------------------|------------------------------|
| $m_{tank,LOX}$ | $0.0107 m_{LOX}$ | $2 \times 0.0107 m_{LOX}$ | $1.8 \times 0.0107 m_{LOX}$ |
| m_{tank,LCH_4} | $12.16 V_{LCH_4}$ | $2 \times 12.16 V_{LCH_4}$ | $1.8 \times 12.16 V_{LCH_4}$ |

Table 4.3: MERs for tanks

Other inert masses The other inert masses considered are the interstages (considered as thin-walled cone frustums), the aft skirts (thin-walled cylinders), the engine blocks (thrust structure, liquid pump-fed engine, TVC gimbals), the avionics, the wirings, the fairing (with its external structure and the payload adapter), and the recovery structure. Appendix E.2 presents a complete development of these components.

Centres of mass Having assigned the masses and the dimensions of each component, the Centre of Mass (CoM) can be computed. The position of the centre of mass x_{CM} is given by Equation (4.14):

$$x_{CM} = \frac{\sum_i m_i x_i}{\sum_i m_i} \quad (4.14)$$

Where the position $x = 0$ is the nose tip. To estimate this value some assumptions have been made. Avionics is divided into the upper and lower stages by 80% and 20%^[53] respectively, the engine block is considered a point mass and the wiring concentrated in the middle of the stage. The propellant's CoM shifts based on the burned fraction. The CoM of each component is allocated individually, and the CoM of the launcher is computed. The launcher is divided into five characteristic regions (i.e., fairing, 1st and 2nd stage, 1st and 2nd interstage) and by considering the items inside each region, the respective CoM positions of these 5 parts are computed.

4.5 Aerodynamics and Stability

This module enables the computation of lift and drag forces across the full range of flight conditions, accounting for variations in velocity, altitude, and angle of attack. The calculation of these forces is determined by the rocket's design parameters, including stage diameters, total length, and the size and geometry of the nose cone. A stability block, strongly linked with the aerodynamics, has been taken into account.

For what concerns the aerodynamics, wings and tail with all their related parameters are included in the block implementation to complete the treatment. Moreover, the computation considers the specified flight conditions and engine mode, which influences in particular the base drag.

4.5.1 Aerodynamics

Body alone geometry aerodynamics The aerodynamic model is based on the component build-up methodology. The objective is to evaluate the aerodynamic coefficients for a body-wing-tail rocket. The first step involves calculating the aerodynamic coefficients C_A and C_N for the rocket body.

To compute C_N , the Jorgensen method is applied^[54] (detailed C_N computation: Appendix F.1). To estimate the axial coefficient C_A instead, Fleeman's relations are used^[55]. This choice is based on the greater accuracy of Fleeman's formulas compared to Jorgensen's in predicting the axial coefficient for a zero angle of attack. While Jorgensen's method captures the general trend of C_A for $0^\circ < \alpha < 180^\circ$, it introduces significant errors for $\alpha < 45^\circ$, which is the primary range of expected angles of attack in the trajectory. Therefore, C_A is computed as follows (a detailed C_A computation can be found in Appendix F.2):

- Axial coefficient at $\alpha = 0$: $C_{A0} = C_{Aw} + C_{Af} + C_{Ab}$
- Axial coefficient: $C_A = C_{A0} + m \cdot \alpha$, where the coefficient m is obtained from comparison with experimental data and depends on the nose shape.

Since the coefficients are evaluated in the axial and normal reference, a change of reference to the tangential and normal direction of the velocity is required to get the C_L and C_D . The estimation algorithm is validated against NASA experimental data^[56] for Mach numbers 1.501.50 to 2.862.86 and angles of attack 1.50 to 2.86, resulting in correction coefficients to address transonic overshoot in C_{Aw} .

Body-wing-tail aerodynamics To evaluate the body-wing-tail configuration NKP method was used, accounting for the aerodynamic interference of the surfaces.

The lift coefficient is obtained as (detailed NKP method: F.4):

$$C_{LNKP} = C_{LN} + C_{LWB} + C_{LBW} + C_{LTB} + C_{LBT} \quad (4.15)$$

The lift contribution due to wing vortices is neglected for preliminary analysis. Furthermore $C_{L\alpha}$ is obtained from the linearized thin airfoil theory (2D), using the Prandtl-Glauert transformation^[57]. The results obtained are compared with the experimental results of Pegasus Air-Launched Booster^[58] ($M =$

1.60, 4.63; $0^\circ \leq \alpha \leq 24^\circ$), as this is taken as a baseline for cases involving the use of wings. From the experimental Pegasus data a linear correction coefficient for C_L is obtained as a function of Mach. Furthermore also the $\frac{C_L}{C_D} = \frac{C_L}{C_D}(C_L, M)$ is obtained from experimental data:

$$C_L = C_{L,NKP}(k_{1C_L} \cdot M + k_{0C_L}) \quad C_D = k_{2C_D} C_L^2 + k_{1C_D} C_L + k_{0C_D} \quad (4.16)$$

k coefficients are obtained from linear interpolation as a function of Mach, based from experimental data of Pegasus.

The validation of the body-wing-tail model is conducted on the experimental data of Pegasus Air-Launched Booster [58].

Body-tail aerodynamics In case of just body-tail configuration, the coefficients are obtained evaluating independently the body and tail aerodynamic coefficients from the previous formulas (for body alone geometry and tail). The overall coefficients are then obtained linearizing the phenomena:

$$C_{Lbody-tail} \approx C_{Lbody} + C_{Ltail} \quad C_{Dbody-tail} \approx C_{Dbody} + C_{Dtail} \quad (4.17)$$

4.5.2 Stability

To continue the analysis performed in the Aerodynamics section it is necessary to evaluate the launcher stability, which is a critical design phase of any space vehicle. Here the evaluation is intended to be a simpler version of the more accurate analysis usually required. Indeed the rocket's stability is evaluated only from the dropping instant and during the next five seconds before the engine ignition, as after ignition the thrust vector control can be used to help stabilize the rocket. A more accurate control loop should be performed in the next phases of the design process.

To ensure the static stability in the first flight instants, the position of the centre of pressure of the rocket is computed through an empirical correlation found in literature [55]:

$$\frac{x_{CP}}{h_{Nose}} = 0.63 (1 - \sin^2(\alpha)) + 0.5 \frac{L_B}{h_{Nose}} \sin^2(\alpha) \quad (4.18)$$

This formula relies on some assumptions: the body is assumed to be composed by a Nose and a Cylinder, slender body theory and C_p is considered as a property of the nose only.

After computing the static margin as $l_{sm} = \frac{x_{CP}-x_{CG}}{d}$ and noticing that it has a negative value, a decision has to be made on the way to guarantee the static stability. The design decision made is to incorporate fins positioned aft of the Centre of Gravity (CoG) to shift the center of pressure (CP) backward, ensuring it remains behind the rocket's CoM. This configuration provides aerodynamic stability while maintaining control authority throughout the flight. To achieve static stability, a minimum of three tail surfaces is required. Accordingly, a three-fin trapezoidal configuration in a Tri-Tail arrangement was chosen, inspired by the proven design employed by the Northrop Grumman Pegasus airborne launcher. [8] Among the three fins only two are considered to generate lift with an inclination angle of 30° . To compute the fins surface, a missile baseline is adopted from 'Tactical Missile Design' from Eugene L. Fleeman [55]. The aspect ratio of the fins is chosen as 2.82. Then the mean chord of the fin is supposed from the same baseline. First the position of the center of pressure in the fin is computed and then, evaluating the critical Mach number from the AR, the fin surface is computed to counter balance the moment generated by the lift applied in the center of pressure of the total body:

$$\begin{cases} S_{fins} = \frac{L|x_{CP}-x_{CG}|}{\pi \frac{AR}{2} |\sin(\alpha_W) \cos(\alpha_W)| + 2 \sin^2(\alpha_W) q(x_{CP_wings}-x_{CG}) \cos(i)} & \text{if } M_{actual} < M_{critical} \\ S_{fins} = \frac{L|x_{CP}-x_{CG}|}{4 \frac{|\sin(\alpha_W) \cos(\alpha_W)|}{\sqrt{M_a^2 - 1}} + 2 \sin^2(\alpha_W) q(x_{CP_wings}-x_{CG}) \cos(i)} & \text{if } M_{actual} \geq M_{critical} \end{cases} \quad (4.19)$$

where α_W is the angle of incidence of the wing assumed as equal to 10° and i is the inclination angle with respect to the launcher pitch axis which for a Tri-Tail symmetric configuration is equal to 30° . The two equations relies both on the Newtonian impact theory and moreover in two different theories: linear wing theory and slender wing theory respectively [55] [59]. Furthermore, knowing the AR and the fins surface, the computation of the semi-span of the fins conclude the sizing process. Finally, the fins mass is computed with a typical area density for general aviation found in literature. [53] Some of the correlations used to compute other important design parameters for the fins are presented in Appendix Figure G.

4.6 Trajectory

The first stage follows an open loop optimized trajectory, defined by a series of points that describe the rocket's pitch as a function of time. At any given time, the required pitch is linearly interpolated between these points. The second stage follows a closed loop Powered Explicit Guidance algorithm. This guarantees a good orbit insertion accuracy and efficient propellant use, even when the first stage deviates from its nominal flight path.

The chosen trajectory configuration of open loop first stage and closed loop second stage is typical of most space launchers, as it offers a good trade-off between minimizing ΔV and not requiring excessive on board computing power. In Equation (4.20) the two sets of 3DOF equations of motion used are reported.

$$\begin{cases} \frac{d\bar{r}}{dt} = \bar{v} \\ \frac{d\bar{v}}{dt} = \frac{\bar{T} + \bar{D} + \bar{L}}{m} - \frac{\mu}{|\bar{r}|^3} \bar{r} \\ \frac{dm}{dt} = -\dot{m} \end{cases} \quad \begin{cases} \frac{dr}{dt} = \dot{r} \\ \frac{d\dot{r}}{dt} = \frac{T \cdot \sin(\theta(t)) - D \cdot \sin(\gamma) + L \cdot \cos(\gamma)}{m} - \frac{\mu}{r^2} + \frac{v_\theta^2}{r} \\ \frac{dv_\theta}{dt} = \frac{T \cdot \cos(\theta(t)) - D \cdot \cos(\gamma) - L \cdot \sin(\gamma)}{m} - \frac{2\dot{r}v_\theta}{r} \\ \gamma = \tan^{-1}\left(\frac{v_\theta}{\dot{r}}\right) \\ \frac{dm}{dt} = -\dot{m} \end{cases} \quad (4.20)$$

The first system describes the trajectory of a rocket in cartesian coordinates, where T is the thrust, D the drag and L the lift. The second system describes a 2D trajectory, with a non rotating earth. One simplification that has been done is to assume that the thrust is aligned with the rocket, so the thrust will always be aligned with the pitch. Another simplification is that no attitude control is considered, it is assumed that the rocket follows the trajectory perfectly.

Trajectory Azimuth The required trajectory azimuth can be calculated such that the target inclination is reached at the end of the burn, in order to minimize ΔV losses from a plane change manoeuvre.

Using spherical geometry, the required azimuth can be calculated as: $\beta_{in} = \sin^{-1}\left(\frac{\cos(i)}{\cos(L)}\right)$

With i the target inclination, L the latitude and β_{in} the azimuth. β_{in} is inertial in that it assumes no initial velocity. The real azimuth can be calculated using B_{in} and considering the initial horizontal velocity using simple geometry. All the vectors and angles involved in this calculation can be seen in Figure 17. With v being the current horizontal velocity, v_T the target orbital velocity and v_{rem} the remaining horizontal velocity to reach orbit, then:

$$v_T = v + v_{rem} \quad v_{x,rem} = v_T * \sin^{-1}(\beta_{in}) - v_x \quad v_{y,rem} = v_T * \cos^{-1}(\beta_{in}) - v_y \quad (4.21)$$

And the required azimuth can be calculated as: $\beta = \tan^{-1}\left(\frac{v_{x,rem}}{v_{y,rem}}\right)$

Ideally, the azimuth would remain constant throughout the flight, calculated only at launch. However, due to the changing latitude during flight, maintaining a fixed azimuth would lead to slight deviations in the target inclination. This is crucial for near polar orbit missions, where latitude changes significantly through the flight. To correct this, the azimuth is recalculated continuously during the flight to ensure accurate trajectory alignment.

Additionally the current and final yaw angles can be calculated. First the azimuth of the velocity has to be calculated, and then the current and estimated final yaw angles can be computed, this are useful for estimating the plane change losses in the Power Explicit Guidance (PEG).

$$\beta_{vel} = \tan^{-1}\left(\frac{v_x}{v_y}\right) \quad \psi_0 = \beta_{vel} - \beta \quad \psi_T = \beta_{in} - \beta \quad (4.22)$$

4.6.1 Powered Explicit Guidance

The second stage trajectory follows a Power Explicit Guidance (PEG) algorithm. Its implementation is detailed in Appendix H.1. This trajectory algorithm guarantees a high orbit insertion accuracy (with expected deviations below a couple of kilometres), even when the first stage flies in off nominal conditions or with a non-optimal trajectory.

4.6.2 Trajectory Optimization

A set of constraints is imposed on the first stage trajectory points to ensure that the rocket can follow the trajectory.

$$|\theta_n - \theta_{n-1}| \leq \dot{\theta}_{max} \cdot \Delta T \quad |\theta_{n-1} - 2\theta_n + \theta_{n+1}| \leq \ddot{\theta}_{max} \cdot \Delta T^2 \quad (4.23)$$

Equations 4.23 impose linear constraints on the maximum pitch rate and on the maximum pitch acceleration, calculated using first and second derivatives of finite difference method respectively.

The initial pitch angle of the first stage must equal the launch pitch: $\theta_0 = \theta_{launch}$, while the final pitch must match the second stage's initial pitch, calculated via PEG: $\theta_{end} = \theta_{0,2^{nd}stage} = \sin^{-1}(fr_0)$.

For optimization reasons, the PEG trajectory is not propagated throughout the process. The PEG algorithm is run only at second stage's initial point, assuming that the calculated burn time and ΔV are accurate.

Fairing detachment The fairing is jettisoned when the aerothermal flux gets below $1135W/m^2$ ^[22].

The aerothermal flux (ϕ) is calculated as: $\phi = \frac{1}{2}\rho V_{air}^3$

GA Trajectory For the GA, the trajectory has to be optimized tens of thousands of times, making computational time crucial. However, it's important to still have representative results for both aerodynamic loads and the required ΔV . To achieve this, the 2D trajectory model has been used, with no coasting, optimizing the pitch at 6 equally distributed points during the first stage burn time. C_D , C_L and Thrust are computed 30 times between each trajectory point to reduce computational time.

To estimate the plane change losses, $v_{x,rem}$ and $v_{y,rem}$ are calculated using equations 4.21 and considering the earths rotation at the launch latitude as the initial velocity.

The plane change ΔV can be estimated as:

$$\Delta V_{pc} = \sqrt{v_{x,rem}^2 + v_{y,rem}^2} - v_T \quad (4.24)$$

The ΔV of the second stage is estimated with PEG and it's trajectory is not propagated. The final ΔV and propellant mass remaining in the second stage can be computed as:

$$\Delta V_{total} = \Delta V_{stage,1} + \Delta V_{stage,2} + \Delta V_{pc} \quad m_{prop} = m_{stage,2e} e^{-\frac{\Delta V_{stage,2} + \Delta V_{pc}}{Isp2g0}} - m_{dry,2} \quad (4.25)$$

Additionally the trajectory outputs the aerodynamic loads, thrust, AOA and remaining propellant at $max(q)$ and $max(q\alpha)$.

Full Trajectory Once the GA is converged and a design is chosen, the full 3D trajectory can be computed. This trajectory also takes into account the coasting phases after detachment from the aircraft and after second stage separation. During the first stage pitch is determined by linearly interpolating the pitch points, while yaw is determined by the azimuth calculation.

It was initially considered to use significantly more points (100-200) than in the 2D trajectory. However, it was found that this led to the optimizer converging to non-optimal local minima. By reducing the number of points the optimizer is capable of finding the global minimum. It was observed that using a smaller number of points (4-20) there is no noticeable difference in the trajectory, so it has been decided to use 6 points, as in the 2D trajectory.

As computational time is not concern, many parameters, such as C_D , C_L and Thrust, are computed at each time step of the integration to increase fidelity. Once the first stage trajectory is optimized, the second stage is propagated all the way to burnout, computing the pitch angle with PEG and yaw with the azimuth calculation. At the end the position and velocity vectors are used to compute the orbital parameters and to check orbit insertion accuracy, while the remaining propellant mass is considered to assess the feasibility of trajectory and re-entry.

4.6.3 Possible Orbits

To analyse the market reach of the launcher, all possible circular orbits heights are calculated as a function of payload mass and orbit inclination. This is done using the 2D trajectory for a specific payload and

orbit, calculating the required plane change ΔV to assess whether the rocket will have enough propellant left to return or not. Two additional cases are also computed. One where only the first stage is recovered, in which the second stage recovery system is removed and there is no left over propellant at the end; another one where no stage is recovered, in which the first stage recovery system is also removed.

4.6.4 Monte Carlo Analysis

Using the 3D trajectory a Monte Carlo analysis is done to analyse the feasibility of the design. The goal of the analysis is to estimate what is the likelihood that the preliminary design will be able to complete the mission without any major modifications to the design. The expected difference between the preliminary and real values of C_D , C_L and first and second stage Thrust and I_{sp} ^[60] are used to create the population of multipliers for the simulations. The following 2σ variations are used for the inputs:

| | C_D | C_L | T_1 | T_2 | $I_{sp,1}$ | $I_{sp,2}$ |
|-----------|-------|-------|-------|-------|------------|------------|
| 2σ | 20% | 20% | 8.6% | 8.6% | 3.08% | 3.08% |

Additionally the I_{sp} modifiers are bounded to a maximum increase of 2%, as significant increases in the real I_{sp} compared to the preliminary value are not feasible. The 3D simulation is performed using the nominal optimized trajectory with the rocket's parameters modified by a population of multipliers.

4.7 Structural Analysis

The structural analysis was performed on a simplified launcher model, as explained in Section 4.4. This approach was chosen to address two key challenges: accurately accounting for all structural components (e.g., tanks, intertanks, interstages, skirts) while ensuring adaptability to design modifications arising during development. To achieve this, the five regions —fairing, 1st and 2nd stages, 1st and 2nd interstages— were defined to be as generic as possible, independent of their specific components. The objectives of this block are to compute the internal forces and moments based on trajectory loads, and use these results to size the structural elements effectively.

The launcher is divided into five general regions, each characterized by a center of mass determined by the allocation of all masses within that region. Using trajectory data, the internal forces and moments at the interfaces of these regions are calculated. For structural sizing, every component within a region is designed to withstand the maximum internal action identified, and the thickness of each component is determined based on its material properties. Additional considerations are applied to account for buckling, with distinctions made between pressurized and non-pressurized components. Finally, the sizing is refined by selecting the thickness required for the worst-case scenario for each component, and the corresponding mass is calculated.

It can be noticed that this procedure overestimates the masses of the components inside the stage region, since the maximum internal action of the whole stage is the sizing quantity for each structural component. For this reason, correction factors have been applied to the MERs to get closer to the ones computed after the structural analysis (see Section 4.4).

4.7.1 Loads Estimation

Concerning the loads computation, the procedure is the one described in Section 4.7. The team has decided to calculate only in-flight loads, considering in particular the worst case scenarios. This latter computation is sufficient because these conditions inherently encompass the most critical structural and aerodynamic forces experienced during the vehicle's mission. During in-flight phases, the rocket is subjected to dynamic pressures, aerodynamic forces, thrust and inertial loads that are significantly higher and more variable than those encountered during ground operations or the release phase from the carrier aircraft.

By focusing on worst-case in-flight scenarios, namely the maximum dynamic pressure (Max-Q), and the Max ($q\alpha$): (Maximum angle of attack · dynamic pressure) conditions the analysis captures the most demanding load conditions. These scenarios dictate the structural integrity, stability, and performance of

the rocket, ensuring that the design margins are adequate for all operational conditions without the need to analyse less critical loading phases separately.

Loads are then computed considering the free-free Timoshenko beam model with no constraints. Following the same approach found in literature^[61], first the overall load factors has been computed along the rocket from the External forces coming from aerodynamics and trajectory blocks. After that, with the contribution of inertial forces, the axial force, the internal normal force and the bending moment are computed all along the length of the launcher. It is worthy of notice that all the positions of the centre of masses of the five different sections and the positions of the centre of pressure of the aerodynamic forces are computed from the nose tip towards the end of the rocket. Furthermore, for the sake of simplicity only the Axial and Normal aerodynamic forces of the nose and of the fins are evaluated. Finally, a contribution of control moment has to be applied near the end of the launcher in order to have zero-moment condition at the very end.

Thickness and Fairing sizing To compute the thickness of every structural component, each section (as described in Section 4.4) has been modelled as a cylinder, supported by the fact that the diameter is constant through the stage; for what concerns the interstages, that in reality are cone frustums, an average diameter between the major and the minor base has been used.

For every stress σ computed, by imposing the material's allowable stress $\sigma_{material}$ the minimum viable thickness t required to resist (with a safety factor SF) has been computed to avoid failure in the worst case scenario. The complete procedure for the sizing of the thicknesses can be consulted in Appendix I.1.

Once the fairing shape is defined in Section 3.2, it becomes crucial to correctly size the fairing by analysing the materials and thicknesses to ensure both structural integrity and minimal weight. The team examined several aerospace references, particularly the Atlas V rocket's payload fairing^[62] and the Ariane V^[63]. Based on these references, the team selected carbon-covered aluminum honeycomb panels as the core material for the fairing structure, with a thickness of 2 cm. The main features of this particular material are the enhanced durability and resistance to external thermal and aerodynamic stresses, and the extremely low density ($\rho = 125 \frac{kg}{m^3}$). The thickness selected was found to be optimal for withstanding the stresses the fairing is subjected to, while minimizing the overall weight^[64].

Once defined material, density and thickness, and knowing the lateral surface, the mass of the fairing has been computed.

4.7.2 Finite Element Analysis

A simple finite element analysis is done on the final configuration of the rocket using a modified 6DOF (x , y and θ for each node) Timoshenko Beam model. The rocket is modelled as a cantilever beam fixed at its base (the thruster), a lateral control force is considered in the thruster to cancel turn moments. Some elements of the rocket (such as payload, engines, tank bulkheads, wiring, etc) are considered as point masses, while the propellant and external structure are considered as distributed masses. The aerodynamic loads are considered in their respective positions (nose and fins). The acceleration is computed to calculate the dynamic loads from all the masses. The tank pressure is calculated at each point inside the tanks as the sum of the ullage pressure and the hydrostatic pressure. The internal axial forces from the tank's pressure are considered as forces acting on the bulkheads while the circumferential stresses are taken into account in the stress post-processing.

The rocket is divided into the previously detailed 5 sections which are then refined into many sub-sections. For the conical sections (nose cone and interstages) the diameter is constant in each sub-section but they are staggered to approximate the conical section.

4.8 Recovery System

The recovery system of the launcher is designed to preserve key components while maximizing the ROI. A HIAD-based recovery is selected, inspired by ULA's Sensible Modular Autonomous Return Technology (SMART) concept. Some studies^{[20][18]} show that recovering only the key components of the rocket could become profitable with fewer launches with respect to other strategies, such as a vertical landing recovery.

The recovery follows the design proposed in a article^[65] from Aerospace Science and Technology.

First Stage Recovery For the first stage, only the engines are recovered, as they constitute over 50% of the stage cost for liquid propulsion systems^[18]. After stage separation, the tanks and engines are detached via a separation mechanism, with the recovery system positioned on the engine block using an adapter. The system shall have its own ADCS composed of an IMU and a ring of cold gas thrusters around the adapter. This is needed to dampen the rotational motion of the system after separation and it will also keep Angle of Attack (AoA) fixed once the aeroshell has been deployed.

At an altitude of 100 km the aeroshell will be inflated through its own Nitrogen tank and will begin the re-entry phase with a fixed AoA of -20° as it has been shown^{[65][66]} to allow the stagnation point of the dynamic pressure to be in the centre of the heat shield. Once the system reaches an altitude of 10 km the aeroshell begins deflating in a precise manner to control the aerodynamic coefficients enough to perform a 180° slew. Following ejection of the aeroshell, the engines free-fall briefly before a drogue parachute deploys at 8 km, slowing the system to 27 m/s. At 6.5 km, the parafoil deploys, initiating engine gliding. At 4 km, a helicopter aligns with the target for MAR, using a non-clamping hook stabilized with a drogue basket.

Second Stage Recovery As seen in the HULA concept, HIAD recovery systems may be used for the second stage of an orbital launcher. After deploying the payload the second stage of the launcher will perform a slew of 180° using the system's cold gas thrusters and perform a retrograde burn to lower its perigee to 80 km. Once close to the perigee a second burn is done to slow the spacecraft down even more to avoid skipping on the atmosphere. The next steps of the recovery follow closely what was detailed for the first stage, with the opening of the inflatable aeroshell followed by the drogue and parafoil. The second stage is also recovered through a MAR using a helicopter.

HIAD Sizing The sizing for all the components of the HIAD follows closely the dimensionless approach used by NASA^[67] were the equations are reported in Figure J.3. The size of the inflatable aeroshell is determined by fixing the diameter of each toroid (D_{Tor}), the diameter of the heat shield (D_{HS}), the half-cone angle (θ) and the number of toroids (N) used as seen in the equation below.

$$D_{HIAD} = D_{HS} + D_{Tor} \cdot [(2N - 1) \cdot \sin(\theta) + 1 - \cos(\theta)] \quad (4.26)$$

The 2D trajectory of the system is then propagated, taking into account the effects of drag and lift as seen in section 4.5. First the pressure needed to inflate the shell is computed, followed by the mass of the gas required. The masses of the system are then computed through the use of the dimensionless parameters multiplied as seen in the following equation:

$$m = \frac{m_{dim} \cdot q_{max} \cdot A_{IAD} \cdot C_D}{g_0} \quad (4.27)$$

Where q_{max} is the maximum dynamic pressure experienced by the system, A_{IAD} is the area of the inflatable aeroshell, C_D is the drag coefficient of the aeroshell at maximum dynamic pressure. The mass of the adapter and separation mechanism was sized considering respectively 7.5% and 3.25% of the mass to be recovered^[68]. The tank containing the inflation gas can be sized knowing the pressure needed in the shell and applying a safety factor of 100 to obtain the tank pressure. Once the material is set the thickness can be computed as well as the tank's mass.

Parachute Sizing The parachute phase of the recovery was sized based on a pure energetic point of view to compute the masses of the system enough to slow down the recovery by a certain ΔV within a certain Δh . This is done by computing the required acceleration and then, knowing the C_D of both the drogue and the parafoil^[69] it is possible to estimate the needed area.

$$A_{drag} = \frac{2m_{rec} \cdot a_{rec}}{\rho_{air} \cdot C_D \cdot v^2} \quad (4.28)$$

Where m_{rec} is the mass to be recovered, A_{drag} is the drag area of the parachute, C_D is the drag coefficient of the parachute and a_{rec} is the required acceleration. The mass of both the parafoil and the drogue can now be computed by knowing the parachute's thickness and density. The formulas used for the recovery

and the data used for this computation is better explored in subsection J.2.

Mid-Air Retrieval Finally, the system is safely recovered through a Mid-Air Retrieval using a civil high-load helicopter. The selected helicopter is the Sikorsky S-92^[70] with an external load capacity of 4500 kg, enough to recover both the stages. The MAR will begin at an altitude of 4 km, where the helicopter will align with the sail trajectory and lower a non-clamping hook to perform the attachment. The hook is suspended from a cable and stabilised with a drogue basket and attaches itself to a secondary parafoil positioned on top of the main parachute at an altitude of approximately 1.5 km.

4.9 Optimal Configuration Choice

After optimizing all configurations using the described MDO approach, selecting the one with the lowest GLOM alone is insufficient, as other critical factors must be considered. To address this, a weighted KPIs is evaluated for profitability, reusability, time to market, design inefficiency, and environmental impact. The weights for these KPIs are determined through project requirements and insights from the House of Quality analysis. The optimal configuration is then identified using Pareto optimality, balancing GLOM and the weighted KPI score.

4.9.1 Key Performance Indexes

The KPIs are chosen to align with project requirements and ensure a comprehensive evaluation of each configuration. Profitability is prioritized, reflecting the need for a quick break-even point (BEP) with minimal launches, a key project goal. Reusability is included as a mandatory requirement and for its role in reducing long-term costs. Time to Market emphasizes delivering a functional system within 4–5 years, while environmental impact, though not a strict requirement, encourages sustainable solutions. Design inefficiency penalizes configurations with potential feasibility challenges. The overall score is computed as:

$$KPI = 0.5KPI_{profit} + 0.15KPI_{reusability} + 0.2KPI_{ttm} + 0.05KPI_{toxicity} + 0.1KPI_{design} \quad (4.29)$$

For a more detailed analysis on the computation of each KPI, refer to Appendix L, where the complete methodology is outlined.

Profitability Following a review of the literature^{[53] [71] [72]}, the profitability KPI has been defined as:

$$KPI_{profit} = w_{BEP}R_{BEP} + w_{TTP}R_{TTP} + w_{TNP}R_{TNP}$$

where R_{BEP} , R_{TTP} , and R_{TNP} are normalized indices for the break-even point in launches, the time to profit in days, and the total net profit (in million USD), respectively.

The break-even point is computed as:

$$N_{bep} = \frac{IC}{NP_{\text{per Launch}}}$$

where IC includes development, production^[73], and R&D costs, with production estimated at \$45,000/lb to orbit^[53]. The revenue per launch is based on \$15,000/kg, a price deemed competitive in comparison to other launch providers^[74], with N_{bep} constrained to ≤ 8 launches before a new LV has to be produced. The time to profit index accounts for launch frequency:

$$TTP = \frac{N_{bep}}{f_{\text{launch}}}, \quad f_{\text{launch}} = \frac{365}{t_{\text{turnAround}}}$$

where $t_{\text{turnAround}}$ increases with complex propellants or full composite structures, delaying profitability.

The total net profit evaluates cumulative gains over the whole 8 launches:

$$TNP = (NP_{\text{per Launch}} \cdot 8) - IC$$

It is adjusted for maximum payload capacity of each configuration at a reference 300 km LEO orbit, penalizing inefficiencies from high dry mass or recovery systems. The simplified assumptions help maintain consistency in the evaluation of all configurations, making it easier to compare their profitability and gain insights into which ones are more financially viable.

Time to Market The Time to Market KPI evaluates the feasibility of fully developing a reusable LV within 4–5 years, considering three factors: propellant couple, materials, and compatibility with an aircraft carrier (AC). It is computed as:

$$KPI_{ttm} = 0.4R_{couple} + 0.3R_{materials} + 0.3R_{compatibility} \quad (4.30)$$

The R_{couple} index favours configurations with the same propellant for both stages, as scaling a single engine is faster; LOX-RP1 configurations also benefit from previous industry experience (e.g., LauncherOne). The $R_{materials}$ index penalizes full carbon composite structures due to slower production, while aluminum alloys allow faster development. Lastly, $R_{compatibility}$ rewards lightweight structures and semi-cryogenic propellants (e.g., LOX-RP1) for easing aircraft integration and operations.

Reusability The Reusability KPI evaluates recovery efficiency using two factors: the recovery system mass fraction (R_{rec}), which is the ratio of the recovery system mass to the total mass recovered, and the reentry burn mass fraction (R_{prop}), which is the ratio of the propellant mass for reentry to the total propellant mass of the second stage. Configurations with lower values of R_{rec} and R_{prop} score higher, as they maximize payload delivery and minimize recovery weights. The KPI is computed as:

$$KPI_{reuse} = 0.6R_{rec} + 0.4R_{prop} \quad (4.31)$$

Design Inefficiencies This KPI measures deviations from optimal design targets. The propellant ratio ($m_{PropRatio}$, which is the ratio between propellant left after the ascent trajectory and the propellant needed for the re-entry burn) targets a value of 1, which minimizes excess propellant. The filling factor of the fairing ($V_{filling}$) aims for 80% utilization, while structural efficiency (ε) penalizes high inefficiencies in the first and second stages. The overall KPI is defined as:

$$KPI_{design} = \frac{w_1 \frac{1}{m_{PropRatio}} + w_2 (1 - |V_{filling} - 0.8|) - w_3 \left(0.5 \frac{\varepsilon_{s1}}{\varepsilon_{s1\max}} + \frac{\varepsilon_{s2}}{\varepsilon_{s2\max}} \right) + c}{w_1 + w_2 + w_3 + c} \quad (4.32)$$

Toxicity The Toxicity KPI considers emissions of CO , CO_2 , and black carbon (BC) for each propellant combination^[75]^[76]. Emission factors are multiplied by the total propellant mass, with CO_2 emissions weighted more heavily for their long-term environmental impact. The KPI is defined as:

$$KPI_{toxic} = 0.4E_{CO_2,x} + 0.3E_{CO,x} + 0.3E_{BC,x} \quad (4.33)$$

4.9.2 Pareto Optimal Solution

Given all feasible solutions in terms of:

$$\xi = [\text{GLOM}_i, KPI_i] \quad \text{for } i = 1, \dots, 12$$

It has been decided to use the Pareto optimality algorithm to select the best configuration, a common approach in Multidisciplinary Design Optimization (MDO)^[77]. To define the Pareto frontier, all non-dominated solutions must first be identified. A solution A is dominated by solution B if for all objective functions, the value in A is always worse (or equal) than in B .

Next, to select the best solution, the Utopia point method is employed, as suggested in the literature^[78]. The Utopia point is the vector of single minima for each objective function, representing the ideal solution. Since no configuration matches the Utopia point exactly, the selected configuration is the one with the smallest distance from it, offering a simple yet effective method for the final selection. Finally, since Pareto optimality aims to find a solution that minimises both the objectives, the inverse of the KPIs was taken.

5 Results

This Chapter is dedicated to the delivery of the obtained results; the first section analyses the feasible configurations generated through the MDO method, then the focus shifts only to the selected configuration, going through every block results until the final rocket overall configuration is exhibited.

5.1 MDO results

All the configurations are presented in the summary plot. As illustrated, they exhibit varying dimensions, each of which is directly tied to the specific design features of the respective configuration. For instance, LH₂ configurations feature a longer second stage due to the lower density of liquid hydrogen compared to the other fuels analyzed.

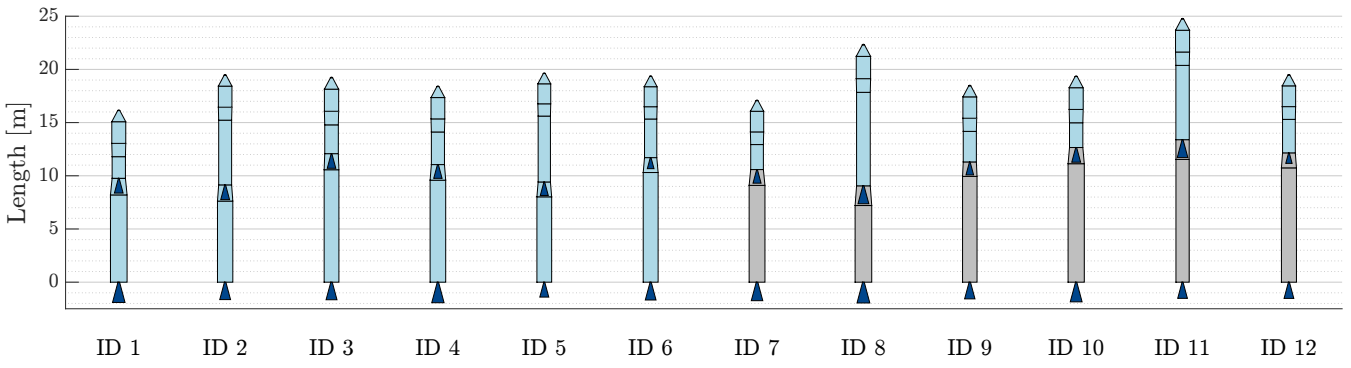


Figure 5.1: MDO configurations

The variables associated with the configurations are summarized in Table 8, providing an overview of the most significant parameters. For a comprehensive list that includes all variables, refer to Appendix C.3.

| ID | 01 | 02 | 03 | 04 | 05 | 06 | 07 | 08 | 09 | 10 | 11 | 12 |
|---------------------|-------|-------|-------|-------|-------|-------|-------|-------|-------|-------|-------|-------|
| $M_{p1}[\text{kg}]$ | 14079 | 11185 | 15002 | 11987 | 8922 | 11933 | 14470 | 12357 | 13468 | 14836 | 10928 | 12690 |
| $M_{p2}[\text{kg}]$ | 2348 | 2396 | 2718 | 3489 | 2260 | 3060 | 2509 | 3954 | 2637 | 2741 | 2767 | 2730 |
| $\varepsilon_2[-]$ | 137 | 98 | 155 | 78 | 121 | 81 | 123 | 82 | 151 | 89 | 115 | 84 |
| $D_1[\text{m}]$ | 1.56 | 1.44 | 1.39 | 1.47 | 1.39 | 1.40 | 1.49 | 1.56 | 1.36 | 1.52 | 1.25 | 1.41 |
| $D_2[\text{m}]$ | 1.25 | 1.22 | 1.28 | 1.23 | 1.16 | 1.16 | 1.19 | 1.29 | 1.24 | 1.25 | 1.25 | 1.20 |
| GLOM[kg] | 18471 | 15628 | 19717 | 17662 | 13094 | 17024 | 19024 | 18927 | 18055 | 19927 | 15977 | 17459 |
| Fuel 1 | RP1 | RP1 | RP1 | LCH4 | LCH4 | LCH4 | RP1 | RP1 | RP1 | LCH4 | LCH4 | LCH4 |
| Fuel 2 | RP1 | LH2 | LCH4 |

Table 5.1: Configurations Optimization Variables

5.2 Final Configuration

As detailed in Section 4.9, the final rocket configuration is determined through Pareto optimality. Figure 5.2 illustrates the points within the Pareto-optimal region, as well as the dominated configurations. The final configuration corresponds to the point closest to the Utopia point, which is identified as Configuration 12. This configuration is characterized by the use of the same propellant pair (LOX-LCH₄) and aluminum for the structural elements and tanks of the first stage.

The rationale behind this selection can be summarized as follows:

- The associated GLOM outperforms most of the other configurations;
- The selected configuration demonstrates the highest KPI among all alternatives.

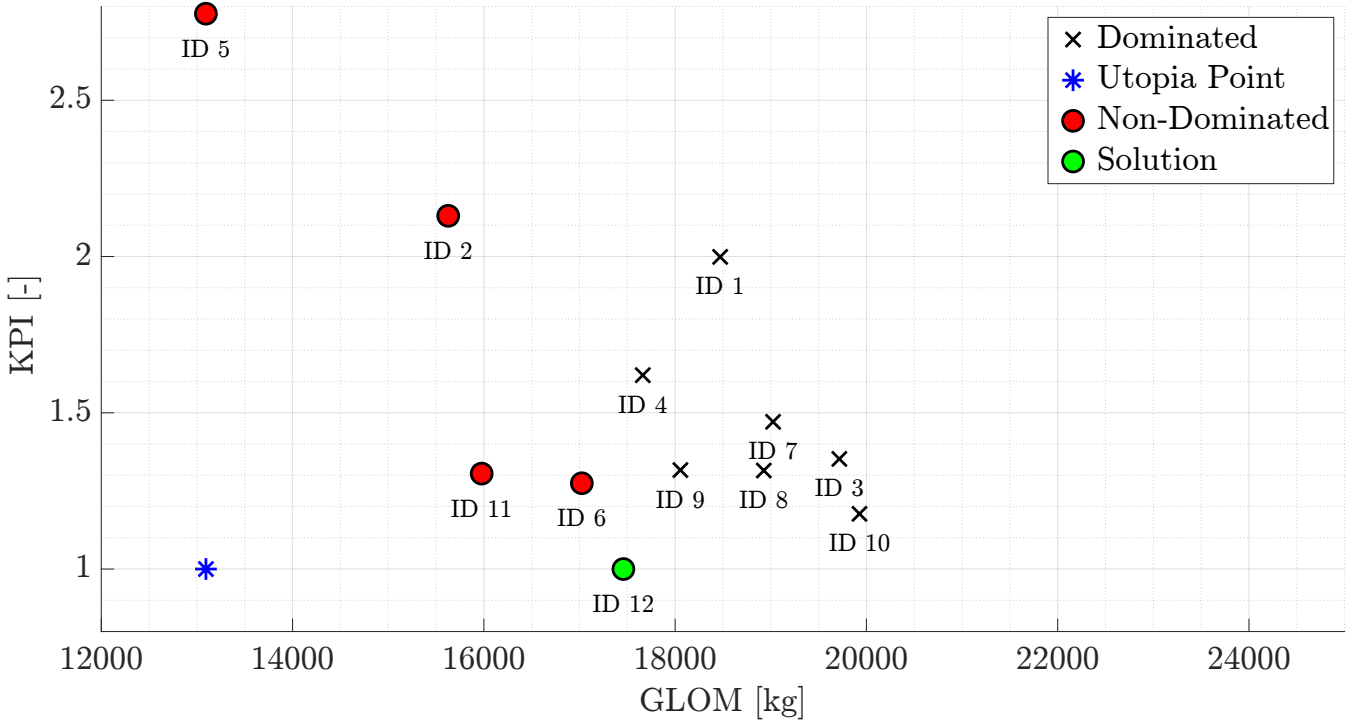


Figure 5.2: Pareto Plot

The KPI value reaches a high level primarily due to the configuration's strong performance in profitability and time-to-market. These two indices were prioritized by the team, as they most closely align with the customer's requirements and pressing needs.

| KPI | Profitability | Time To Market | Reusability | Emissions | Design Inefficiencies |
|-------|---------------|----------------|-------------|-----------|-----------------------|
| Value | 0.9995 | 0.7900 | 0.6329 | 0.5457 | 0.5071 |

Table 5.2: KPI Configuration 12

This configuration allows the team to focus on the development of a single engine, accelerating the readiness for market entry. As illustrated in Figure 32, it requires about 4 launches to achieve the Break-Even Point.

The obtained results are derived from a model based on some preliminary assumptions, encompassing both the individual components and the overall structure of the problem. To enhance the model's accuracy, it was decided to incorporate new, more realistic features. This refinement resulted in adjustments to the launcher's design, ensuring greater precision and reliability in its implementation. The final model novelties begin with the recovery block's complete integration, including also all associated component characteristics and parameters. From the beginning, structural masses were precisely modeled, and verified 3D routes were added to the trajectory analysis. While FEA produced accurate stress evaluations, guaranteeing structural durability, a Monte Carlo analysis evaluated design viability under uncertainty. These enhancements increase the rocket design's overall resilience and authenticity.

Before entering more deeply in the blocks results, the new and improved configuration optimal variables are exhibited in Table 5.3

| CONF | OF ₁ [-] | OF ₂ [-] | TW ₁ [-] | TW ₂ [-] | M _{p1} [kg] | M _{p2} [kg] | z ₁ [m] | ε ₂ [-] | D ₁ [m] | D ₂ [m] | GLOM[kg] |
|--------------|---------------------|---------------------|---------------------|---------------------|----------------------|----------------------|--------------------|--------------------|--------------------|--------------------|----------|
| ID 12 | 3.48 | 3.74 | 1.10 | 0.81 | 13086 | 3619 | 12619 | 115 | 1.57 | 1.26 | 19185 |

Table 5.3: Final Configuration optimal variables

As observed, the optimal variables reveal significant variation, yet they remain within the defined bounds set in Appendix B.2 and yield plausible values. This variability can be attributed to the nature of the

optimization process conducted using the genetic algorithm. The algorithm is designed to provide an initial optimal, albeit not definitive, solution, which requires further refinement and enhancement, as subsequently performed by the team.

5.3 Propulsion Results

In Table 5.4, the engine characteristics are presented, with results aligning well with literature for the first stage^[79]. The slightly higher ε for the first stage is attributed to the imposed P_c and optimization for operation at approximately 13 km altitude. Regarding the results obtained for the second-stage engine, $I_{sp,vac}$ is slightly lower than expected. This outcome is attributed to the conservative choice of a lower P_c for the second stage, that has led to reduced performances. Adjusting P_c in future iterations could improve specific impulse and align it more closely with expected values.

| | $I_{sp,opt}$ [s] | T_{opt} [kN] | $\varepsilon[-]$ |
|---------------------|------------------|----------------|------------------|
| First Stage | 347 | 265.56 | 92 |
| Second Stage | 361 | 42.29 | 115 |

Table 5.4: Propulsion results: optimal condition for second stage is vacuum

5.4 Aerodynamic Results

This section presents the lift coefficient Figure 5.3 and lift to drag ratio Figure 5.4 as a function of angle of attack, for the most relevant flight conditions (Mach and altitude).

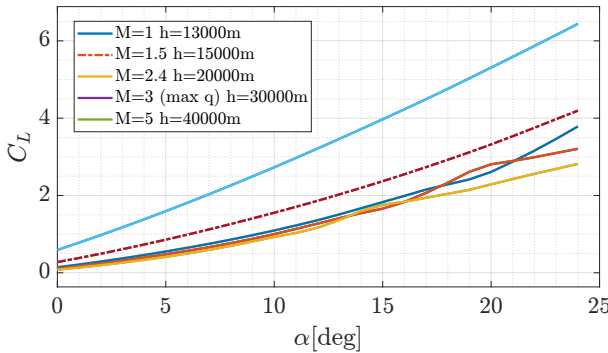


Figure 5.3: Lift Coefficient vs angle of attack

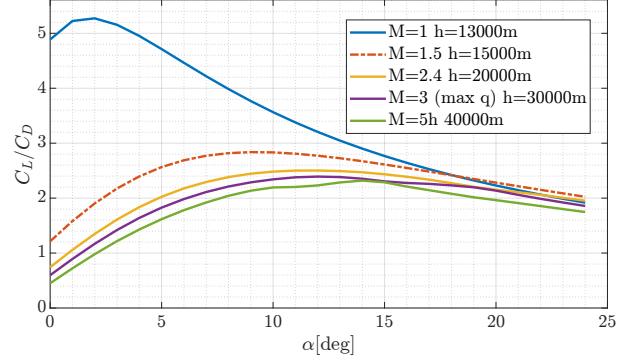


Figure 5.4: Lift to Drag ratio vs angle of attack

The angle of attack remains predominantly between 15° and 18° throughout most of the trajectory Figure 19. At these angles, as the Mach number increases, the peak C_L/C_D shifts closer to the trajectory's angle of attack. This enables the exploitation of aerodynamic forces near optimal aerodynamic efficiency while benefiting from higher lift values.

5.5 Stability Results

The reported CP position corresponds to the configuration prior to including the fins. Additionally, the initial total CoM position and the center of pressure location specific to the fins are presented. The fins' semi-span is also provided, representing a carefully selected value that ensures stability during the critical initial moments before engine ignition. Beyond this phase, the TVC system actively stabilizes the rocket throughout its trajectory.

| Parameters | b_{fins} [cm] | x_{CP} [m] | $x_{CP,wings}$ [m] | x_{CG} [m] |
|------------|-----------------|--------------|--------------------|--------------|
| Values | 46.3 | 1.96 | 18.53 | 11.93 |

Table 5.5: Stability results

5.6 Trajectory Results

The results from the 3D nominal trajectory can be seen in the following figures, the ground track of the trajectory can be seen in Figure 21. The trajectory of the rocket does not go over land and thus it does not endanger people on the ground.

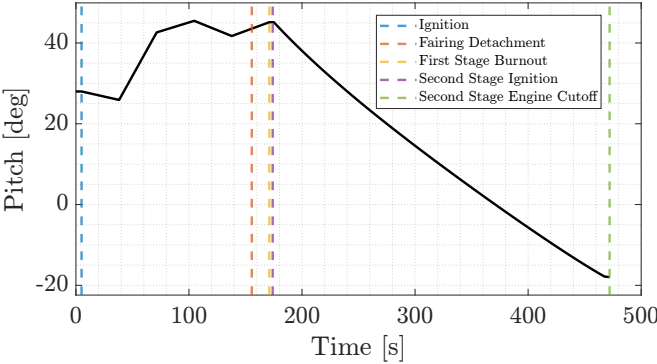


Figure 5.5: Nominal trajectory pitch

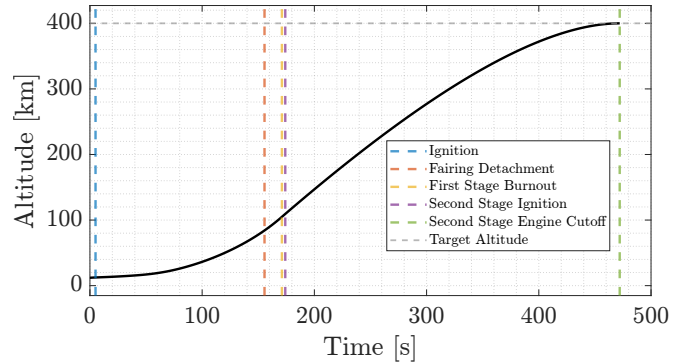


Figure 5.6: Nominal trajectory altitude

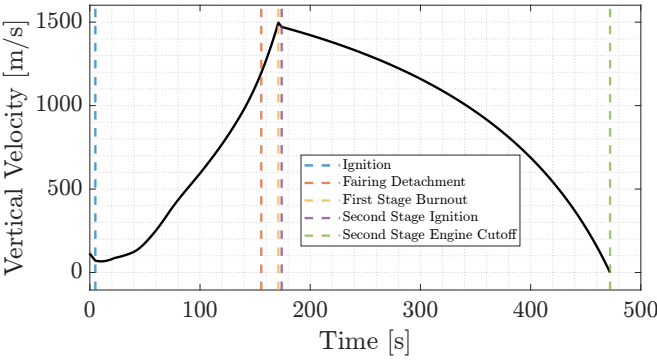


Figure 5.7: Nominal trajectory vertical velocity

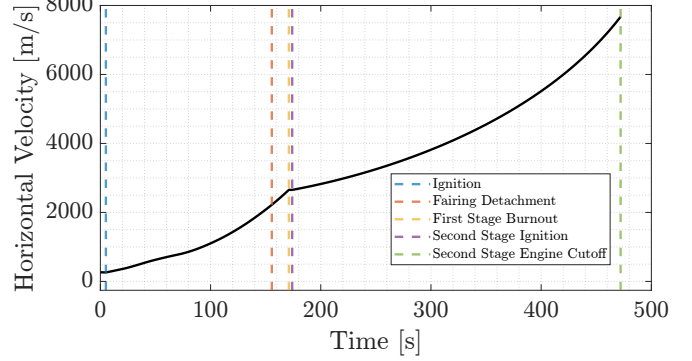


Figure 5.8: Nominal trajectory horizontal velocity

In Figure 5.5 the pitch can be seen for the first and second stage. The first stage pitch was optimized while the second stage pitch is calculated with Power Explicit Guidance. The maximum pitch is relatively low compared to vertical launch vehicles as the horizontal launch position, combined with the launch velocity and low air density means the rocket can use the aerodynamic lift to partially counteract gravity, so it does not require as much vertical thrust and thus minimizes gravity losses. In Figure 19 the angle of attack and Mach number can be seen for the first stage flight.

In Figure 5.6 the altitudes of the different event's can be seen. The rocket is deployed from the plane at 12000m, 5 seconds later at 12458m the first stage engine ignites. At 84255m and 155.58s after deployment the fairing is jettisoned and at 105022km and 171.08s after deployment the first stage engine burns out. There is a 3 second coasting phase until the second engine ignites. Finally the second stage engine is shut off at almost exactly 400km, 472.08s after deployment. The final values of altitude, vertical velocity and horizontal velocity at engine cut-off and the orbit periapsis, apoapsis and inclination are:

| Altitude | Vertical velocity | Horizontal velocity | Periapsis | Apoapsis | Inclination |
|----------|----------------------|-------------------------|-----------|----------|-------------|
| 400km | 0.0m s ⁻¹ | 7672.3m s ⁻¹ | 398.95km | 400.00km | 98.00° |

Although the orbit insertion accuracy seems almost perfect, the model is not considering the attitude control of the rocket and the engine cut-off procedure. Also this model considers that the state vector of the rocket is known with perfect accuracy to calculate the guidance when in reality there will measurement errors.

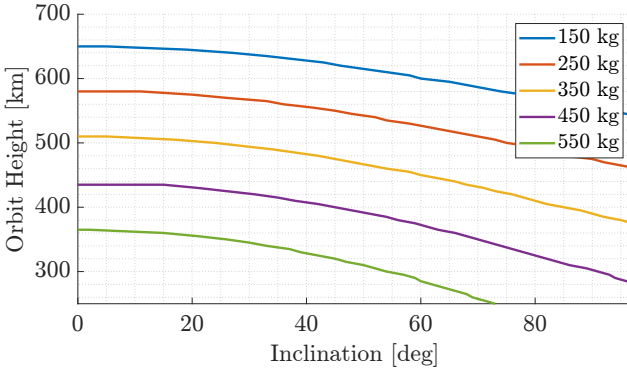


Figure 5.9: Possible orbits with full reusability

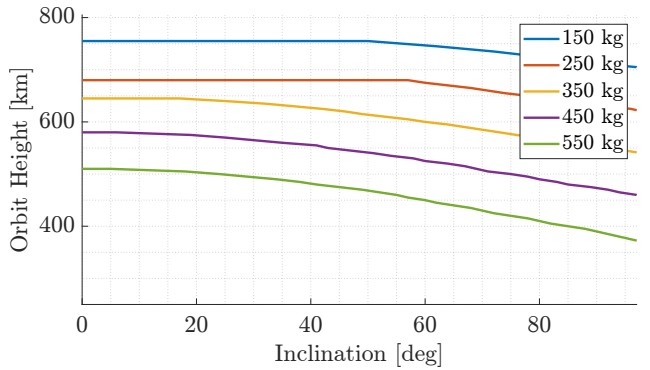


Figure 5.10: Orbit discarding the second stage

In Figure 5.9 all the achievable orbits can be seen as a function of the payload mass and orbit inclination for the fully reusable rocket. For example a payload of up to 450kg could be taken to an orbit of 400km with an inclination of 51.6°, this is the orbit of the International Space Station.

In Figure 5.10 are the achievable orbits when the second stage is not reused. There is a notable increase in the orbits that can be achieved, a payload of 500 kg could be taken to a 400km SSO, assuming the payload fits within the fairing, this is double the payload capacity of the fully reusable rocket. This comes with a significant cost as the second stage is lost but it could make economical sense for heavier payloads that could not be launched otherwise.

In Figure 18 are the achievable orbits when the first stage propulsion unit is not recovered. Even more orbits are reachable than the case recovering the first stage, however the increase is marginal and it would not make economical sense to fly the rocket in this configuration.

5.7 Structure Results

First this section presents the results of the loads analysis. Figure 5.11 illustrates the axial loads and bending moments calculated using the procedure outlined in Section 4.7. Similarly, Figure 5.12 displays the corresponding loads obtained from the FE analysis.

The difference between the two results primarily arises from how the tank pressure is accounted for in the analyses. In the FE analysis, the tank pressure is treated as an external load, whereas, in the classical method, it is incorporated into the stress computation. Additionally, discrepancies in the computed moments are influenced by the differing levels of approximation: the classical method approximates the structure into five sections, compared to 170 sections in the FEA. This coarser approximation, combined with differences in mass distribution, leads the classical method to misestimate the actual loads acting on the structure.

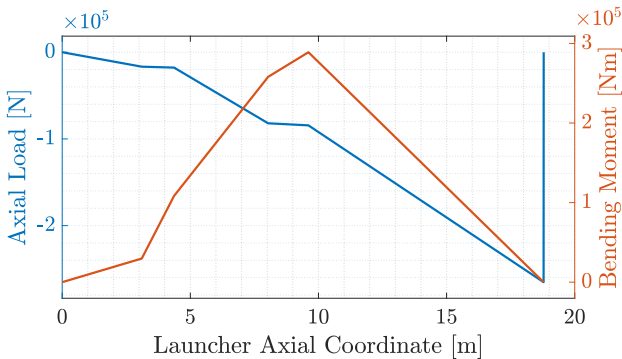


Figure 5.11: Axial Force and Bending Moment estimation

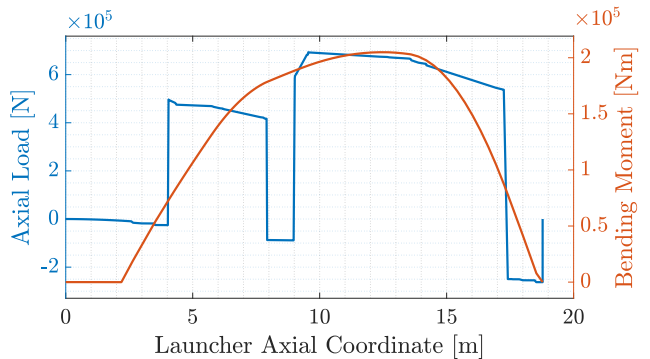


Figure 5.12: Axial Force and Bending Moment with FEM analysis

5.7.1 Finite Element Analysis

In Figure 5.13 the deformed model of the rocket can be seen with a Von Mises stress map. The displacements have been amplified by a factor of 20 to make them visible. Although the beams are 1D, the Timoshenko beam model allows to calculate stresses in 3D for axisymmetrical geometries, so they can be represented on the surface of this 3D model. The maximum stresses occur at the bottom of the first stage fuel tank. It's noticeable how the stresses are higher at the bottom of the tanks, this is due to the hydrostatic pressure. The stresses are higher at the side that is in tension by the bending, this is the bottom side, while the compression bending relaxes some of the stresses on the tanks.

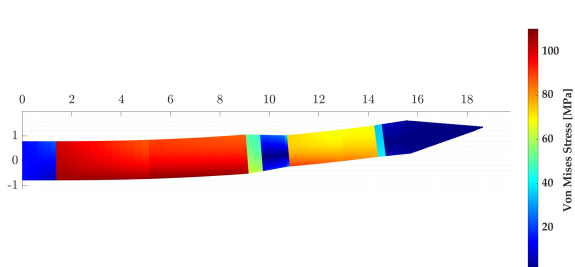


Figure 5.13: Displacements and stresses map on the rocket

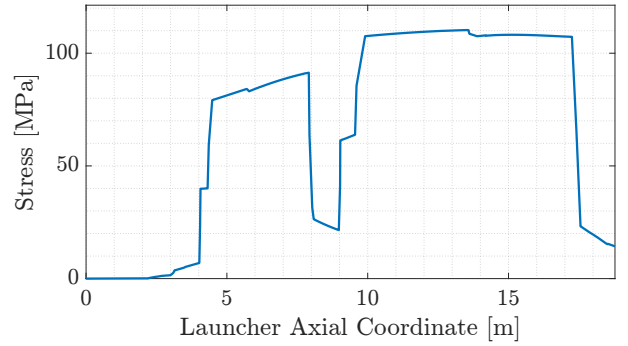


Figure 5.14: Maximum Von Mises stresses

In Figure 5.12 the maximum Von Mises stresses along the rocket is plotted. As it can be seen the stresses are much lower than the yield stresses of each section (965 MPa for Carbon-Composite and 503 MPa for Aluminum), this is expected as the critical factor for all sections was buckling.

5.8 Recovery Results

The simulation of the system's recovery is performed once the final mass of the project is computed and shows promising results. For the first stage a 4-toroid HIAD is enough to slow the system enough and the limiting factor is the acceleration perceived by the stage. Although the acceleration would be too high for the recovery of tanks, for the recovery of only the engine block these values are acceptable^[20]. For the second stage on the other hand the limiting factor is the heat flux perceived by the heat shield, as the acceleration values are low enough to grant the recovery of the whole second stage. The heat flux, although high, has been verified as accurate^[17] and the thickness of the ablative material is enough to counter the heat flux absorbed. The accelerations of the first and second stage are reported in Figure 5.15 and Figure 5.16.

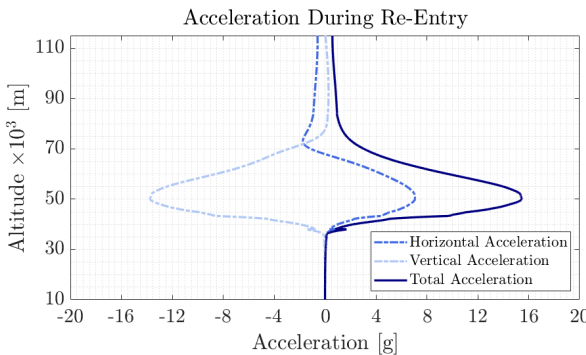


Figure 5.15: Acceleration perceived by the first stage

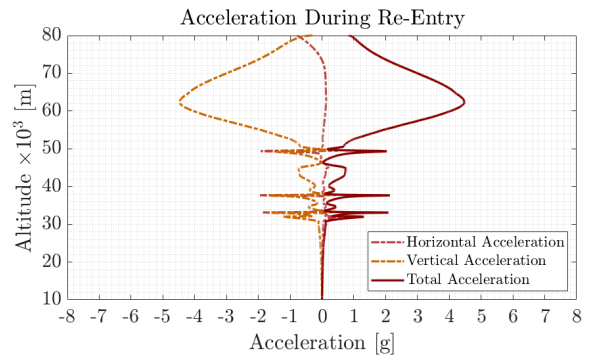


Figure 5.16: Acceleration perceived by the second stage

5.9 Final Sizing Results

This section is dedicated to the exhibition of the final dimensions, masses and thicknesses of the launcher. From the initial estimation of the masses provided by the Mass Estimation Relation (MER), the masses of the structural components computed after the structural sizing have been updated; these masses have been used in a second iteration of the final design loop, in substitution of the respective components from the MERs. The fins have been inserted, too (since in the first iteration their mass was not been estimated, being negligible with respect to all the other components). After this, the trajectory has been computed again, and so the entire loop until conclusion. Convergence of the values of inert masses has been assessed in the second iteration, with a tolerance of 1 kg. The values reported in Table 5.6 are the definite final ones.

| Component | Thickness[mm] | Mass[kg] | Length[m] | Max Diameter[m] |
|-------------------------------|---------------|----------|-----------|-----------------|
| Fairing | 20 | 33.6 | 3.1 | 1.32 |
| Second Interstage | 7.5 | 59.9 | 1.25 | 1.25 |
| Second Stage LCH4 Tank | 3.8 | 39.4 | 1.70 | 1.25 |
| Second Stage LOx Tank | 3.8 | 58.1 | 2.18 | 1.25 |
| Second Aft Skirt | 7.2 | 32.7 | 0.73 | 1.25 |
| First Interstage | 6.2 | 121.1 | 1.57 | 1.57 |
| First Stage LCH4 Tank | 3.7 | 202.7 | 3.92 | 1.57 |
| First Stage LOx Tank | 3.6 | 262.9 | 4.87 | 1.57 |
| First Aft Skirt | 6.8 | 149.2 | 1.57 | 1.57 |
| Fins | - | 4.6 | - | - |
| Wiring & Avionics | - | 101.9 | - | - |
| First Stage Engine Block | - | 425.8 | - | - |
| Second Stage Engine Block | - | 120.4 | - | - |
| First Stage Recovery | - | 202.8 | - | - |
| Second Stage Recovery | - | 184.7 | - | - |
| PAF | - | 68.9 | - | - |
| First Stage Insulation (sum) | - | 48.2 | - | - |
| Second Stage Insulation (sum) | - | 17.7 | - | - |

Table 5.6: Final Launcher Design Results

| | Mass[kg] | Length[m] | $\varepsilon_{s1}[-]$ | $\varepsilon_{s2}[-]$ |
|-------|----------|-----------|-----------------------|-----------------------|
| Total | 19185 | 18.79 | 0.10 | 0.16 |

Table 5.7: Overall Mass and Structural Mass indexes

It can be seen from Table 5.6 that the most important contribution to the inert masses of the launcher are given by the tanks of the first stage (which are biggest ones), the engine blocks (consisting of engine, TVC, thrust structure) and the recovery blocks masses. In a future development, a more advanced investigation about the items containing the recovery structures (i.e. first stage aft skirt and second interstage) should be performed, with a more accurate allocation of the recovery volumes inside these components. Furthermore, it can be noted that half of the components do not have a thickness, since they have been considered as point masses; future developments should integrate these components in a more precise and realistic way into the structural analysis.

6 Analysis Of Results and Requirements Compliance

The main objective of this study was to carry out the preliminary design of a reusable airborne launcher. The analysis was done by the team using a Multidisciplinary Design Optimization (MDO) approach, that enabled the evaluation of multiple configurations. The results demonstrate that feasible designs were obtained for all configurations, with optimization variables yielding practical and expected outcomes. The final configuration aligns well with expectations: the *OF* ratio is near optimal, the *TW* is appropriately higher for the first stage, and the propellant mass supports reasonable structural efficiency values (ε_s). Moreover, since the optimal configuration was chosen according to the key performance indexes, it is crucial to assess the compliance with mission requirements and customer needs. The reusability requirements, for both stages, have been fulfilled by adopting an innovative solution that aims to guarantee a fast return on the initial investment. Although full recoverability was not achieved for the first stage, the adopted approach proved economically viable, requiring relatively few launches to break even.

For the requirement on a time to market of under four years, even if the adopted solution comprises not yet flight-proven technologies in airborne launchers' field, the choice of the same propellant couple and the rising adoption of LCH₄ in the liquid propulsion framework, provide confidence in achieving engine validation within the timeframe. Furthermore, the integrated recovery technology has already flight heritage and the materials chosen for the structures are widely used. Finally, the orbit insertion accuracy requirement has been successfully met, as detailed in section 5.6.

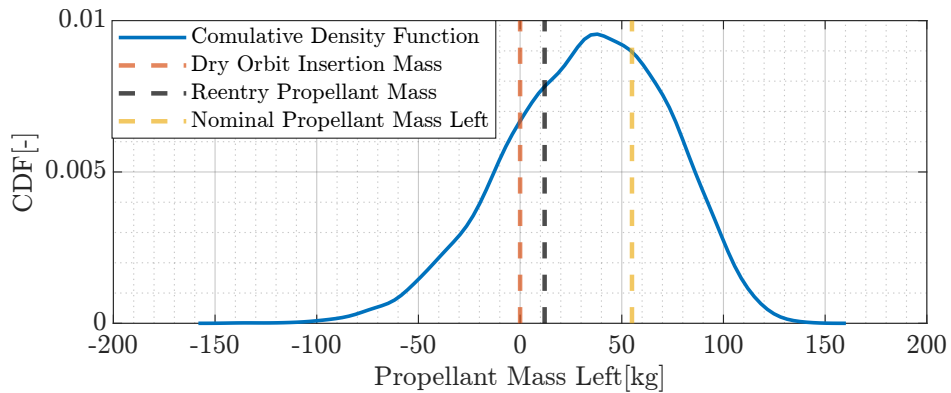


Figure 6.1: Remaining propellant mass of monte carlo population

In Figure 6.1 results of the Monte Carlo simulation show the probability distribution of remaining propellant mass after reaching orbit. Three distinct regions can be identified: the cases where there is not enough propellant to reach orbit, the cases where there is enough propellant to reach orbit but not to de-orbit the second stage and the cases where the mission can be done successfully. The probabilities of each section are:

| Not enough propellant | No de-orbit | Successful mission |
|-----------------------|-------------|--------------------|
| 21% | 8.83% | 70.17% |

The results indicate a probability of 70.17% that the preliminary design will work without any major modifications. There is a 8.83% probability that it will require minor modifications to increase performance. And a 21% probability that major modifications will be required to be feasible.

Although modifications are expected, as the design is only in preliminary phase, there is a high degree of confidence that these will only be minor.

7 Conclusions and Further Developments

The precedent analysis presents the main features of the design of a reusable airborne launcher. By exploring this specialized field of launch vehicle design, the team gained valuable insights into the development and integration of all subsystems involved in the process. Considering the growing interest in flexible, cost-effective and tailored launch solutions for small and nano satellites, reusable airborne launchers could play a more significant role in the years to come, with their advantages in terms of accessibility and operational efficiency.

The MDO approach used to carry out the analysis allowed the team members to gain a deeper understanding on the complexity of the preliminary design of a launch vehicle. Particular emphasis was focused on the coupling between different disciplines in a such complex project. This became particularly evident during the optimisation of different configurations, which required careful tuning of variables to ensure convergence of the optimisation algorithm.

The analysis on the Key Performance Indexes shed light on the importance of the economic and commercial side of developing a launch vehicle. Technical and engineering decisions consistently needed to align with customer requirements and mission objectives, enhancing the flexibility of the team members to this aspect of the project.

For further developments and future improvements on the design, the team plans to explore alternative propulsion architectures, such as Solid Rocket Motors and hybrid solutions. Furthermore, the possibility of expanding the design to a three stage vehicle should be investigated. Regarding the carrier aircraft, which currently represents a key limitation in the state-of-the-art airborne launchers, a deeper analysis of the interface with the launch vehicle and the needed modifications that must be applied to the carrier should be carried out. Also the possibility to exploit military resources could be investigated, as this might offer improved performance and capabilities.

Last but not least, from the commercial and economic point of view, a trade-off analysis should be performed to assess the possibility of discarding the recovery of the second stage, in order to enhance the maximum payload capacity of the vehicle. This approach could significantly enhance the vehicle's maximum payload capacity and provide a competitive edge in the growing nanosatellite market, where operators are seeking out to find a cost-effective and accessible way to reach orbit, without having to rely on piggyback solutions.

Appendix

A House Of Quality

The House of Quality structure is presented in Figure 1:

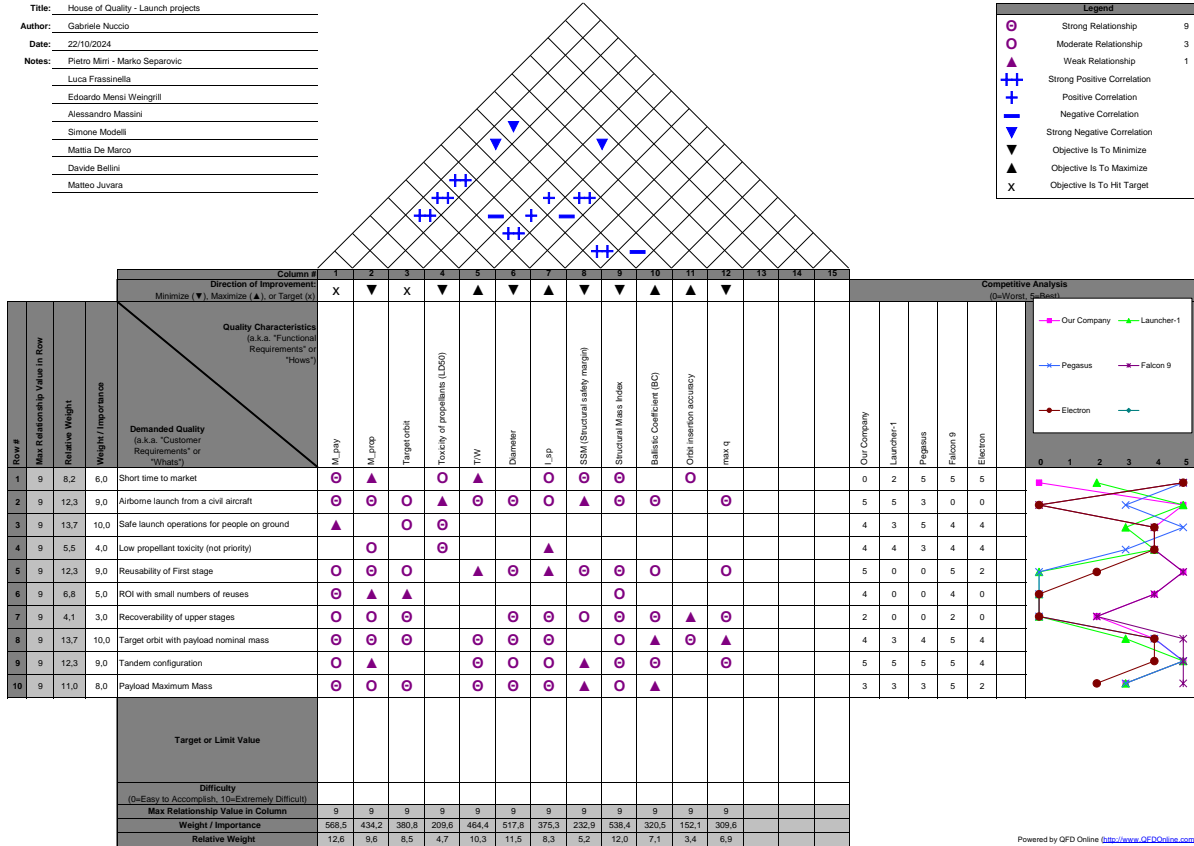


Figure 1: House Of Quality, Re-Heets Launcher

B Baseline Appendix

B.1 Decision Matrix

In this section the decision matrices developed to choose the propellant couples and the external structure and tank materials that will be presented. Both matrices evaluate the inherent features for each possible choice, giving to each of them a weight from 1 to 5 depending on their relevance for the success of the mission. Also a score from 1 to 5 was given in order to conclude the evaluation process.

| | $I_{sp,volumetric}$ | $I_{sp,gravimetric}$ | $M_{dry,tank}$ | Cost | TRL | Availability | Toxicity | |
|------------------------|---------------------|----------------------|----------------|------|-----|--------------|----------|----------------|
| Parameters weights | 4 | 5 | 4 | 1 | 3 | 2 | 4 | 3 Total |
| LOX-LH2 | 1 | 5 | 1 | 4 | 5 | 5 | 5 | 1 3.269 |
| LOX-RP1 | 5 | 3 | 4 | 3 | 5 | 3 | 3 | 3 3.692 |
| LOX-LCH4 | 4 | 4 | 2 | 5 | 3 | 5 | 5 | 2 3.615 |
| N2O4-Aerozine50 | 4 | 3 | 4 | 2 | 5 | 2 | 1 | 4 3.231 |
| N2O4-MMH | 4 | 2 | 4 | 2 | 5 | 2 | 1 | 5 3.154 |
| N2O4-UDMH | 3 | 1 | 4 | 2 | 5 | 2 | 1 | 3 2.577 |

Table 1: Propellant couple decision matrix

| | σ_{yield}/ρ ratio | Manufacturability | TRL | Insulation | Cost | Density | Reusability | |
|-------------------------|-----------------------------|-------------------|-----|------------|------|---------|-------------|-------------|
| Parameters weights | 4 | 4 | 3 | 2 | 2 | 5 | 5 | Total |
| Aluminum-Lithium | 4 | 3 | 5 | 2 | 2 | 4 | 4 | 3.64 |
| 7075 Al Alloy | 4 | 4 | 5 | 2 | 3 | 4 | 4 | 3.88 |
| 7178 Al Alloy | 5 | 3 | 4 | 2 | 2 | 3 | 3 | 3.28 |
| HS Carbon fibers | 5 | 3 | 5 | 4 | 2 | 5 | 4 | 4.16 |
| HM Carbon fibers | 4 | 2 | 4 | 4 | 1 | 5 | 3 | 3.44 |

Table 2: Materials decision matrix

B.2 ΔV Preliminary Estimation

The ΔV needed to reach the target orbit has been initially estimated through Equation (4.1), where the single elements are reported in Equation (1).

$$\Delta V_{orbit} = \sqrt{\frac{g_0 R_0^2}{R_0 + z_{orbit}}} \quad \Delta V_{gravity} = \sqrt{2g_0 R_e \left(\frac{1}{r_0} - \frac{1}{r_f} \right)} \quad \Delta V_{launchsite} = v_{Earth} \cos(\lambda) \quad (1)$$

where λ is the latitude of the launch site which is 60° . The aircraft velocity is computed from the deployment Mach number defined in Section 3.4.

C MDO Appendix

C.1 Inputs

In Table 3, the general inputs for each configurations are presented.

| Category | Parameter | Value |
|----------------|-------------------------|---|
| General | Number of Stages | 2 |
| | Launch Altitude | 12,000 m |
| | Detachment Altitude | 80,000 m |
| | Orbit Altitude | 400,000 m |
| | Re-entry Altitude | 80,000 m |
| | Payload Mass | 250 kg |
| AeroTrajectory | Inclination | 98° |
| | Launch Velocity | 241.96 m/s |
| | Initial Pitch Angle | 28° |
| | Max. Pitch Rate | 3°/s |
| | Max. Pitch Acceleration | 1°/s ² |
| | Launch Latitude | 60° |
| Structure | Nose Type | Blunted |
| | Bluntness Ratio | 0.15 |
| Fairing | Tank Aspect Ratio | [2, 2] |
| | Tank Pressure | 4 Bar |
| Fairing | Empty Ratio | 0.12578 |
| | Max Payload Volume | 1.500045 m ³ |
| | Density | 125 kg/m ³ |
| | Safety Margins | 1.2 |
| Constants | g_0 | 9.80665 m/s ² |
| | R_{Earth} | 6,371,008.7714 m |
| | ω_{Earth} | 7.2921159e-5 rad/s |
| | μ_{Earth} | 3.986004418e14 m ³ /s ² |

Table 3: Constant Input Parameters for the LVD

In Table 4, the specific inputs of each configuration are reported.

| CONF | P_{c_1} [bar] | P_{c_2} [bar] | ρ_{ox_1} [kg/m ³] | ρ_{ox_2} [kg/m ³] | ρ_{fuel_1} [kg/m ³] | ρ_{fuel_2} [kg/m ³] |
|-------|--------------------|--------------------|---------------------------------------|---------------------------------------|---|---|
| ID 01 | 85 | 40 | 1140 | 1140 | 820 | 820 |
| ID 02 | 80 | 35 | 1140 | 1140 | 820 | 70.94 |
| ID 03 | 80 | 60 | 1140 | 1140 | 820 | 424 |
| ID 04 | 140 | 40 | 1140 | 1140 | 424 | 820 |
| ID 05 | 140 | 35 | 1140 | 1140 | 424 | 70.94 |
| ID 06 | 140 | 60 | 1140 | 1140 | 424 | 424 |
| ID 07 | 80 | 40 | 1140 | 1140 | 820 | 820 |
| ID 08 | 80 | 35 | 1140 | 1140 | 820 | 70.94 |
| ID 09 | 80 | 60 | 1140 | 1140 | 820 | 424 |
| ID 10 | 140 | 40 | 1140 | 1140 | 424 | 820 |
| ID 11 | 140 | 35 | 1140 | 1140 | 424 | 70.94 |
| ID 12 | 140 | 60 | 1140 | 1140 | 424 | 424 |

Table 4: Inputs for each configuration.

C.2 Configuration ID Bounds

In this section, all the bounds used for by GA Algorithm are presented.

| CONFIGURATION | | ID1 | | ID2 | | ID3 | | ID4 | |
|------------------------|-----------------|-------|-------|-------|-------|-------|-------|-------|-------|
| | | LB | UB | LB | UB | LB | UB | LB | UB |
| Propellant Mass | M_{p1} | 12800 | 19200 | 10400 | 15600 | 12000 | 18000 | 10400 | 15600 |
| | M_{p2} | 2000 | 3000 | 2000 | 3000 | 2000 | 3000 | 2400 | 3600 |
| Mixture Ratio | OF_1 | 2.21 | 2.99 | 2.21 | 2.99 | 2.21 | 2.99 | 3.06 | 4.14 |
| | OF_2 | 2.21 | 2.99 | 4.68 | 6.33 | 3.06 | 4.14 | 2.21 | 2.99 |
| Thrust-to-Weight Ratio | TW_1 | 1.04 | 1.56 | 0.96 | 1.44 | 0.88 | 1.32 | 1.04 | 1.56 |
| | TW_2 | 0.72 | 1.08 | 0.72 | 1.08 | 0.72 | 1.08 | 0.72 | 1.08 |
| Stage Diameter | D_1 | 1.2 | 1.8 | 1.2 | 1.8 | 1.2 | 1.8 | 1.2 | 1.8 |
| | D_2 | 1.04 | 1.56 | 1.04 | 1.56 | 1.04 | 1.56 | 1.04 | 1.56 |
| Release Altitude | z_1 | 12000 | 14000 | 12000 | 14000 | 12000 | 14000 | 12000 | 14000 |
| Expansion Ratio | ε_2 | 78 | 162 | 78 | 162 | 80 | 162 | 72 | 168 |

Table 5: Bounds for Configuration ID1, ID2, ID3, and ID4

| CONFIGURATION | | ID5 | | ID6 | | ID7 | | ID8 | |
|------------------------|-----------------|-------|-------|-------|-------|-------|-------|-------|-------|
| | | LB | UB | LB | UB | LB | UB | LB | UB |
| Propellant Mass | M_{p1} | 8800 | 13200 | 11200 | 16800 | 12800 | 19200 | 10400 | 15600 |
| | M_{p2} | 2000 | 3000 | 2400 | 3600 | 2000 | 3000 | 2800 | 4200 |
| Mixture Ratio | OF_1 | 3.06 | 4.14 | 3.06 | 4.14 | 2.21 | 2.99 | 2.21 | 2.99 |
| | OF_2 | 4.68 | 6.33 | 3.06 | 4.14 | 2.21 | 2.99 | 4.68 | 6.33 |
| Thrust-to-Weight Ratio | TW_1 | 0.96 | 1.44 | 1.04 | 1.56 | 1.04 | 1.56 | 0.96 | 1.44 |
| | TW_2 | 0.72 | 1.08 | 0.72 | 1.08 | 0.72 | 1.08 | 0.88 | 1.32 |
| Stage Diameter | D_1 | 1.2 | 1.8 | 1.2 | 1.8 | 1.2 | 1.8 | 1.2 | 1.8 |
| | D_2 | 1.04 | 1.56 | 1.04 | 1.56 | 1.04 | 1.56 | 1.04 | 1.56 |
| Release Altitude | z_1 | 12000 | 14000 | 12000 | 14000 | 12000 | 14000 | 12000 | 14000 |
| Expansion Ratio | ε_2 | 78 | 162 | 78 | 162 | 78 | 162 | 78 | 162 |

Table 6: Bounds for Configuration ID5, ID6, ID7, and ID8

| CONFIGURATION | | | ID9 | | ID10 | | ID11 | | ID12 | |
|------------------------|-----------------|-------|-------|-------|-------|-------|-------|-------|-------|----|
| Variables | | | LB | UB | LB | UB | LB | UB | LB | UB |
| Propellant Mass | M_{p1} | 12000 | 18000 | 10400 | 15600 | 8800 | 13200 | 11200 | 16800 | |
| | M_{p2} | 2000 | 3000 | 2400 | 3600 | 2000 | 3000 | 2400 | 3600 | |
| Mixture Ratio | OF_1 | 2.21 | 2.99 | 3.06 | 4.14 | 3.06 | 4.14 | 3.06 | 4.14 | |
| | OF_2 | 3.06 | 4.14 | 2.21 | 2.99 | 4.68 | 6.33 | 3.06 | 4.14 | |
| Thrust-to-Weight Ratio | TW_1 | 0.8 | 1.2 | 1.04 | 1.56 | 0.88 | 1.32 | 0.8 | 1.2 | |
| | TW_2 | 0.72 | 1.08 | 0.8 | 1.2 | 0.8 | 1.2 | 0.72 | 1.08 | |
| Stage Diameter | D_1 | 1.2 | 1.8 | 1.2 | 1.8 | 1.2 | 1.8 | 1.2 | 1.8 | |
| | D_2 | 1.04 | 1.56 | 1.04 | 1.56 | 1.04 | 1.56 | 1.04 | 1.56 | |
| Release Altitude | z_1 | 12000 | 14000 | 12000 | 14000 | 12000 | 14000 | 12000 | 14000 | |
| Expansion Ratio | ε_2 | 78 | 162 | 72 | 168 | 78 | 162 | 78 | 162 | |

Table 7: Bounds for Configuration ID9, ID10, ID11, and ID12

C.3 Results

| CONF | $OF_1[-]$ | $OF_2[-]$ | $TW_1[-]$ | $TW_2[-]$ | $M_{p1}[\text{kg}]$ | $M_{p2}[\text{kg}]$ | $z_1[\text{m}]$ | $\varepsilon_2[-]$ | $D_1[\text{m}]$ | $D_2[\text{m}]$ | GLOM[kg] |
|--------------|-----------|-----------|-----------|-----------|---------------------|---------------------|-----------------|--------------------|-----------------|-----------------|----------|
| ID 01 | 2.32 | 2.37 | 1.27 | 0.83 | 14079 | 2348 | 12717 | 137 | 1.56 | 1.25 | 18471 |
| ID 02 | 2.42 | 5.81 | 1.09 | 1.03 | 11185 | 2396 | 12598 | 98 | 1.44 | 1.22 | 15628 |
| ID 03 | 2.80 | 3.76 | 0.92 | 0.97 | 15002 | 2718 | 12168 | 155 | 1.39 | 1.28 | 19717 |
| ID 04 | 3.44 | 2.29 | 1.36 | 0.96 | 11987 | 3489 | 12531 | 78 | 1.47 | 1.23 | 17662 |
| ID 05 | 3.52 | 6.09 | 1.01 | 0.72 | 8922 | 2260 | 12273 | 121 | 1.39 | 1.16 | 13094 |
| ID 06 | 3.51 | 3.98 | 1.12 | 0.99 | 11933 | 3060 | 12177 | 81 | 1.40 | 1.16 | 17024 |
| ID 07 | 2.56 | 2.67 | 1.08 | 0.76 | 14470 | 2509 | 12132 | 123 | 1.49 | 1.19 | 19024 |
| ID 08 | 2.73 | 5.99 | 1.16 | 1.23 | 12357 | 3954 | 12948 | 82 | 1.56 | 1.29 | 18927 |
| ID 09 | 2.64 | 3.32 | 0.87 | 0.81 | 13468 | 2637 | 12465 | 151 | 1.36 | 1.24 | 18055 |
| ID 10 | 3.14 | 2.63 | 1.21 | 1.16 | 14836 | 2741 | 12323 | 89 | 1.52 | 1.25 | 19927 |
| ID 11 | 3.95 | 5.25 | 0.94 | 1.15 | 10928 | 2767 | 12650 | 115 | 1.25 | 1.25 | 15977 |
| ID 12 | 3.56 | 3.29 | 0.86 | 0.95 | 12690 | 2730 | 12698 | 84 | 1.41 | 1.20 | 17459 |

Table 8: Configurations Optimization Variables

C.4 Block Scheme Definition

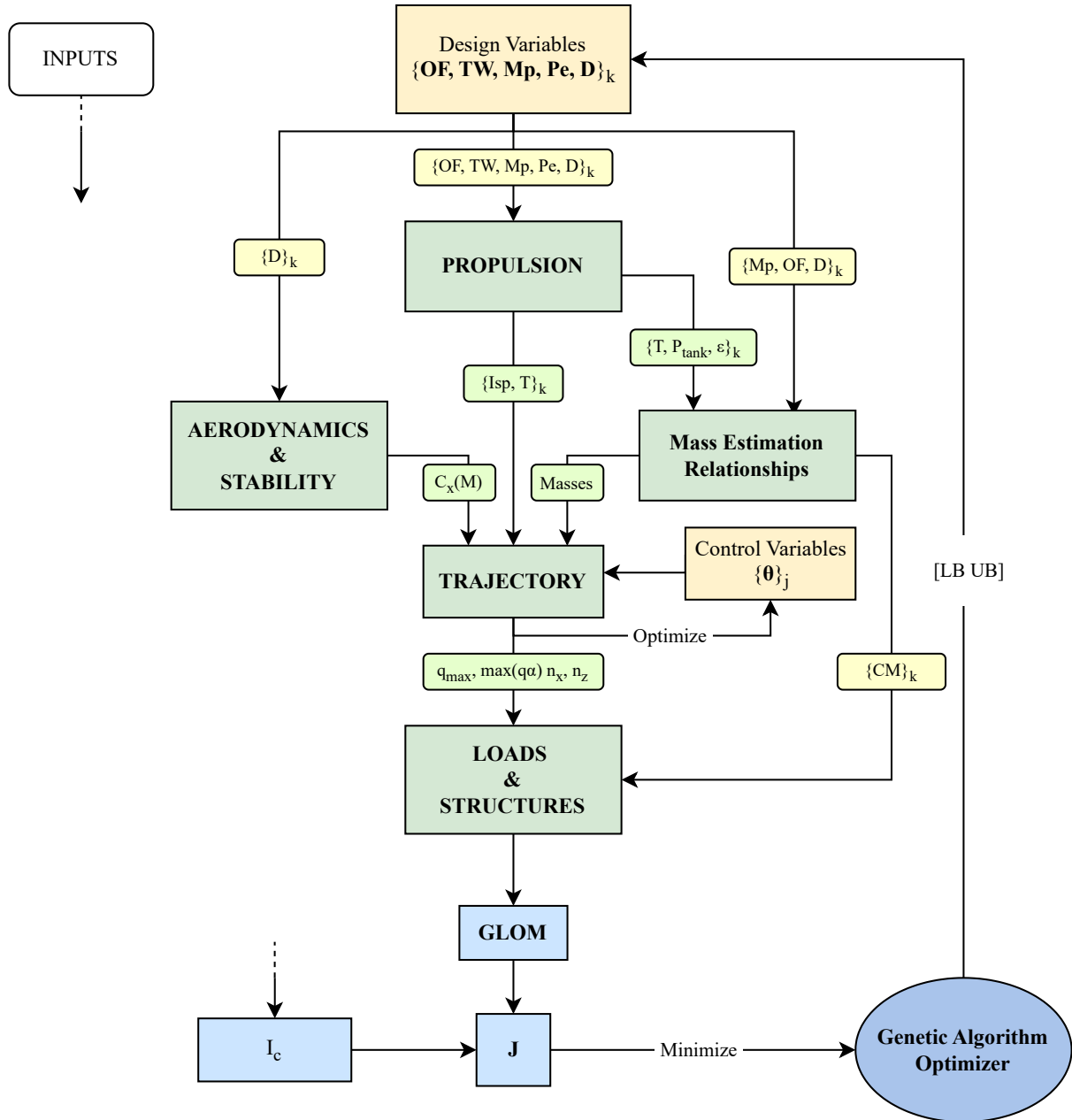
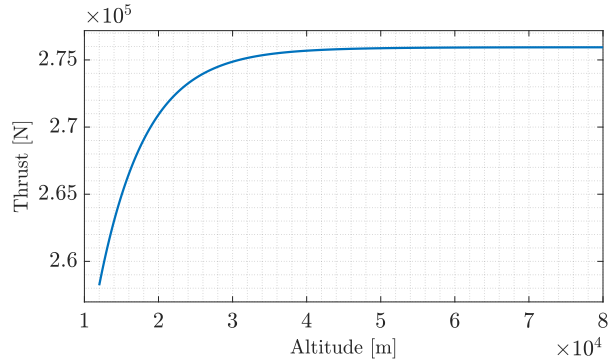
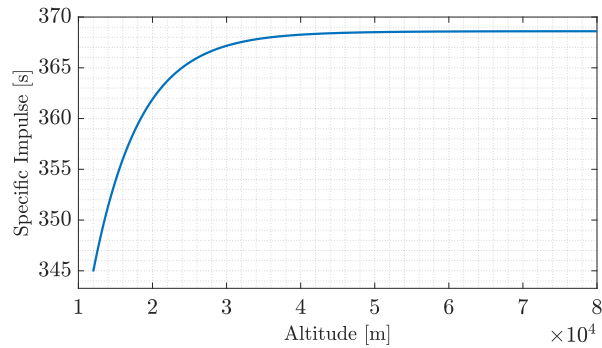


Figure 2: Block Scheme

D Propulsion System Appendix

In Figure 3 and Figure 4 are reported the evolution with the altitude of the thrust and the specific impulse of the first stage:

Figure 3: Thrust of 1st stage as function of altitudeFigure 4: Specific Impulse of 1st stage as function of altitude

Validation The validation of propulsion block has been performed considering the Merlin 1C engine used by Falcon 1 and Falcon 9 launch vehicles. Merlin 1C is a RP1-LOX pump-feed engine, which generates a thrust similar to the engine designed by the authors. In Table 17 are reported the engine specifications used as input for validation of propulsion block. In Table 18 are compared the I_{sp} and geometric shape calculated with the code implemented and the one retrieved from data-sheet.

| MERLIN 1C Specifications | |
|--------------------------|--------|
| P_c [bar] | 56.88 |
| $T(@s.l.)$ [kN] | 348.74 |
| O/F Ratio[–] | 5.5 |
| z_{opt} [km] | 1 |

Table 9: Merlin 1C Data^[3]^[4]

| | Real Data | Model Results |
|----------------------|-----------|---------------|
| ε | 14.5 | 13.89 |
| I_{sp} (@s.l.) [s] | 274 | 273.07 |
| I_{sp} (@vac) [s] | 304 | 306 |

Table 10: Validation of propulsion block

E Masses estimation Appendix

E.1 MER

Here is reported the whole development of the mass estimation procedure.

Tanks For the tanks, different MERs have been adopted based on the propellant inside (the analyzed one have been LOX, LH₂, RP-1, and LCH₄). The mass of each single propellant has been retrieved knowing both the total propellant mass M_{prop} and the corresponding O/F ratio for each stage. The MERs adopted are reported in Table 11, where all the four propellants considered in the MDO are present:

| Component | Original MER ^[53] | Corrected MER (AL) | Corrected MER (CF) |
|-----------------|------------------------------|--------------------------------|----------------------------------|
| $m_{tank,LOX}$ | $0.0107 m_{LOX} [kg]$ | $2 \times 0.0107 m_{LOX} [kg]$ | $1.8 \times 0.0107 m_{LOX} [kg]$ |
| $m_{tank,LH2}$ | $0.128 m_{LH2} [kg]$ | $2 \times 0.128 m_{LH2} [kg]$ | $1.8 \times 0.128 m_{LH2} [kg]$ |
| $m_{tank,RP1}$ | $0.0148 m_{RP1} [kg]$ | $2 \times 0.0148 m_{RP1} [kg]$ | $1.8 \times 0.0148 m_{RP1} [kg]$ |
| $m_{tank,LCH4}$ | $12.16 V_{LCH4} [kg]$ | $2 \times 12.16 V_{LCH4} [kg]$ | $1.8 \times 12.16 V_{LCH4} [kg]$ |

Table 11: MERs for tanks

To compute the volume of the tanks (Equation (2)), some additions were made to the volume of propellant, as stated in Section 4.4:

$$V_{tank} = V_{prop} (1 + \text{ullage} + \text{shrink}) = V_{prop} (1 + \text{ullage} + 3\alpha_{exp}\Delta T) \quad (2)$$

where the propellant volume has been computed from the propellant mass m_{prop} previously calculated and its density ρ_{prop} ($\rho_{LOX} = 1140 \text{ kg/m}^3$, $\rho_{LH2} = 71 \text{ kg/m}^3$, $\rho_{RP1} = 820 \text{ kg/m}^3$, $\rho_{LCH4} = 424 \text{ kg/m}^3$)^[53]. The ullage addition considered is +3%^[53], while for the shrinkage have been considered linear expansion coefficients α_{exp} both for the aluminum and for the carbon fiber tank, and ΔT specific for each cryogenic propellant as reported in Table 12:

| Tank material | α_{exp} | Propellant | ΔT | % shrinkage |
|---------------|--------------------------------------|------------|---------------|-------------|
| Aluminum | $2.34 \times 10^{-5} \text{ K}^{-1}$ | LOX | (293 – 90) K | +1.43% |
| Carbon fiber | $0.15 \times 10^{-5} \text{ K}^{-1}$ | LOX | (293 – 90) K | +0.09% |
| Aluminum | $2.34 \times 10^{-5} \text{ K}^{-1}$ | LH2 | (293 – 20) K | +1.92% |
| Carbon fiber | $0.15 \times 10^{-5} \text{ K}^{-1}$ | LH2 | (293 – 90) K | +0.12% |
| Aluminum | $2.34 \times 10^{-5} \text{ K}^{-1}$ | LCH4 | (293 – 111) K | +1.28% |
| Carbon fiber | $0.15 \times 10^{-5} \text{ K}^{-1}$ | LCH4 | (293 – 111) K | +0.08% |
| Aluminum | $2.34 \times 10^{-5} \text{ K}^{-1}$ | RP1 | 0 K | +0% |
| Carbon fiber | $0.15 \times 10^{-5} \text{ K}^{-1}$ | RP1 | 0 K | +0% |

Table 12: Shrinkage additions

To compute the dimensions of the tanks (i.e. height of the cylindrical part h_{cyl} , height of the domes h_{dome} , area of the tank A_{tank}), the formulas in the system of Equation (3) have been used:

$$\left\{ \begin{array}{l} h_{cyl,ox} = \frac{4V_{tank}}{\pi d^2} \quad (1 \text{ dome}) \\ h_{cyl,fuel} = \frac{4V_{tank}}{\pi d^2} - \frac{2d}{3(AR)} \quad (2 \text{ domes}) \\ h_{dome} = \frac{d/2}{(AR)} = \frac{R}{(AR)} \\ A_{tank} = 2\pi R h_{cyl} + 2\pi R^2 \left[1 + \frac{1}{2E(AR)^2} \ln \frac{1+E}{1-E} \right] \quad \text{where } E = \sqrt{1 - 1/(AR)^2} \quad (\text{eccentricity}) \end{array} \right. \quad (3)$$

From the area of the tank A_{tank} the insulation mass m_{ins} required by the cryogenic propellant has been calculated via the MERs^[53] shown in Table 13:

| Propellant | MER |
|------------|---|
| LOX | $m_{ins} = 1.123 [\text{kg/m}^2] \times A_{tank,LOX}$ |
| LH2 | $m_{ins} = 2.88 [\text{kg/m}^2] \times A_{tank,LH2}$ |
| LCH4 | $m_{ins} = 0.98 [\text{kg/m}^2] \times A_{tank,LCH4}$ |
| RP1 | $m_{ins} = 0 [\text{kg}]$ |

Table 13: Insulation mass for cryogenic propellants

Engine block For the estimation of the masses and dimensions related to the engine (“engine block”), the following MERs have been adopted. The thrust T considered is the one in optimal expansion condition.

- Thrust structure: mass = $2.55 \times 10^{-4} T [kg]$, length = $1/2 d_1$ (1st) and $1/3 d_2$ (2nd) [m]
- Liquid pump-fed engine: mass = $T (7.81 \times 10^{-4} + 3.37 \times 10^{-5} \sqrt{\varepsilon_{noz}}) + 59 [kg]$, length = point mass
- TVC gimbals: mass = $237.8 \left(\frac{T}{P_c}\right)^{0.9375} [kg]$, length = point mass

Interstages, skirts, wiring, avionics To size these components, the following MERs have been considered:

- Aft skirts: mass = $13.3 [kg/m^2] A_{skirt}$, length = d_1 (1st) and $1/3 d_2 + h_{dome,2}$ (2nd) [m]
- Interstage: mass = $13.3 [kg/m^2] A_{interstage}$, length = d_1 (1st) and d_2 (2nd) [m]
- Wirings: mass = $1.43 [kg/m] (l_{stage} + l_{interstage})$, length = $l_{stage} + l_{interstage} [m]$ but then considered as a point mass
- Avionics: mass = $75 kg$ divided 80% in the upper stage and 20% in the lower stage, length = point mass

Fairing To estimate the mass of the fairing, some geometric considerations are needed and are reported in the system of Equation (4):

$$\begin{cases} d_f = 1.05d_2 & (\text{fairing diameter}) \\ l_f = l_{f,cyl} + l_{f,nose} = 1.55d_f + 0.8d_f = 2.35d_f & (\text{fairing length}) \\ R_f = \frac{d_f}{2} & (\text{fairing radius}) \\ R_{nose} = (BR) R_f & (\text{fairing nose radius}) \\ ap = \sqrt{((l_{f,nose} - R_{nose})^2 + (R_f - R_{nose})^2)} & (\text{apothem}) \\ A_f = \pi(R_f + R_{nose})ap + 2\pi R_{nose}^2 + 2\pi R_f l_{f,cyl} & (\text{fairing surface}) \end{cases} \quad (4)$$

where BR is the bluntness ratio of the nose. The mass of the fairing^[53] has been estimated as:

$$m_f = 9.89 [kg/m^2] \times A_f \quad (5)$$

but has been refined as explained before.

Inside the fairing, the Payload Attach Fitting (PAF) mass has been estimated as via Equation (6)^[53]:

$$m_{PAF} = 0.0755 m_{pay} + 50 [kg] \quad (6)$$

Recovery The recovery block has been estimated in a preliminary way as:

$$\begin{cases} m_{recovery} = 1.3 \times 0.3 \times (\text{mass to recover}), & \text{where:} \\ \text{mass to recover (1}^{\text{st}} \text{ stage)} = m_{engine,1} \\ \text{mass to recover (2}^{\text{nd}} \text{ stage)} = m_{inert,2} + m_{interstage,2} \end{cases} \quad (7)$$

Dimensions A visual rendering of the launcher can be seen in Figure 5, which is not on scale and should be considered representative only of the model adopted, not of the actual final configuration.

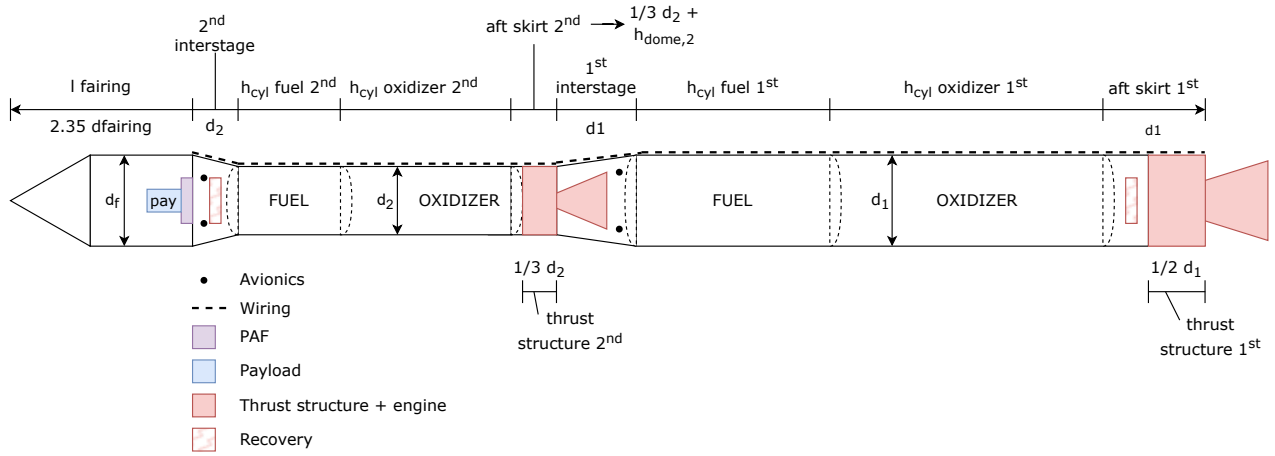


Figure 5: Preliminary dimensions

Validation To validate the results obtained from the estimations (both masses and lengths), a search for a compatible launcher has been done. The difficulties encountered in this part are mainly related to two aspects: first, airborne launchers can be considered a niche, and their user manuals do not provide enough information to run our code without a huge amount of assumptions; second, the totality of user manuals found that provide enough information are those of classic ground-launched rockets. Our choice was to validate our results (codes and corrective factors) with SpaceX's Falcon 1^[80], that has a user manual with almost all the information needed to reduce the amount of assumptions. Our developed code has been run with Falcon 1's data, and the following errors have been found on the dry mass and on the total length:

- Dry mass, first stage: -4.2% error
- Dry mass, second stage: -11.6% error
- Total length: -4.4% error

We concluded that the estimation process provides realistic results.

E.2 Centres of mass

To compute the local centres of mass of each component of the launcher, the following models have been adopted:

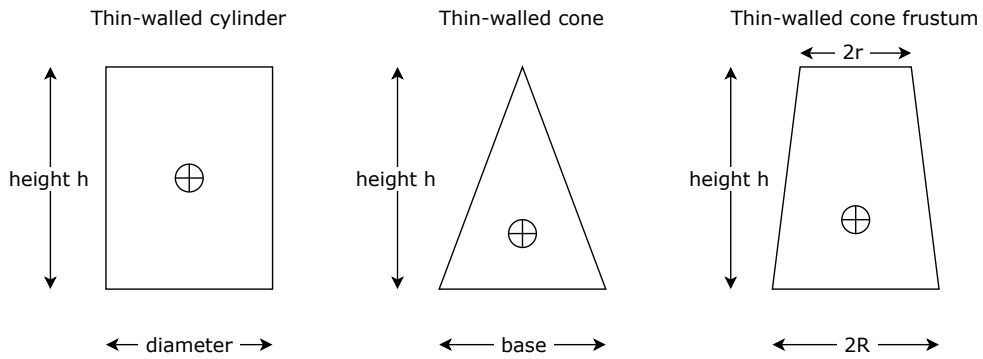


Figure 6: Shapes for local CM position calculations

where (referring to Figure 6):

$$\begin{cases} \text{Cylinder: } h_{CM} = \frac{1}{2}h \text{ above base} \\ \text{Cone: } h_{CM} = \frac{1}{3}h \text{ above base} \\ \text{Cone frustum: } h_{CM} = \frac{h}{3} \left(\frac{2r+R}{r+R} \right) \text{ from major base} \end{cases} \quad (8)$$

The fairing has been considered, in a first approximation, as a cone; this assumption is not completely true (it is a blunted nose), but has been formulated like this for simplicity and to not divide it into subsections.

| Component | Local h_{CM} model |
|-----------------------------|--|
| Fairing | Cone |
| PAF | Point, @ CM fairing |
| Payload | Point, @ CM fairing |
| Interstage | Cone frustum |
| Tank + Insulation | Cylinder |
| Aft skirt | Cylinder |
| Thrust structure | Cylinder |
| Engine + TVC | Point, $1/8 h_{thr\ str}$ above base |
| Recovery (1 st) | Point, @ Aft skirt (1 st) |
| Recovery (2 nd) | Point, @ Interstage (2 nd) |
| Avionics (1 st) | Point, $1/3 d_1$ above 1 st interstage major base |
| Avionics (2 nd) | Point, $2/3 d_2$ above 2 nd interstage major base |
| Wiring | Point, $1/2 l_{stage}$ |

Table 14: Local CM for components

while the propellant's CM shifts from the centre of the tank to the end as it is consumed.

F Aerodynamics Appendix

F.1 C_N computation:

C_N is computed as follows:

$$C_N = \frac{\sin(2\alpha) \cdot \cos(\frac{\alpha}{2})}{S_{ref}} \cdot \int_0^l \left(\frac{C_N}{C_{N0}} \right)_{SB} \cdot \frac{dA}{dx} dx + \frac{2\eta \cdot C_{dn}}{S_{ref}} \sin^2(\alpha) \int_0^l \left(\frac{C_N}{C_{N0}} \right)_{Newt} r dx \quad (9)$$

In the preliminary analysis, only the body's circular section was considered, so both $\left(\frac{C_N}{C_{N0}} \right)_{SB}$ and $\left(\frac{C_N}{C_{N0}} \right)_{Newt}$ are equal to 1.

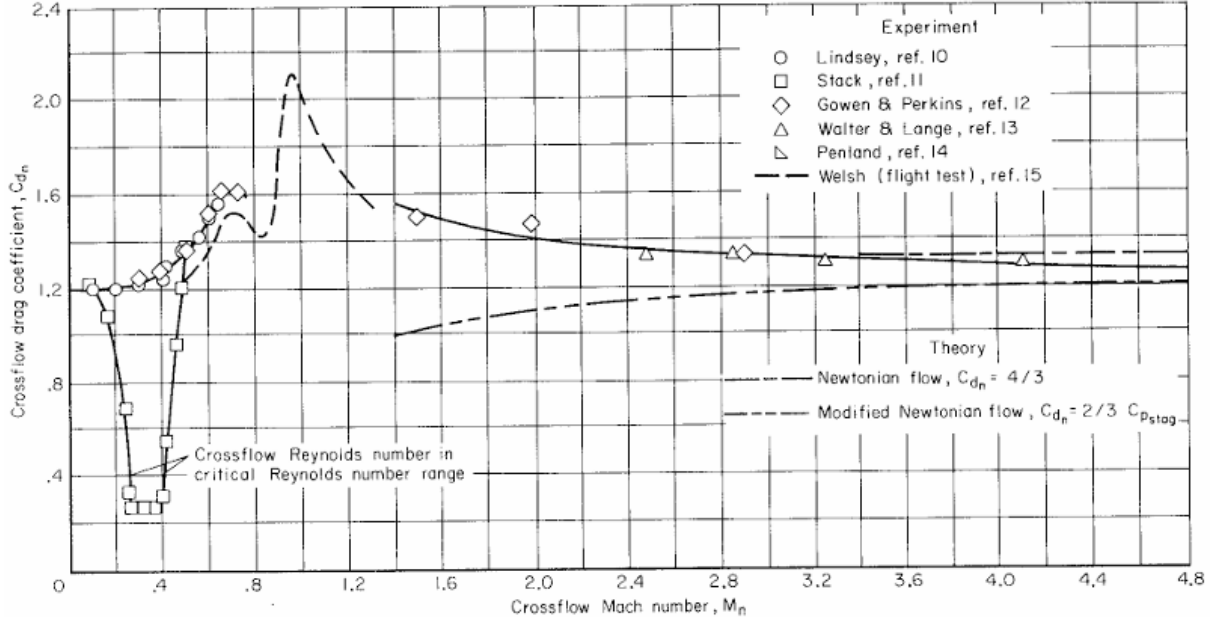


Figure 7: Crossflow drag coefficient as a function of crossflow Mach number

The crossflow drag coefficient C_{dn} for a circular cylinder section is obtained as follows:

- For $M_n \leq 4.5$, C_{dn} is determined experimentally as a function of the crossflow Mach number M_n (Figure 7).
- For $M_n \geq 5.5$, the asymptotic value is $C_{dn} = \frac{2}{3}C_{Pstag}$, with $C_{Pstag} \approx 1.8$ derived from the perfect gas relation.
- For $4.5 < M_n < 5.5$, C_{dn} is linearly interpolated from the experimental value at $M_n = 4.5$ to the asymptotic value at $M_n = 5.5$.

The crossflow drag proportionality factor η is given by:

$$\text{For } M \leq 1, \eta = 0.05 \frac{l}{d} + 0.52 \quad , \quad \text{For } M > 1, \eta = 1$$

F.2 C_A computation:

C_A is computed as follows:

- $C_{A0} = C_{Aw} + C_{Af} + C_{Ab}$
- C_{Aw} , the wave drag contribution, depends on the nose shape. The following cases were considered:
 - For $M \leq 1$ (all shapes, Fleeman^[55]): $C_{Aw} = 0.8 \sin^2(\phi)$

- For $M > 1$, conical nose:

$$C_{Aw} = \left(1.586 + \frac{1.834}{M^2} \right) \left(\tan^{-1} \left(\frac{0.5}{f_n} \right) \right)^{1.69} \quad (10)$$

- For $M > 1$, tangent ogive (Miles method):

$$C_{Aw} = P \left(1 - \frac{196 f_n^2 - 16}{14(M + 18)f_n^2} \right) \quad (11)$$

where

$$P = \left(0.083 + \frac{0.096}{M^2} \right) \left(\frac{\sigma}{10} \right)^{1.69} \quad (12)$$

and

$$\sigma = 2 \tan^{-1} \left(\frac{0.5}{f_n} \right) \left(\frac{180}{\pi} \right) \quad (13)$$

- For $M > 1$, blunt nose (Fleeman):

$$C_{Aw} = C_{Aw,\text{sharpnose}} \frac{(S_{\text{ref}} - S_{\text{nose tip}})}{S_{\text{ref}}} + C_{Aw,\text{Hemi}} \frac{S_{\text{nose tip}}}{S_{\text{ref}}} \quad (14)$$

where

$$C_{Aw,\text{Hemi}} = 0.665 \left(1.59 + \frac{1.83}{M^2} \right) \quad (15)$$

and

$$C_{Aw,\text{sharpnose}} = \left(1.59 + \frac{1.83}{M^2} \right) \left(\tan^{-1} \left(\frac{0.5}{f_n} \right) \right)^{1.69} \quad (16)$$

Furthermore a correction coefficient is computed for $1.2 < M < 1.8$ to mitigate the transonic overshoot observed in the C_{Aw} values (Figure: 12, experimental data from NACA report^[81]).

- C_{Af} , skin friction coefficient:

$$C_{Af} = 0.053 \left(\frac{l}{d} \right) \left(\frac{M}{ql} \right)^{0.2} \quad (17)$$

- C_{Ab} , base pressure coefficient:

- $M \geq 1$

$$C_{Ab} = \frac{0.25}{M} \quad (18)$$

- $M < 1$

$$C_{Ab} = 0.12 + 0.13M^2 \quad (19)$$

- if the engine is on:

$$C_{Ab} = C_{Ab} \left(1 - \frac{A_{e,\text{nozzle}}}{S_{ref}} \right) \quad (20)$$

- The total axial coefficient is given by:

$$C_A = C_{A0} + m \cdot \alpha \quad (21)$$

where the coefficient m is obtained from experimental data and depends on the nose shape.

F.3 Validation of the body alone geometry aerodynamics

The estimation algorithm is validated by comparing the results with experimental data from NASA^[56], for Mach numbers ranging from 1.50 to 2.86 and angle of attacks $0^\circ \leq \alpha \leq 60^\circ$. with conical and tangent ogive noses. For both configurations, the relative error is always less than 30% for $0^\circ < \alpha < 45^\circ$, improving at higher Mach numbers (more common in our trajectory), mostly below 15% (Validation graphs: F.3). Additionally, the blunted nose type will undergo further validation. This process yields correction coefficients designed to mitigate the transonic overshoot observed in the C_{Aw} values.

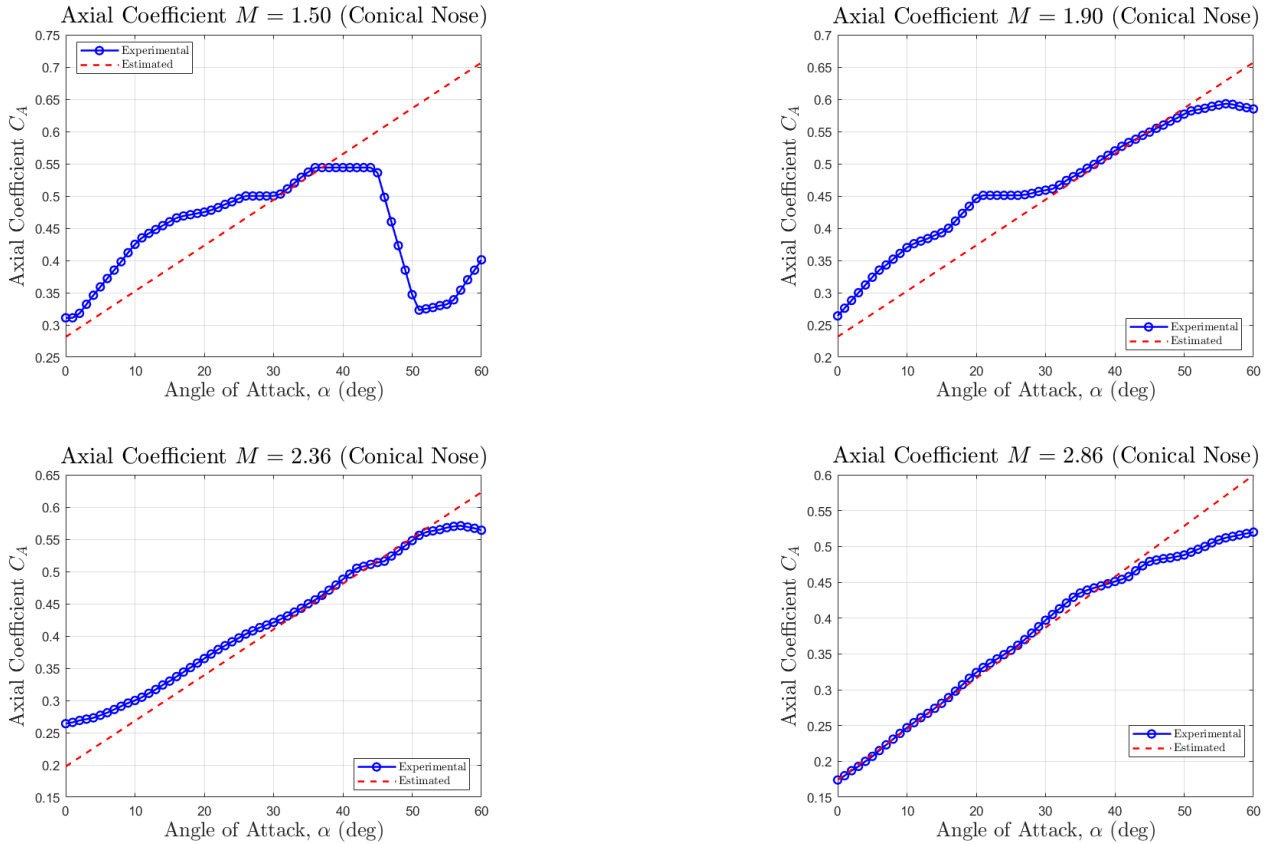
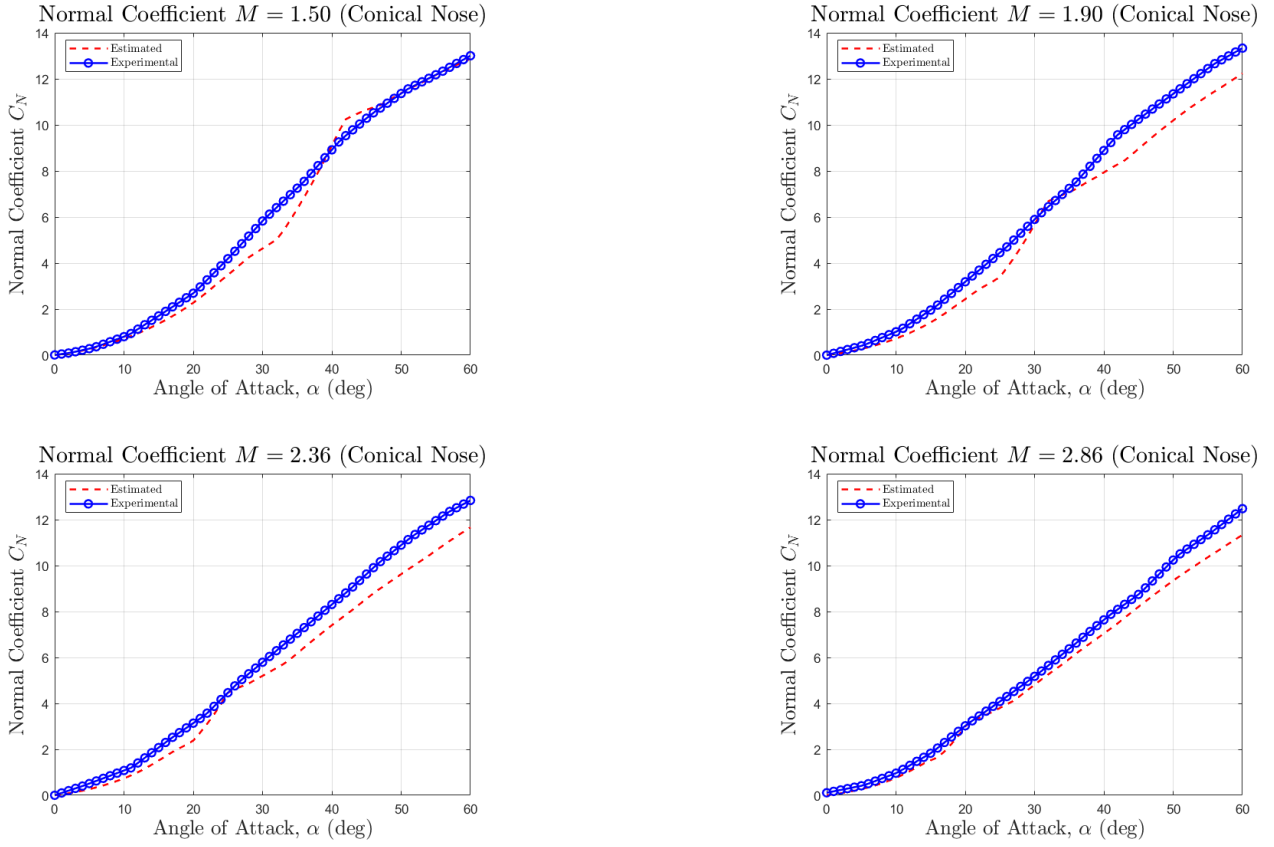
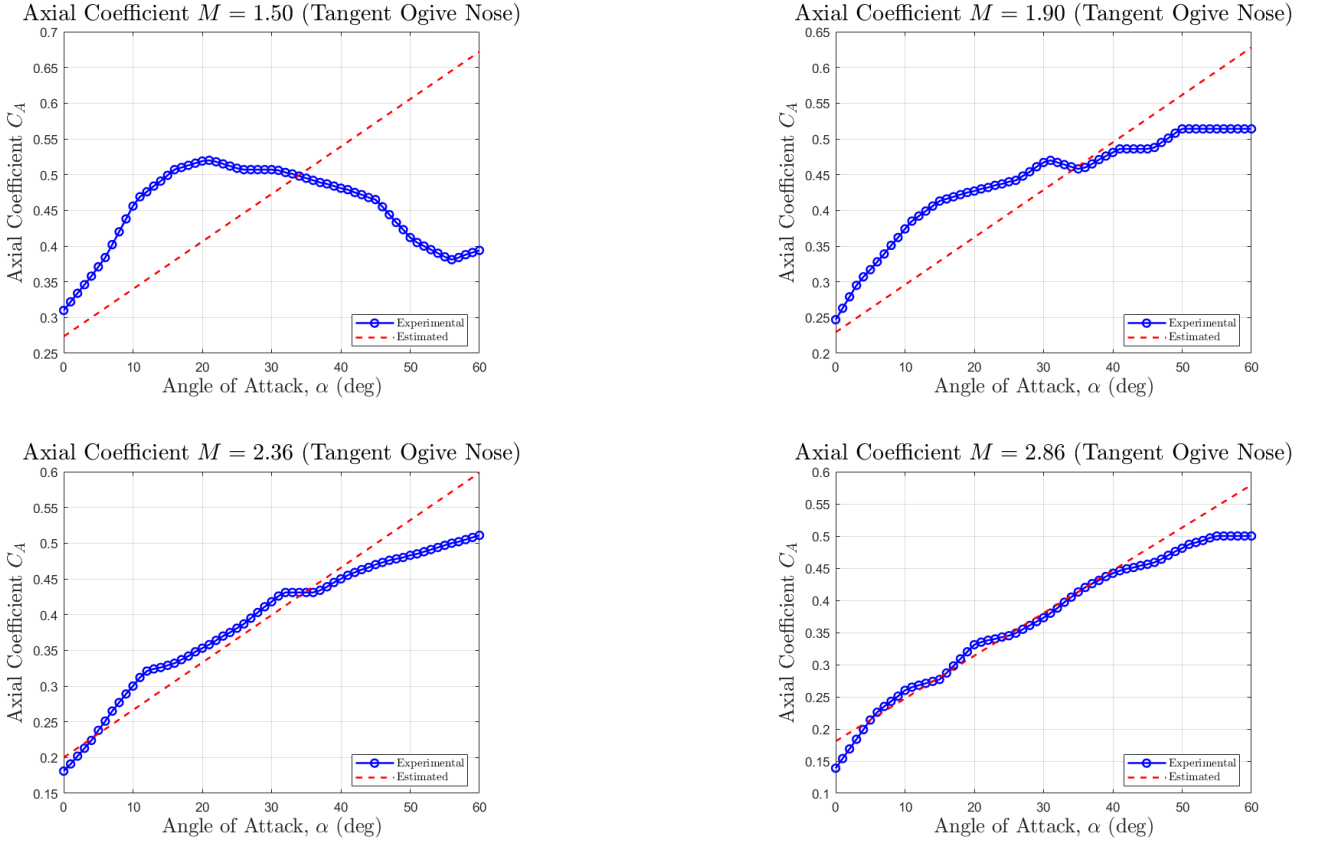
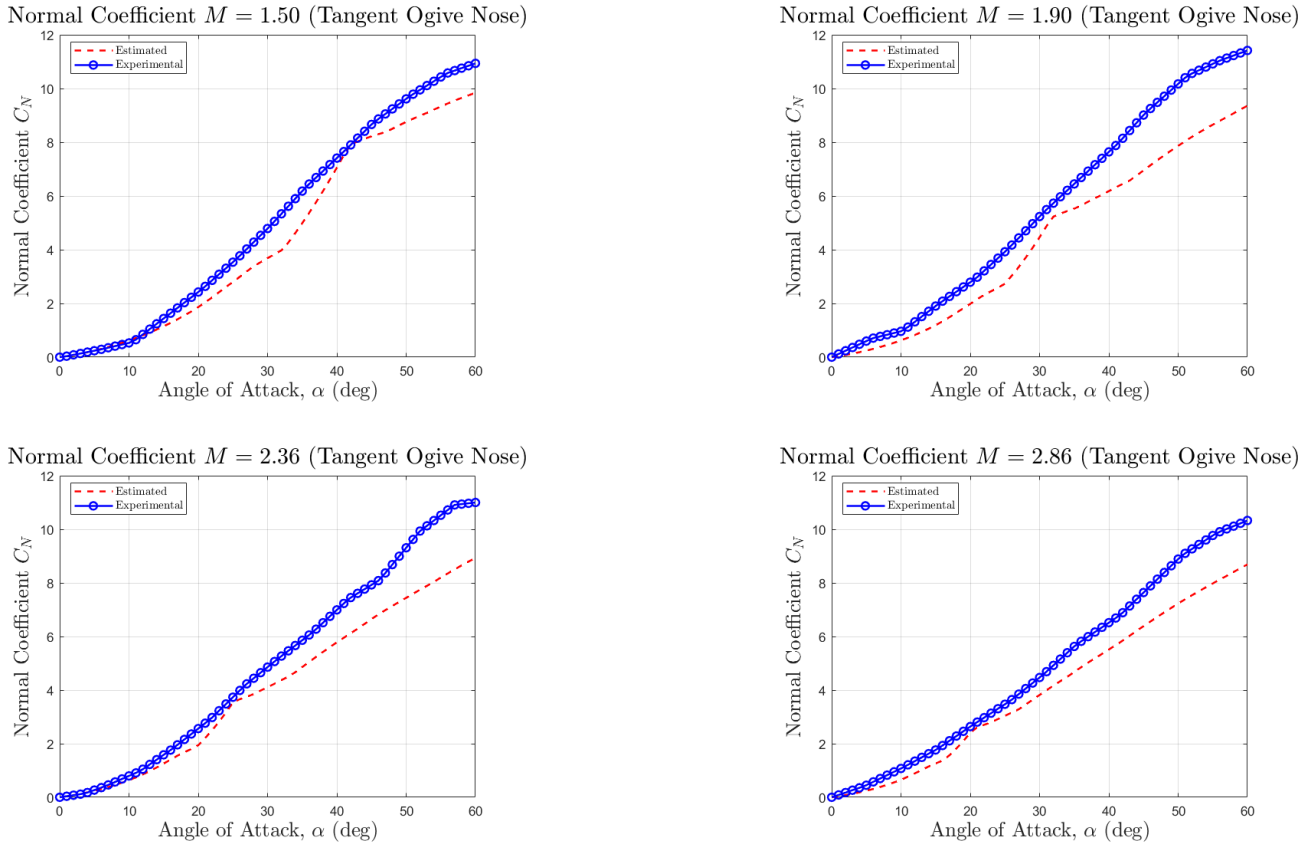
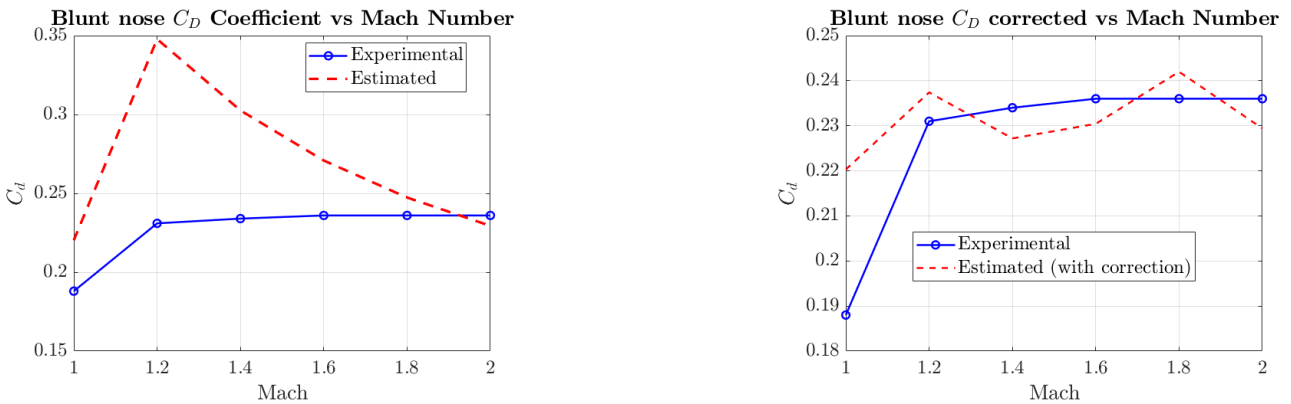


Figure 8: C_A body for Conical nose with $l_N/d = 3$ and $l_A/d = 8$

Figure 9: C_N body for Conical nose with $l_N/d = 3$ and $l_A/d = 8$ Figure 10: C_A body for Tangent ogive nose with $l_N/d = 3$ and $l_A/d = 6$

Figure 11: C_N body for Tangent ogive nose with $l_N/d = 3$ and $l_A/d = 6$ Figure 12: C_D body and correction for blunt nose with $l/d = 8.91$

The validation of the estimated C_L and C_D coefficients for body-wing-tail is performed on experimental data from Pegasus Air-Launched Booster^[58].

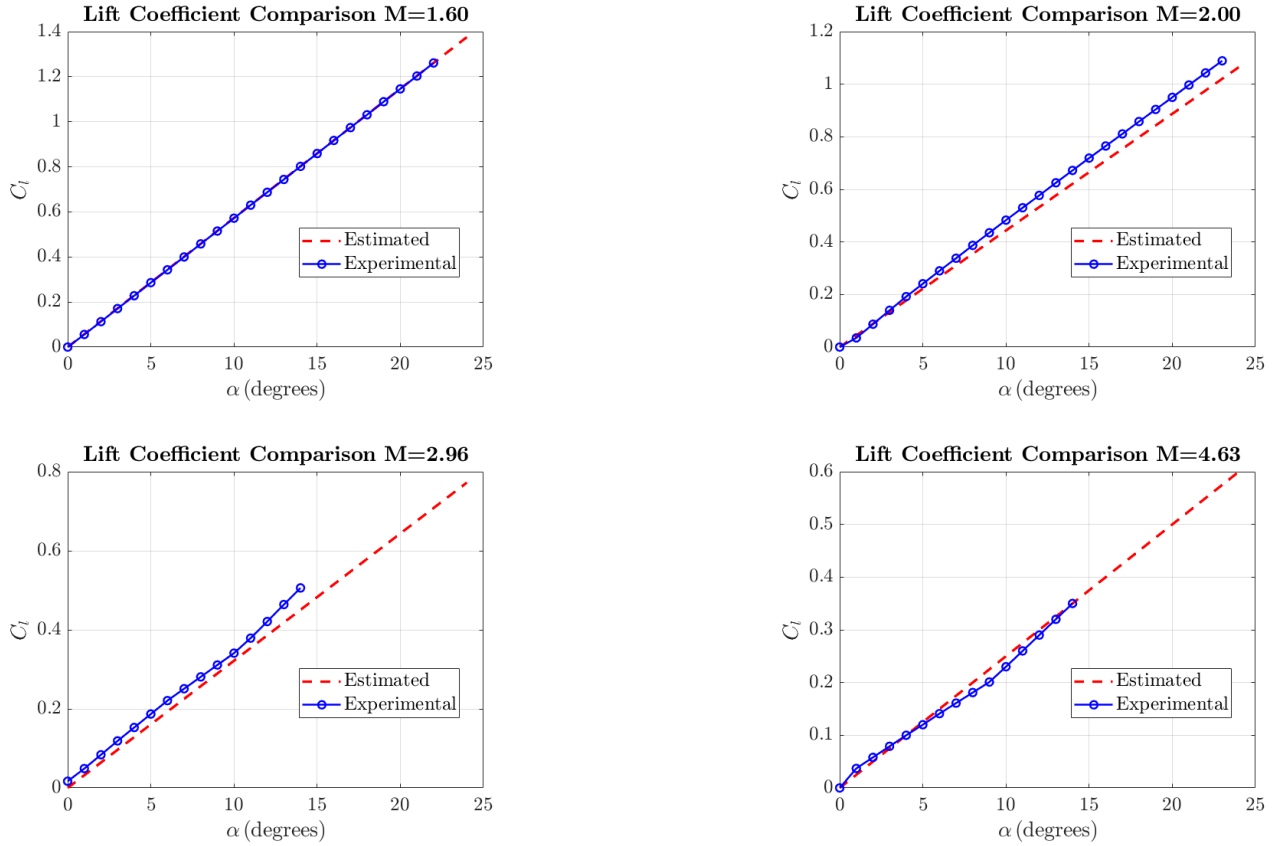
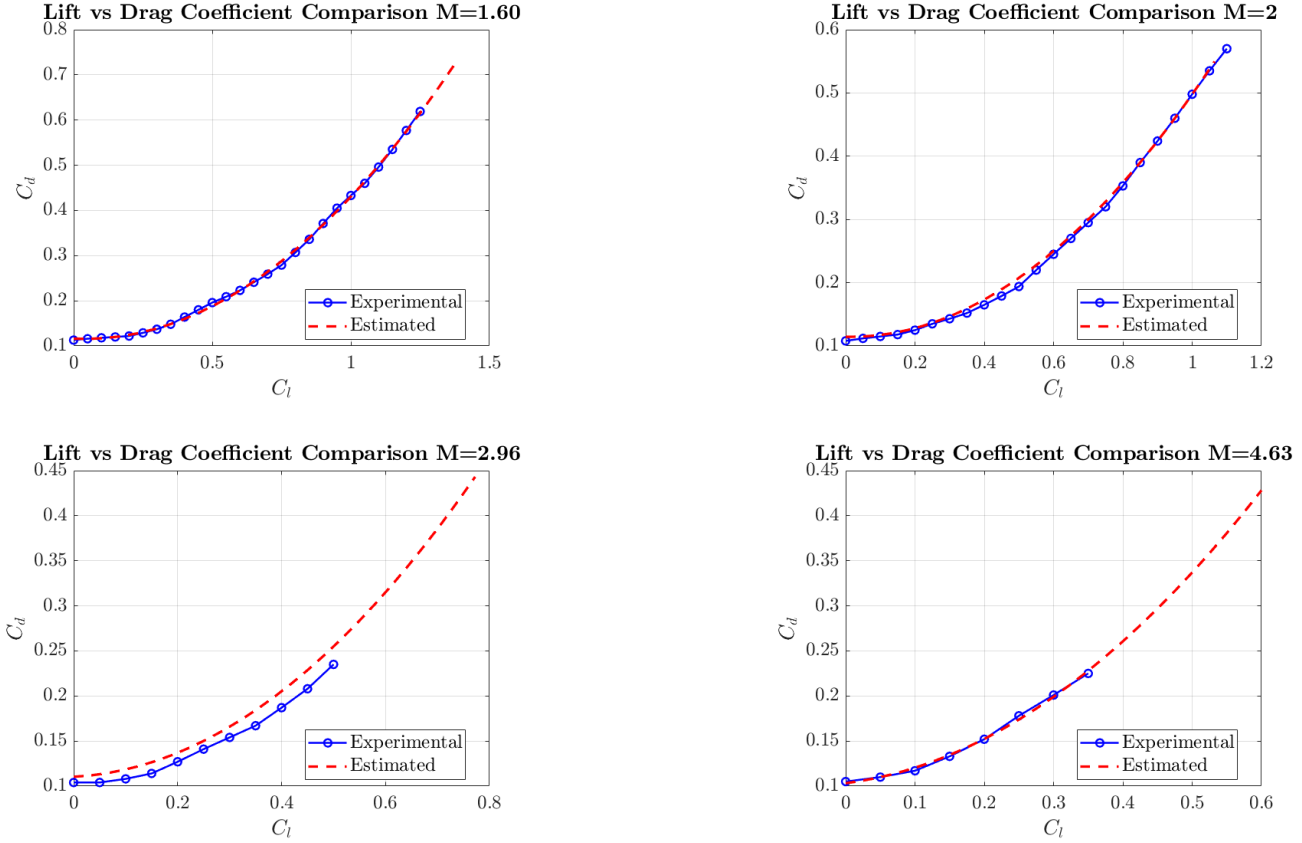


Figure 13: C_L for the Pegasus launcher body-wing-tail

Figure 14: C_D vs C_L for the Pegasus launcher body-wing-tail

F.4 Body wing tail NKP method

To evaluate the body-wing-tail configuration NKP method was used^[82], accounting for the aerodynamic interference of the surfaces. The lift coefficient is obtained as:

$$C_{LNKP} = C_{LN} + C_{LWB} + C_{LBW} + C_{LTB} + C_{LBT} \quad (22)$$

The components are obtained as following:

- Nose lift coefficient: $C_{LN} = K_N \cdot C_{L\alpha w} \alpha$
- Wing lift coefficient (considering the presence of the body): $C_{LWB} = (K_{WB} \alpha + k_{WB} \delta_w) C_{L\alpha w} \alpha$
- Body lift coefficient (due to the presence of the wing): $C_{LBW} = (K_{BW} \alpha + k_{BW} \delta_w) C_{L\alpha w} \alpha$
- Tail lift coefficient (considering the presence of the body): $C_{LTB} = (K_{TB} \alpha + k_{TB} \delta_t) C_{L\alpha t} \alpha$
- Body lift coefficient (due to the presence of the tail): $C_{LWT} = (K_{WB} \alpha + k_{WB} \delta_t) C_{L\alpha t} \alpha$

The K coefficients are calculated according to NKP method^[82]. The lift contribution due to wing vortices is neglected for preliminary analysis. Furthermore $C_{L\alpha}$ is obtained from the linearized thin airfoil theory (2D), using the Prandtl-Glauert transformation^[57]:

- $M < 0.8$

$$C_{L\alpha} = \frac{2\pi}{\sqrt{1 - M^2}} \quad (23)$$

- $M > 1.3$

$$C_{L\alpha} = \frac{4}{\sqrt{M^2 - 1}} \quad (24)$$

- $0.8 \leq M \leq 1.3$: Linear interpolation from $C_{L\alpha}$ at $M = 0.8$ and $C_{L\alpha}$ at $M = 1.3$

G Stability Appendix

In Figure 15 the data used for the validation of the fins are presented. Also the relations used to evaluate the position of the center of pressure of the fins and the semi-span of the wings are showed.

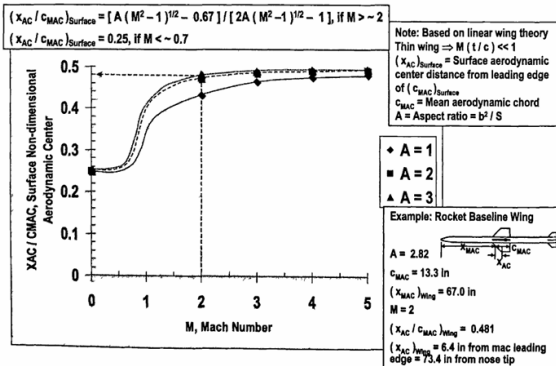


Figure 15: Stability Baseline

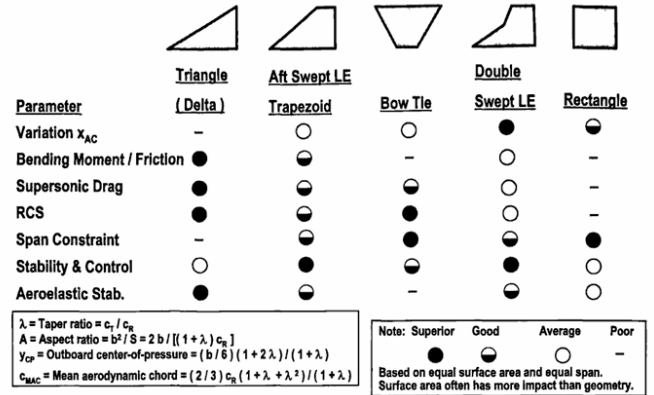


Figure 16: Example of tail geometry alternatives

H Trajectory Appendix

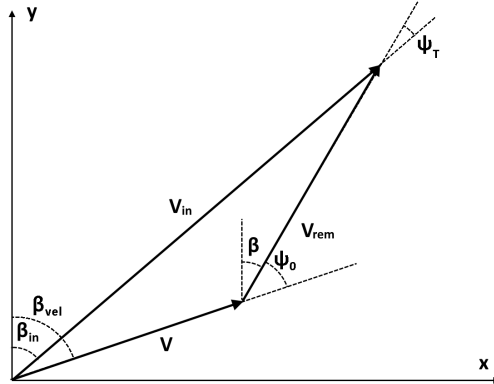


Figure 17: Vectors and angles for the azimuth

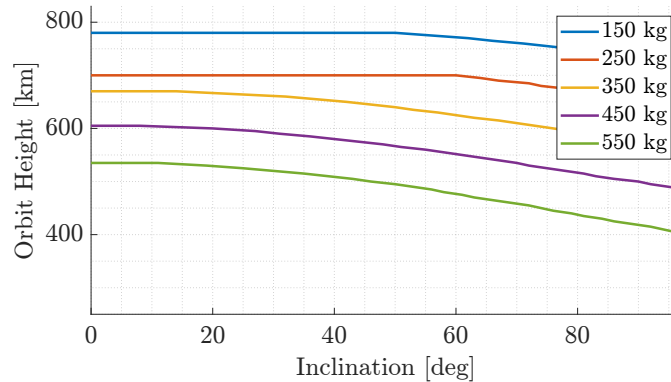


Figure 18: Possible orbits with no reusability

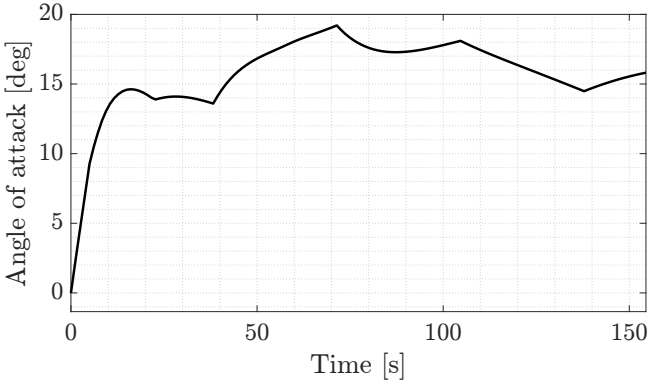


Figure 19: First stage trajectory angle of attack

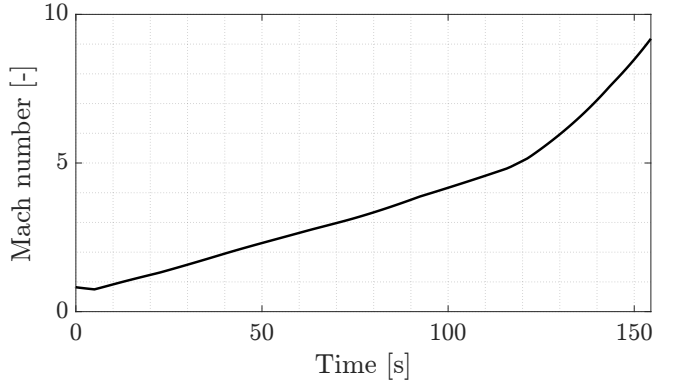


Figure 20: First stage Mach number

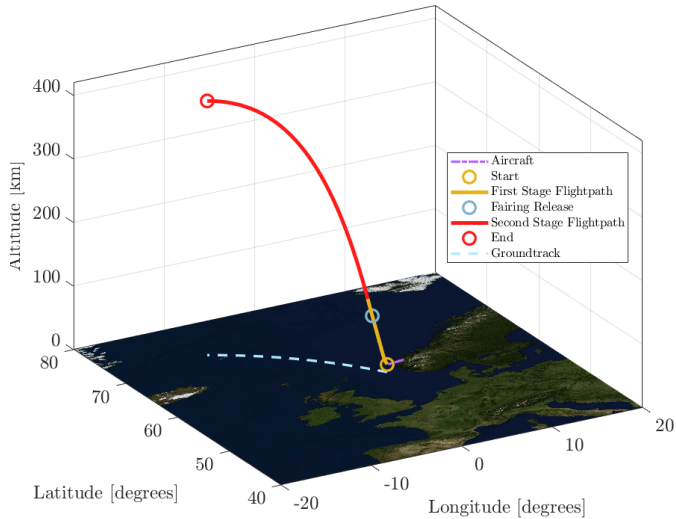


Figure 21: Launcher Ground Track

H.1 Power Explicit Guidance

To guarantee a high orbit insertion accuracy the second stage trajectory follows a closed loop PEG algorithm. The pitch angle formula depends on the parameters A, B and C with the following formula:

$$\theta(t) = \sin^{-1}(A + B \cdot t + C(r)) \quad C(r) = \frac{\frac{\mu}{r^2} - \omega^2 r}{a} \quad (25)$$

Although one could calculate this parameters at the initial time step and follow the trajectory all the way to cutoff, the reached orbit would not be exactly the same as the target as the PEG algorithm uses linear approximations, it doesn't take into account any perturbations and assumes a flat earth. As such the A and B parameters are constantly recalculated to maximize orbit insertion accuracy.

The PEG algorithm is used to calculate A, B and T. With T being the remaining burn time.

Rocket equations

The rocket equations can be used to calculate the acceleration of the rocket as a function of time.

$$\tau a = \frac{v_e}{a} \quad a(t) = \frac{a_0}{1 - \frac{t}{\tau}} \quad (26)$$

With a_0 being the current acceleration. The parameter τ is useful for many equations, it represents the time it would take to burn the rocket completely if it was all propellant.

Integrals

Some necessary integrals are necessary, they will be useful to represent what fraction of the rockets ΔV and traveled distance will go in the vertical and horizontal directions. In [83] a recursive formula for this integrals is presented.

$$b_0 = \int_0^T a(t) dt = -v_e \ln \left(1 - \frac{T}{\tau} \right) \quad b_n = \int_0^T t^n a(t) dt = b_{n-1} \tau - \frac{v_e T^n}{n} \quad (27)$$

$$c_0 = \int_0^T \int_0^t a(s) ds dt = b_0 T - b_1 \quad c_n = \int_0^T \int_0^t s^n a(s) ds dt = c_{n-1} \tau - \frac{v_e T^{n+1}}{n(n+1)} \quad (28)$$

Main Loop

The main loop is constantly run during the flight of the second stage to update the parameters required for the trajectory. When the PEG is run for the first time the loop must be run many times until the remaining burn time has converged, after that it only needs to be updated periodically.

The loop requires the estimated remaining burn time as an input. If it's the first time running it can be estimated as the total burn time of the second stage.

Otherwise it can be calculated as: $T_{n+1} = T_n - \Delta T$.

Then the integrals b_0 , b_1 , b_2 , c_0 and c_1 are calculated. The parameters A and B can be calculated by solving:

$$\begin{bmatrix} b_0 & b_1 \\ c_0 & c_1 \end{bmatrix} \begin{bmatrix} A \\ B \end{bmatrix} = \begin{bmatrix} \dot{r}_T - \dot{r} \\ r_T - r - \dot{r}T \end{bmatrix} \quad (29)$$

The sine of the pitch angle at the current time and burnout, and its estimated derivative are:

$$f_{r,0} = A + C_0 \quad f_{r,T} = A + BT + C_T \quad \dot{f}_r = \frac{f_{r,T} - f_{r,0}}{T} \quad (30)$$

With C being the portion of the rocket's acceleration used to counteract the gravity and centrifugal force.

$$C_0 = \frac{\frac{\mu}{r_0^2} - \omega_0^2 r_0}{a_0} \quad C_T = \frac{\frac{\mu}{r_T^2} - \omega_T^2 r_T}{a_T} \quad (31)$$

The yaw angle can be estimated with equation 4.22 and then the sine of the yaw angle and its derivative can be calculated as:

$$f_{h,0} = \sin(\psi_0) \quad f_{h,T} = \sin(\psi_T) \quad \dot{f}_h = \frac{f_{h,T} - f_{h,0}}{T} \quad (32)$$

Then the cosine of the pitch, pitch rate and pitch acceleration can be estimated as:

$$f_\theta = 1 - \frac{f_{r,0}^2}{2} - \frac{f_{h,0}^2}{2} \quad \dot{f}_\theta = - (f_{r,0} \dot{f}_r + f_{h,0} \dot{f}_h) \quad \ddot{f}_\theta = - \frac{\dot{f}_{r,0}^2 + \dot{f}_{h,0}^2}{2} \quad (33)$$

Finally the required change in angular momentum can be estimated as:

$$\Delta h = h_T - h_0 = \bar{r}(f_\theta b_0 + \dot{f}_\theta b_1 + \ddot{f}_\theta b_2) \quad (34)$$

With:

$$\bar{r} = \frac{r_T + r_0}{2} \quad h_T = \omega_T r_T^2 \quad h_0 = \omega_0 r_0^2 \quad (35)$$

Knowing that $b_0 = \Delta V$, ΔV and the remaining burn time can be solved from equation 34.

$$\Delta V = \frac{\frac{h_T - h_0}{\bar{r}} - \dot{f}_\theta b_1 - \ddot{f}_\theta b_2}{f_\theta} \quad T = \tau \left(1 - e^{-\frac{\Delta V}{v_e}} \right) \quad (36)$$

Cutoff Logic

As T gets smaller the algorithm can become unstable as a solution to perfectly reach the target is not found. As such when T is 5 seconds the algorithm is stopped and A and B are kept. Burning with a pitch equal to $\sin^{-1}(A + Bt + C(r))$ with $t \in [0, T]$ until engine cutoff at $t = T$. For simplicity it is assumed that engine cutoff is instant, however in reality it is necessary to take into account the time required for engine shutoff and to begin the shutoff procedure at the right time.

I Structures System Appendix

I.1 Thickness Sizing Procedure

For every component (pressurized and unpressurized), the needed σ_{tot} to resist the axial force stress σ_A and bending moment stress σ_B has been computed via Equation (37), with a conservative approach:

$$\sigma_A = -\frac{P}{A}(SF) = -\frac{P}{2\pi R t}(SF) \quad \sigma_B = \frac{MR}{I}(SF) = \frac{F_{lat} h_{CM} R}{\pi R^3 t}(SF) \quad \sigma_{tot} = |\sigma_A| + |\sigma_B| \quad (37)$$

Also, the shear force stress has been analyzed via Equation (38):

$$\tau_{shear} = \frac{F_{lat}}{A}(SF) \quad \text{with} \quad \tau_{shear,allow} = \frac{1}{2}\sigma_{allow} \quad (38)$$

Furthermore, since the structural elements of the launcher are thin-walled shells, buckling has been considered a valuable aspect to analyze; the correlations used are reported by Sforza^[84]:

$$\frac{\sigma_{crit}}{E} = 9 \left(\frac{t}{R} \right)^{1.6} + 0.16 \left(\frac{t}{l} \right)^{1.3} \quad (39)$$

The above equations have been used to size the interstages and the skirts, while the tanks have been further analyzed due to the presence of internal pressure p and of the hydrostatic pressure p_{hydro} imposed by the propellant contained inside.

With the presence of internal pressure p , the stress in the axial direction σ_{AX} and on the hoop σ_{hoop} can be computed via Equation (40):

$$\sigma_{AX} = \frac{p \times \text{Area pressed}}{A}(SF) = \frac{p \pi R^2}{2\pi R t}(SF) \quad \sigma_{hoop} = 2\sigma_{AX} \quad (40)$$

Furthermore, considering the hydrostatic pressure p_{hydro} of the propellant inside the tank:

$$\begin{cases} \sigma_{AX,MAX} = -|\sigma_A| - |\sigma_B| + |\sigma_{AX}| + |\sigma_{AX,hydro}| = \left[-\frac{P}{2\pi R t} - \frac{MR}{\pi R^3 t} + \frac{R}{2t} (p + \rho_{prop} n_x g_0 h_{prop}) \right] (SF) \\ \sigma_{hoop,MAX} = |\sigma_{hoop}| + |\sigma_{hoop,hydro}| = \frac{R}{t} (p + \rho_{prop} n_x g_0 h_{prop}) (SF) \end{cases} \quad (41)$$

Finally, buckling has been reconsidered when the tanks are full and pressurized. The internal pressure helps contrasting the buckling effect, since it acts in tension on the tanks surface against the buckling compression. The correlations used are reported in Equation (42):

$$\begin{cases} \sigma_{crit} = \frac{(K_0 + K_p)tE}{R} \\ K_0 = 9 \left(\frac{t}{R} \right)^{0.6} + 0.16 \left(\frac{R}{l} \right)^{1.3} \left(\frac{t}{R} \right)^{0.3} \\ K_p = 0.191 \frac{p}{E} \left(\frac{R}{t} \right)^2 \quad \text{if} \quad K_p < 0.229, \text{ otherwise} \quad K_p = 0.229 \end{cases} \quad (42)$$

J Recovery Appendix

J.1 HIAD

Heat Flux

The heat flux absorbed by the heat shield during the atmospheric re-entry phase was calculated based on a modified Chapman formula^[85] as seen below.

$$\dot{q} = 20254.4 \cdot \text{sqrt} \frac{\rho}{\rho_{ref}} \frac{R_{ref}}{R_{HS}} \cdot \left(\frac{v}{v_{ref}} \right)^{3.05} \quad (43)$$

Where R_{ref} is the reference nose radius of 1 m, ρ_{ref} is the reference air density of 1.225 kg/m³ and v_{ref} is a reference velocity of 10000 m/s.

Physical Parameters

In this section a table with all parameters used for the sizing of the HIAD system is reported.

| Name | Symbol | Value | Reference |
|---------------------------------|-------------------|------------------------|------------------------|
| HIAD Geometry | | | |
| Half-cone Angle | θ | 65° | [18], [67], [15], [16] |
| Toroid Diameter | D_{Tor} | 0.3 m | [20], [67], [15] |
| Heat Shield Diameter | D_{HS} | 1 m | [20], [15] |
| HIAD Diameter | D_{HIAD} | 3.577 m | [67] |
| AOA | α | 20° | [66] |
| Characteristic Length | L | 1 m | [67] |
| Bias Angle | β | 75° | [67] |
| Radial Strap Number | N_{RS} | 18 | [67] |
| IAD Area | A_{IAD} | 8.279 m ² | [67] |
| HIAD Material Properties | | | |
| Fibre Yield (Kevlar 49) | σ_{Fib} | 3 GPa | [67] |
| Fibre Density (Kevlar 49) | ρ_{Fib} | 1440 kg/m ³ | [67] |
| Gore Yield (Upilex-25S) | σ_{Gore} | 0.5 GPa | [67] |
| Gore Density (Upilex-25S) | ρ_{Gore} | 1470 kg/m ³ | [67] |
| Gore Strain (Upilex-25S) | ϵ_{Gore} | 0.1 | [67] |
| Gas Properties | | | |
| Molecular Mass | M_{mol} | 22 g/mol | [67] |
| Gas Temperature | T_{gas} | 273.15 K | [67] |
| Gas Constant | R | 8.3144 J/mol·K | [67] |
| Tank Properties | | | |
| Tank Yield (Aluminium) | σ_{tank} | 880 MPa | |
| Tank Density (Aluminium) | ρ_{tank} | 4500 kg/m ³ | |
| Heat Shield Properties | | | |
| Thickness (PICA) | t_{HS} | 0.05 m | [86] |
| Density (PICA) | ρ_{HS} | 280 kg/m ³ | [86] |
| Emissivity (PICA) | ϵ_{HS} | 0.85 | [86] |

| Name | Symbol | Value | Reference |
|---------------------------|---------------|---------------------|-----------|
| Area (PICA) | A_{HS} | 1.767 m^2 | [67] |
| Margins | | | |
| Inflation Pressure Margin | η_p | 1.25 | [67] |
| Gas Mass Margin | η_{gas} | 1.25 | [67] |
| Toroid Mass Margin | η_{tor} | 4 | [67] |
| Radial Strap Mass Margin | η_{RS} | 4 | [67] |
| Gore Mass Margin | η_{gore} | 4 | [67] |
| Tank Thickness Margin | SF_t | 3 | |
| Tank Pressure Margin | SF_p | 100 | |
| Tank Volume Margin | η_V | 1.1 | [87] |

Table 15: HIAD values used in the sizing

Dimensionless Formulas

In this section all the dimensionless formulas^[67] used for the sizing of the inflated aeroshell are used as seen in section 4.8.

$$\xi_i = \frac{D_i}{D_{tot}} \quad (\text{Heat Shield Diameter})$$

$$\xi_t = \frac{1 - \xi_i}{(2N - 1) \cdot \sin(\theta) + 1 - \cos(\theta)} \quad (\text{Toroid Diameter})$$

$$AR = 1 - \xi_i^2 \quad (\text{IAD Area Ratio})$$

$$\bar{C} = N \cdot [1 - \xi_t - \xi_t \cdot (N - 1) \cdot \sin(\theta)] \quad (\text{Toroid Circumference})$$

$$\bar{S} = \frac{4\pi \cdot \xi_t}{AR} \cdot \bar{C} \quad (\text{Toroid Surface})$$

$$\bar{V} = \frac{\bar{S}}{4} \quad (\text{Toroid Volume})$$

$$\bar{L}_r = \xi_t \cdot [2(N - 1) + \pi] \quad (\text{Radial Strap Length})$$

$$\bar{A}_{gore} = \frac{1}{\sin(\theta)} + \frac{2\pi \cdot \xi_t \cdot (1 - \xi_t)}{AR} \quad (\text{Gore Area})$$

$$\bar{r}_c = \frac{\pi \cdot (4\xi_{gore}^2 + 1)}{8\xi_{gore} \cdot N_{RS}} \quad (\text{Deflected Surface Curvature})$$

$$\bar{p}_{min} = \frac{AR \cdot \tan(\theta) \cdot \sin(\theta)}{3\xi_t} \cdot \eta_p \quad (\text{Inflation Pressure})$$

$$\bar{G} = \frac{g_0 \cdot L}{\frac{R}{M} \cdot T} \quad (\text{Gas Dimensionless Parameter})$$

$$\bar{m}_{gas} = \bar{G} \cdot (\bar{p}_{min} + \Delta \bar{p}_{static}) \cdot \bar{V} \cdot \xi_t \cdot \bar{D}_0 \cdot \eta_g \quad (\text{Gas Mass})$$

$$\bar{\sigma} = \frac{\sigma}{\rho \cdot g_0 \cdot L} \quad (\text{Tensile Yield})$$

$$\bar{m}_{Fib} = \frac{1}{\bar{\sigma}} \cdot \left(1 + \frac{1}{\tan^2(\beta)}\right) \cdot \bar{p}_{min} \cdot \bar{S} \cdot \frac{\xi_t}{2} \cdot \bar{D}_0 \cdot \eta_{Fib} \quad (\text{Fiber Mass})$$

$$\bar{m}_{Axial} = \frac{1}{\bar{\sigma}} \cdot \bar{p}_{min} \cdot \bar{S} \cdot \frac{\xi_t}{4} \cdot \bar{D}_0 \cdot \eta_{Axial} \quad (\text{Axial Fiber Mass})$$

$$\bar{m}_{Toroid} = \frac{1}{\bar{\sigma}} \cdot \bar{p}_{min} \cdot \bar{S} \cdot \frac{\xi_t \cdot (2 - 3\xi_t)/4\xi_i}{4} \cdot \bar{D}_0 \cdot \eta_{Tor} \quad (\text{Toroid Mass})$$

$$\bar{m}_{RS} = \frac{1}{\bar{\sigma}} \cdot \frac{\bar{L}_r}{\cos(\theta)} \cdot \bar{D}_0 \cdot \eta_{RS} \quad (\text{Radial Straps Mass})$$

$$\bar{m}_{gore} = \frac{1}{\bar{\sigma}} \cdot \bar{r}_c \cdot \bar{D}_0 \cdot \eta_{gore} \quad (\text{Gore Mass})$$

(44)

Tank Sizing

In this section the formulas used to size the tank are reported.

$$mol = m_{gas}/M_{mol} \quad (\text{Mole of the gas})$$

$$V_{gas} = \frac{mol \cdot R \cdot T}{SF_p \cdot p_{min}} \quad (\text{Gas Volume})$$

$$r_{tank} = \left(\frac{3V_{gas}}{4\pi}\right)^{1/3} \cdot \eta_V \quad (\text{Tank Radius})$$

$$t_{tank} = \frac{p_{min} \cdot r_{tank} \cdot SF_t \cdot SF_p}{2\sigma_{tank}} \quad (\text{Tank Thickness})$$

$$A_{tank} = 4\pi \cdot r_{tank}^2 \quad (\text{Tank Surface})$$

$$V_{tank} = A_{tank} \cdot r_{tank} \quad (\text{Tank Volume})$$

$$m_{tank} = \rho_{tank} \cdot V_{tank} \quad (\text{Tank Mass})$$

(45)

CAD model and system integration

Follows a simplified CAD (SOLIDWORKS) model for the evaluation of the integration in the launcher.

The CAD models of the TEREA engines has correct nozzles diameters, scaled (to real motors such as SpaceX's Merlin 1C) chamber dimensions and for the fluidics, pumps, TVC system no model at all. For this last categories only a 45° angle truncated cone connecting chamber head and engine attachment surface/point has been put into place to account for the space occupied by those systems.

For simplicity the HIAD has been kept the same for both the first and second stages recovery systems. The model has two configurations. One configuration before inflation, where the upper inflatable part is an orange part kept in place by an aluminium skirt symbolizing the eternal structure that holds the inflating part in place and allows structural support for external attachment, the other part is the main

structure that holds the gas tank and its diameter is $1m$. One inflated configuration where the aluminium skirt is lost to allow the inflation of the system, the inflated part is composed of four orange toroids of $30cm$ diameter with a 65° half angle, the thermal protection is a black layer that covers the underside (when descending). (Images of HIAD present in Figure 22)

Inflated and before inflation configuration for both stages recovery systems are here Figure 22 reported.

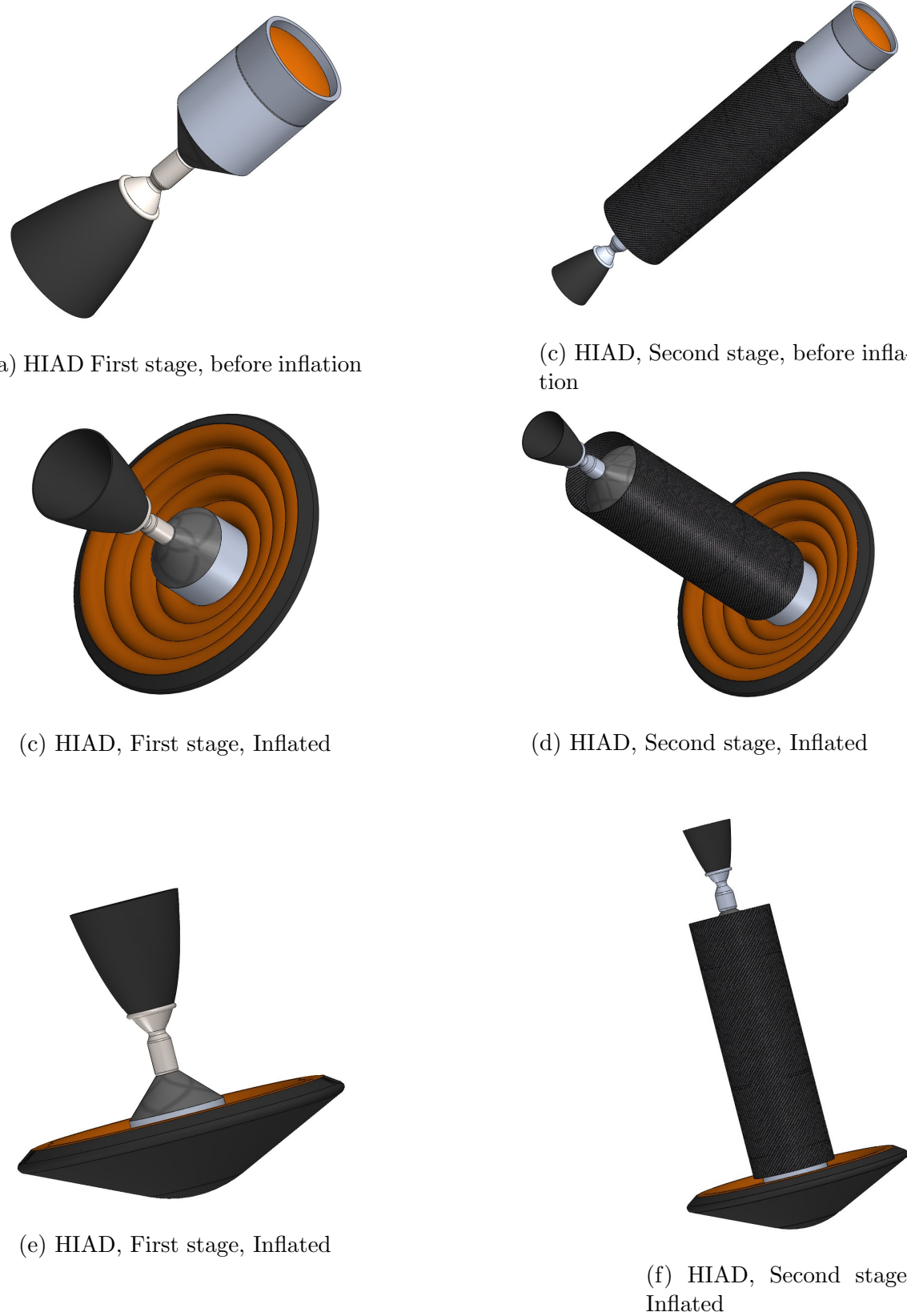


Figure 22: Stages recovery CAD models for different configurations and perspectives.
(not in scale one in respect to the other)

Cad model consistency and has been verified comparing the model to the Figures 4, 5, 8, 9, 10, 12, 13 of reference^[20].

Integration in the full launcher is presented in Figure 23. As can be seen multiple simplifications have

been adopted. For the first stage the inflating side has been put below the first stage oxidizer tank dome at an arbitrary distance to account for the lines routing around the HIAD, essential support structures are missing. For the second stage the bottom side of the HIAD has been put into contact with the dome of the fuel tank, essential support structure are also here missing; moreover the payload is here mated to the inflating side of the HIAD, in particular to the disposable skirt around the inflating part. This part in particular would have to be reworked to account for a safe, stable structure to serve as base for the payload.

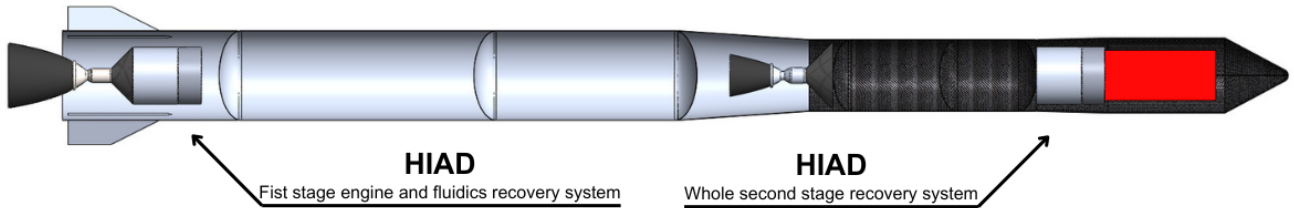


Figure 23: HIADs integrated in the launcher.

This CAD model validation exhibits some issues with the implementation in a real world scenario, in particular for the first stage engine, lines etc. recovery: the lines coming from the tanks going to the engine have to pass around the HIAD and its considerable dimensions could make this task difficult and costly; moreover the length of the first stage aft skirt had to be elongated to account for the HIAD presence and lines routing, resulting to a doubling of its length (arbitrary) and so an increase of the total launcher length.

In figure Figure 24 is presented a snapshot of the detachment phase of the first stage HIAD recovery system.



Figure 24: First stage HIAD recovery system detach.

J.2 Parachute Recovery

Physical Parameters

| Name | Symbol | Value | Reference |
|---------------------------------|-----------------|----------------------|-----------|
| Parachute Trajectory | | | |
| Drogue Opening Altitude | h_{drogue} | 8000 m | [20] |
| Parafoil Opening Altitude | h_{para} | 6500 m | [20] |
| MAR Altitude | h_{MAR} | 3000 m | [20] |
| Parafoil Opening Speed | v_{para} | 27 m/s | [20] |
| MAR Initiation Speed | v_{MAR} | 5 m/s | [20] |
| Drogue Properties | | | |
| Drogue Density (Kevlar & Nylon) | ρ_{drogue} | 675 kg/m^3 | [88] [89] |
| Drogue Drag Coefficient | C_D | 0.8 | [89] |
| Suspension Line Number | N_{SL} | 16 | [89] |

| Name | Symbol | Value | Reference |
|-----------------------------------|-----------------|-----------------------|-----------|
| Suspension Line Density | ρ_{SL} | 0.004 kg/m | [89] |
| Drogue Thickness | t_{drogue} | 0.001 m | [89] [69] |
| Drogue Shape Factor | k | 1.2 | [89] |
| Suspension Line Length | SF_{SL} | 1.2 | [89] |
| Parafoil Properties | | | |
| Parafoil Density (Kevlar & Nylon) | ρ_{drogue} | 675 kg/m ³ | [88] [89] |
| Parafoil Drag Coefficient | C_D | 1.5 | [89] |
| Aspect Ratio | AR | 2.5 | [89] [69] |
| Glide Ratio | GR | 5 | [89] [69] |
| Suspension Line Number | N_{SL} | 40 | [89] |
| Suspension Line Density | ρ_{SL} | 0.004 kg/m | [89] |
| Parafoil Thickness | t_{para} | 0.001 m | [89] [69] |

Table 16: Parachute values used in the sizing

Drogue Sizing

In this section the formulas used to size the drogue parachute as seen in Equation 4.8.

$$A_{drogue} = A_{drag} \cdot k \quad (\text{Surface Area})$$

$$m_{drogue} = A_{drogue} \cdot t_{drogue} \cdot \rho_{drogue} \quad (\text{Canopy Mass})$$

$$r_{drogue} = \sqrt{A_{drag}/\pi} \quad (\text{Drogue Radius})$$

$$L_{SL} = SF_{SL} \cdot r_{drogue} \quad (\text{Suspension Lines Length})$$

$$m_{SL} = N_{SL} \cdot L_{SL} \cdot \rho_{SL} \quad (\text{Suspension Line Mass})$$

$$m_{struct} = 0.1 \cdot (m_{drogue} + m_{SL}) \quad (\text{Structural Mass})$$

(46)

Parafoil Sizing

In this section the formulas used to size the parafoil parachute as seen in Equation 4.8.

$$A_{glide} = A_{drag} \cdot GR \quad (\text{Glide Area})$$

$$s_{para} = \sqrt{A_{glide} \cdot AR} \quad (\text{Parafoil Span})$$

$$c_{para} = s_{para}/AR \quad (\text{Parafoil Chord})$$

$$m_{para} = A_{glide} \cdot t_{para} \cdot \rho_{para} \quad (\text{Canopy Mass})$$

$$m_{SL} = N_{SL} \cdot s_{para} \cdot \rho_{SL} \quad (\text{Suspension Line Mass})$$

$$m_{struct} = 0.1 \cdot (m_{para} + m_{SL}) \quad (\text{Structural Mass})$$

J.3 Results

In this section the recovery results are explored and better analysed.

Acceleration

The accelerations impressed to the HIAD shield during the atmospheric re-entry are shown below. The values are similar to data from previous experiments^{[20][17]}. It has to be noted the the acceleration impressed on the first stage is much larger with respect to the second stage as the entry velocity is much larger, although for the most part in the horizontal direction.

Heat Flux

The heat fluxes absorbed during the atmospheric re-entry are shown below. The values are consistent with data from previous experiments and the ablative material of the heat shield has been proven to resist to such heat fluxes^{[20][17]}. It has to be noted the the heat flux absorbed by the second stage is much larger with respect to the first stage as the entry velocity is much larger, although for the most part in the horizontal direction.

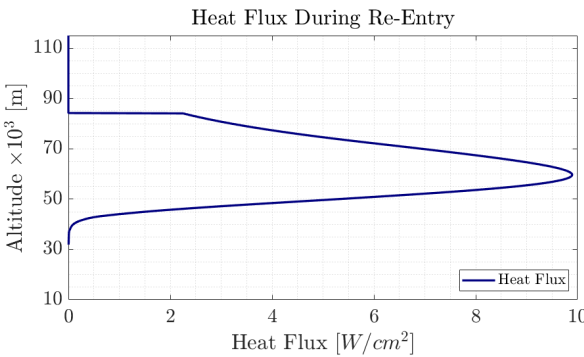


Figure 25: Heat flux absorbed by the first stage

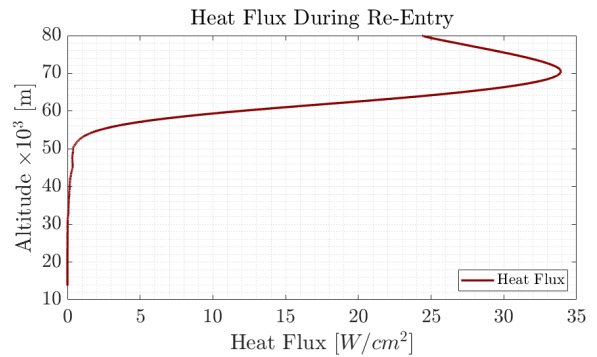


Figure 26: Heat flux absorbed by the second stage

Speed

The speed with respect to time of the first and second stage can be seen below.

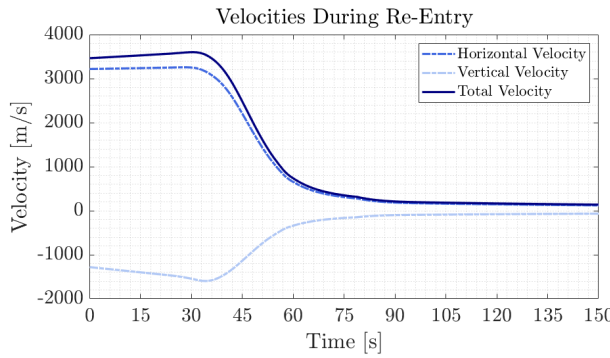


Figure 27: Speed in time of the first stage

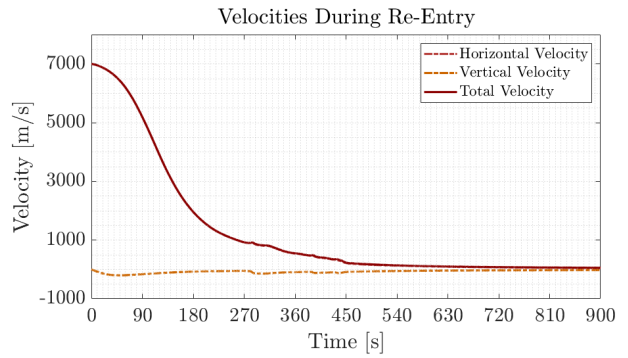


Figure 28: Speed in time of the second stage

Altitude

The altitude with respect to time of the first and second stage can be seen below.

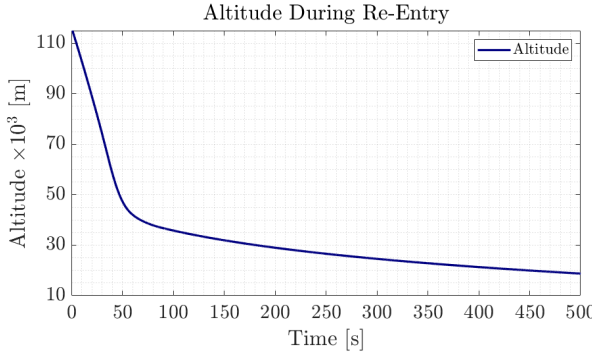


Figure 29: Altitude in time of the first stage

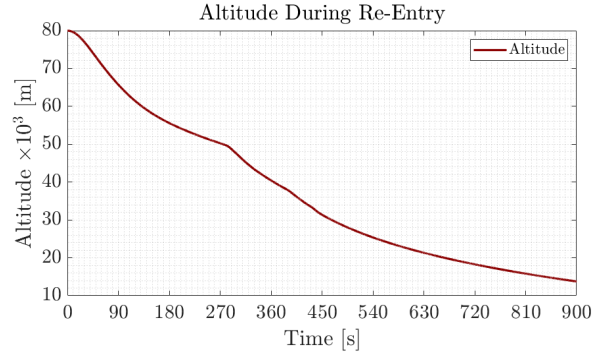


Figure 30: Altitude in time of the second stage

K Validation of subsystems Appendix

Here are reported all the validations performed on the models developed in the single subsystems.

K.1 Propulsion system

The validation of propulsion block has been performed considering the Merlin 1C engine used by Falcon 1 and Falcon 9 launch vehicles. Merlin 1C is a RP1-LOX pump-feed engine, which generates a thrust similar to the engine designed by the authors. In Table 17 are reported the engine specifications used as input for validation of propulsion block. In Table 18 are compared the I_{sp} and geometric shape calculated with the code implemented and the one retrieved from data-sheet.

| MERLIN 1C Specifications | |
|--------------------------|--------|
| P_c [bar] | 56.88 |
| $T(@s.l.)$ [kN] | 348.74 |
| O/F Ratio[–] | 5.5 |
| z_{opt} [km] | 1 |

Table 17: Merlin 1C Data^{[3][4]}

| | Real Data | Model Results |
|----------------------|-----------|---------------|
| ε | 14.5 | 13.89 |
| I_{sp} (@s.l.) [s] | 274 | 273.07 |
| I_{sp} (@vac) [s] | 304 | 306 |

Table 18: Validation of propulsion block

K.2 Estimation of masses and dimensions

To validate the results obtained from the estimations (both masses and lengths), a search for a compatible launcher has been done. The difficulties encountered in this part are mainly related to two aspects: first, airborne launchers can be considered a niche, and their user manuals do not provide enough information to run our code without a huge amount of assumptions; second, the totality of user manuals found that provide enough information are those of classic ground-launched rockets. Our choice was to validate our results (codes and corrective factors) with SpaceX's Falcon 1^[80], that has a user manual with almost all the information needed to reduce the amount of assumptions. Our developed code has been run with Falcon 1's data, and the following errors have been found on the dry mass and on the total length:

- Dry mass, first stage: -4.2% error
- Dry mass, second stage: -11.6% error
- Total length: -4.4% error

We concluded that the estimation process provides realistic results.

L KPI Appendix

In this section, a more detailed description of the methodology adopted to compute the Key Performance Indexes is reported.

Profitability KPI

The profitability KPI is computed by evaluating the cost structure, revenue, and operational expenses of each configuration. The calculation involves the following steps:

- Turnaround Time:** Each configuration is assigned a turnaround time ($t_{turnAround}$) in days, ranging from 60 to 100 days, depending on the materials and propellant used. This parameter determines the launch frequency:

$$f_{\text{launch}} = 365/t_{\text{turnAround}} \quad (48)$$

- . In Table 19, the turnaround time for each configuration is showcased.

| Configuration ID | Turnaround Time (days) |
|------------------|------------------------|
| 1, 3, 4, 6 | 90 |
| 2, 5 | 100 |
| 7, 9, 10, 12 | 60 |
| 8, 11 | 75 |

Table 19: Turnaround times for different configurations.

- Development and Production Costs:** The initial cost (CI) is the sum of:

- Development cost, including structure, propellant, and engine costs, with engine costs estimated as [73].

$$C_{\text{engine}_1} = 18.9M_{\text{dry}}^{0.959}T_{\text{vac}}^{0.412}\dot{m}^{-0.383} \quad C_{\text{engine}_2} = 27M_{\text{dry}}^{1.714}T_{\text{vac}}^{0.423}\dot{m}^{-1.301} \quad (49)$$

- R&D cost, estimated as 25% of the development cost.
- Production cost, approximated at \$45,000 per pound to orbit.

$$CI = \text{DevCost} + \text{ProdCost} \quad (50)$$

where:

$$\text{DevCost} = C_{\text{engine}_1} + C_{\text{engine}_2} + (M_{\text{struct1}} \cdot P_{\text{mat1}}) + (M_{\text{struct2}} \cdot P_{\text{mat2}}) + (M_{\text{fairing}} \cdot P_{\text{fair}}) + R\&D \quad (51)$$

$$\text{ProdCost} = 45000 \cdot M_{pl} \quad (52)$$

| Material/Propellant | LOX | RP1 | LH2 | LCH4 | Carbon Composite | Aluminum Alloy | Fairing Honeycomb |
|---------------------|------|------|-------|------|------------------|----------------|-------------------|
| Price per kg (\$) | 0.31 | 4.76 | 10.65 | 0.40 | 85 | 15 | 200 |
| Reference | [53] | [53] | [53] | [53] | [90] | [90] | - |

Table 20: Prices per kg of various materials and propellants.

- Operational Costs:** The per-launch operational cost (C_{op}) includes:

- Helicopter rental (\$7,000 per hour, 24 hours of rental).
- Aircraft amortization over 15 years (\$15M initial cost [91] [92] [93]) and associated maintenance/fuel costs (\$350k per launch).
- Refurbishment and expendable material costs with an additional 20% margin for reusability-related expenses.

$$NP_{\text{launch}} = R_{\text{launch}} - C_{\text{op}} \quad (53)$$

Where:

$$C_{\text{op}} = C_{\text{heli}} + C_{\text{aircraft}} + 1.2 \cdot (M_{\text{struct1}} \cdot P_{\text{mat1}} + M_{\text{fairing}} \cdot P_{\text{fair}} + M_{\text{fuel}} \cdot P_{\text{fuel}} + M_{\text{ox}} \cdot P_{\text{ox}}) \quad (54)$$

4. Revenue and Net Profit: The revenue per launch is calculated as:

$$R_{\text{launch}} = \text{max payload capacity} \times \$15,000/\text{kg}$$

The net profit per launch (NP_{launch}) is the difference between revenue and operational costs. Maximum payload capacity is computed for a reference LEO orbit at 350 km by determining the payload mass that satisfies the total Δv budget. The Δv budget includes the orbital velocity, gravity losses (13% of v_{req}), site losses due to Earth's rotation, and the aircraft velocity provided at launch. The total velocity is matched to the rocket's Δv , computed from the stage-specific impulses and mass ratios. The payload is calculated iteratively by solving the equation:

$$\Delta v_{\text{budget}} = I_{\text{sp},1}g_0 \ln \left(\frac{M_{01} + M_{\text{pay}}}{M_{f1} + M_{\text{pay}}} \right) + I_{\text{sp},2}g_0 \ln \left(\frac{M_{02} + M_{\text{pay}}}{M_{f2} + M_{\text{pay}}} \right)$$

where M_{01} , M_{02} , M_{f1} , and M_{f2} represent the initial and final masses of each stage.

Finally, the overall metrics to be computed are:

- Break-even point (N_{bep}): Number of launches required to recover CI , computed as:

$$N_{\text{bep}} = \frac{CI}{NP_{\text{launch}}}$$

- Time to profit: Calculated as $TTP = N_{\text{bep}} / f_{\text{launch}}$.
- Total net profit after 8 launches (TNP): Total profit from 8 launches, considering payload capacity and operational costs.

This methodology ensures that all configurations are evaluated consistently, capturing the trade-offs between initial costs, reusability, and operational performance.

Reusability KPI

The reusability KPI is calculated by evaluating two primary factors: the recovery system mass fraction and the reentry burn mass fraction.

1. The recovery system mass fraction (R_{r1} and R_{r2}) is determined by comparing the mass of the recovery systems to the mass of the recovered components. Specifically, R_{r1} is the ratio of the first stage recovery system mass to the engine mass, and R_{r2} is the ratio of the second stage recovery system mass to the second stage mass. The formulas used are:

$$R_{r1} = \frac{M_{\text{recovery}}(1)}{M_{\text{engine}}} \quad \text{and} \quad R_{r2} = \frac{M_{\text{recovery}}(2)}{M_{\text{Stage2}}}$$

where $M_{\text{recovery}}(1)$ and $M_{\text{recovery}}(2)$ are the masses of the recovery systems for the first and second stages, respectively, and M_{engine} and M_{Stage2} represent the mass of the engine and the second stage, respectively.

2. The reentry burn mass fraction (R_{prop}) is calculated by dividing the mass of the propellant used for the reentry burn by the total mass of propellant. The formula is:

$$R_{\text{prop}} = \frac{M_{\text{propRentry}}}{M_{p2}}$$

where $M_{\text{propRentry}}$ is the mass of propellant required for the reentry burn, and M_{p2} is the total mass of propellant of the second stage.

A lower recovery system mass fraction and reentry burn mass fraction are preferred as they indicate a more efficient design, preserving more mass for payload delivery. The overall reusability KPI combines these factors to assess the efficiency of the vehicle's recovery and reusability systems.

Time to Market KPI

| Configuration | Fuel Type | Material | Time to Market KPI |
|---------------|-------------|-----------------------|--------------------|
| ID 1 | RP1 / RP1 | Composite / Composite | 1.00 |
| ID 2 | RP1 / LH2 | Composite / Composite | 0.50 |
| ID 3 | RP1 / LCH4 | Composite / Composite | 0.40 |
| ID 4 | LCH4 / RP1 | Composite / Composite | 0.70 |
| ID 5 | LCH4 / LH2 | Composite / Composite | 0.40 |
| ID 6 | LCH4 / LCH4 | Composite / Composite | 0.30 |
| ID 7 | RP1 / RP1 | Aluminum / Composite | 0.80 |
| ID 8 | RP1 / LH2 | Aluminum / Composite | 0.60 |
| ID 9 | RP1 / LCH4 | Aluminum / Composite | 0.50 |
| ID 10 | LCH4 / RP1 | Aluminum / Composite | 0.70 |
| ID 11 | LCH4 / LH2 | Aluminum / Composite | 0.50 |
| ID 12 | LCH4 / LCH4 | Aluminum / Composite | 0.40 |

Table 21: Time to Market KPI for different configurations based on fuel and material combinations.

Design Inefficiencies KPI

The Design Inefficiencies KPI evaluates how close a configuration is to optimal design targets by considering three factors: the propellant mass ratio ($M_{\text{propRatio}}$), the fairing filling factor (V_{filling}), and the structural efficiency (ε) of both stages.

The KPI is calculated using:

$$KPI_{\text{design}} = \frac{w_1 \frac{1}{M_{\text{propRatio}}} + w_2 (1 - |V_{\text{filling}} - 0.8|) - w_3 \left(\alpha \frac{\varepsilon_1}{\varepsilon_{\max 1}} + (1 - \alpha) \frac{\varepsilon_2}{\varepsilon_{\max 2}} \right) + C}{\sum w + C}$$

where:

- $M_{\text{propRatio}}$ should ideally be 1.
- V_{filling} targets 0.8 for optimal fairing usage.
- ε_1 and ε_2 are the structural efficiencies for the stages, with lower values indicating better designs.

This KPI penalizes configurations with inefficient designs, promoting better optimization across all factors.

Emissions KPI

[75]

Table 3 – Overview over the exhaust composition of the five propellants. Results are given in kg per kg propellant combusted.

| Propellant | CO | CO ₂ | H ₂ O | H | O | OH | N ₂ | NO | Al | HCl | Cl | BC |
|----------------------|-------|-----------------|------------------|-------|-------|-------|----------------|-------|-------|-------|-------|-------|
| LOx&RP-1 | 0.456 | 0.222 | 0.250 | 0.012 | 0.011 | 0.029 | 0 | 0 | 0 | 0 | 0 | 0.020 |
| LOx&LH ₂ | 0 | 0 | 0.907 | 0.064 | 0.002 | 0.027 | 0 | 0 | 0 | 0 | 0 | 0.000 |
| LOx&LCH ₄ | 0.344 | 0.187 | 0.422 | 0.018 | 0.005 | 0.024 | 0 | 0 | 0 | 0 | 0 | 0 |
| NTO&UDMH | 0.227 | 0.114 | 0.258 | 0.013 | 0.006 | 0.020 | 0.353 | 0.005 | 0 | 0 | 0 | 0.004 |
| APCP | 0.280 | 0.017 | 0.067 | 0.026 | 0.001 | 0.009 | 0.081 | 0.001 | 0.342 | 0.148 | 0.025 | 0.004 |

Figure 31: Table of emissions for different propellant couples

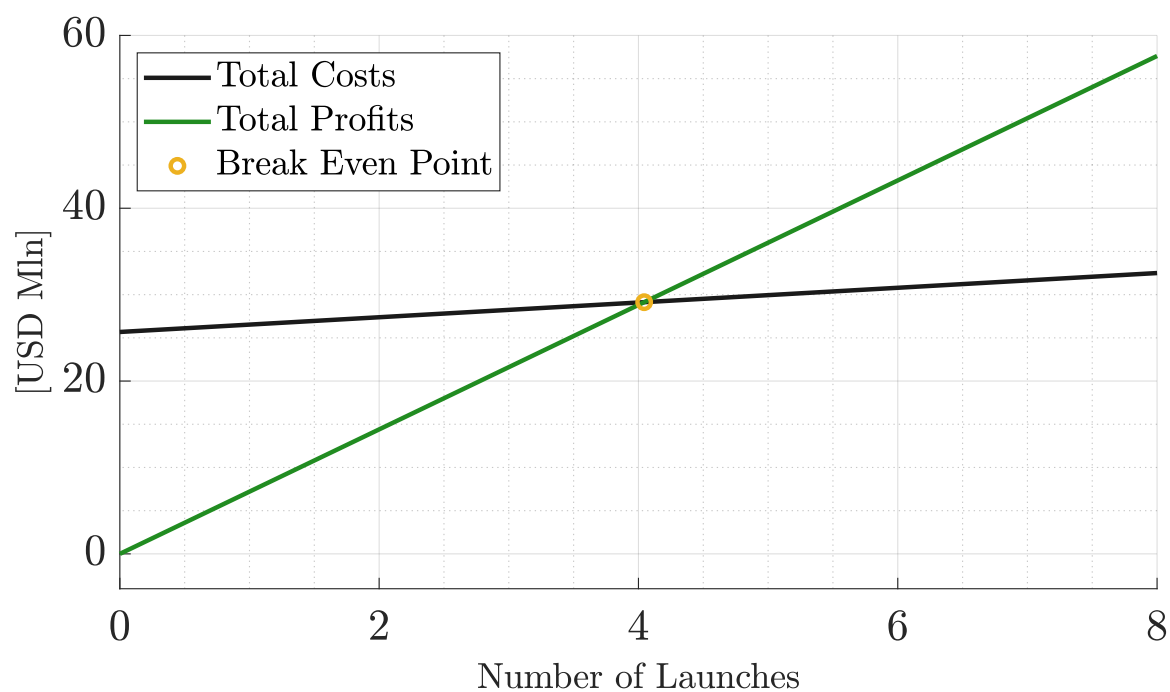


Figure 32: Break Even Point

Bibliography

- [1] Cole, H. A. and Erickson, A. L. and Rainey, A. G., "Buffeting during atmospheric ascent," National Aeronautics and Space Administration, Tech. Rep. NASA-SP-8001(REV), November 1970, revision Report.
- [2] Boeing, "747-400 freighter," https://www.boeing.com/content/dam/boeing/boeingdotcom/company/about_bca/startup/pdf/freighters/747-400f.pdf.
- [3] Brian Bjelde and Peter Capozzoli and Gwynne Shotwell, "The SpaceX Falcon 1 Launch Vehicle Flight 3 Results, Future Developments, and Falcon 9 Evolution," in *Proceedings of the 59th International Astronautical Congress (IAC)*, ser. IAC-08-D2.1.03, International Astronautical Federation (IAF). Glasgow, Scotland: International Astronautical Federation, 2008, Space Exploration Technologies, United States of America.
- [4] S. E. Corporation, "Falcon 1 launch vehicle payload user's guide." [Online]. Available: <http://www.spacelaunchreport.com/falcon.html>
- [5] W. contributors, "Air-Launch to Orbit," <https://en.wikipedia.org/wiki/Air-launch-to-orbit>.
- [6] Kelly, J. W. and Rogers, C. E. and Brierly, G. T. and Martin, J. C. and Murphy, M. G., "Motivation for Air-Launch: Past, Present, and Future," Edwards, California, 93523.
- [7] S. A. Muir, "Air-Launch to Orbit," Boulder, CO 80909.
- [8] Northrop Grumman Corporation, "Pegasus Payload user's guide - Release 8.2," 2020.
- [9] Virgin Orbit, LLC, "LauncherOne service guide - Version 2.1," 2020.
- [10] J. Foust, "Death of a Launch Company," *The Space Review*, May 30, 2023. [Online]. Available: <https://www.thespacereview.com/article/4593/1>
- [11] Goetzendorf-Grabowski, T. and Kiszkowiak, L. and Kwiek, A. and Zalewski, P. and Chudy, K. and Figat, M., "Study on Configurations of Airborne Launch System for Delivery of Small Payload to Low Earth Orbit." [Online]. Available: https://www.icas.org/ICAS_ARCHIVE/ICAS2024/data/papers/ICAS2024_0355_paper.pdf
- [12] Sarigul-Klijn, N. and Sarigul-Klijn, M., "A Comparative Analysis of Methods for Air-Launching Vehicles from Earth to Sub-Orbit or Orbit," *Proceedings of the Institution of Mechanical Engineers, Part G: Journal of Aerospace Engineering*, pp. 439–452, October 2006.
- [13] R. Dillman, "Attitude Control Performance of IRVE-3," 2013. [Online]. Available: <https://core.ac.uk/download/pdf/42731591.pdf>
- [14] ——, "Flight Performance of the Inflatable Re-entry Vehicle Experiment 3 , " 2013. [Online]. Available: <https://ntrs.nasa.gov/api/citations/20140000147/downloads/20140000147.pdf>
- [15] ——, "Inflatable Reentry Vehicle Experiment-3 (IRVE-3) Project Overview & Instrumentation," 2015. [Online]. Available: <https://core.ac.uk/download/pdf/80604887.pdf>
- [16] A. Mazaheri, "High-Energy Atmospheric Reentry Test Aerothermodynamic Analysis," 2013. [Online]. Available: <https://ntrs.nasa.gov/api/citations/20140000739/downloads/20140000739.pdf>
- [17] H. Wright, "HEART Flight Test Overview," 2012. [Online]. Available: https://websites.isae-supraero.fr/IMG/pdf/137-heart-ippw-9_v04-tpsas.pdf
- [18] Mohamed M. Ragab, F. McNeil Cheatwood and Stephen J. Hughes , "Launch Vehicle Recovery and Reuse," 2015. [Online]. Available: [https://www.ulalaunch.com/docs/default-source/supporting-technologies/launch-vehicle-recovery-and-reuse-\(aiaa-space-2015\).pdf](https://www.ulalaunch.com/docs/default-source/supporting-technologies/launch-vehicle-recovery-and-reuse-(aiaa-space-2015).pdf)

- [19] Mohamed M. Ragab, F. McNeil Cheatwood, Stephen J. Hughes and Robert Dillman, “HIAD on ULA (HULA) Orbital Reentry Flight Experiment Concept,” 2016. [Online]. Available: <https://ntrs.nasa.gov/api/citations/20160010175/downloads/20160010175.pdf>
- [20] Mohamed M. Ragab, F. McNeil Cheatwood, Stephen J. Hughes, “Performance Efficient Launch Vehicle Recovery and Reuse,” 2016. [Online]. Available: <https://ntrs.nasa.gov/api/citations/20160012009/downloads/20160012009.pdf>
- [21] Martins, Joaquim R. R. A. and Lambe, Andrew B., “Multidisciplinary design optimization: A survey of architectures,” *AIAA Journal*, vol. 51, no. 9, pp. 2049–2075, 2013.
- [22] M. Balesdent, “Multidisciplinary Design Optimization of Launch Vehicles,” Theses, Ecole Centrale de Nantes (ECN), Nov. 2011. [Online]. Available: <https://theses.hal.science/tel-00659362>
- [23] Balesdent, Mathieu and Bérend, Nicolas and Dépincé, Philippe and Chriette, Abdelhamid, “A survey of multidisciplinary design optimization methods in launch vehicle design,” *Structural and Multidisciplinary Optimization*, vol. 45, pp. 619–642, 05 2012.
- [24] Nicolas Duranté and Alain Dufour and Véronique Pain and Gilles Baudrillard and Marc Schoenauer, *Multi-disciplinary Analysis and Optimisation Approach for the Design of Expendable Launchers*. [Online]. Available: <https://arc.aiaa.org/doi/abs/10.2514/6.2004-4441>
- [25] F. Castellini, “Multidisciplinary design optimization for expendable launch vehicles,” Ph.D. Thesis, Politecnico di Milano, 2012.
- [26] Lewis, Robert and Shubin, Gregory and Cramer, Evin and Dennis, J. and Frank, Paul and Michael, Robert and Gregory, Lewis and Shubin, R., “Problem formulation for multidisciplinary optimization,” *SIAM Journal on Optimization*, vol. 4, 02 1997.
- [27] Chen, Gang and Xu, Min and Wan, zi-ming and Chen, Silu, “Multidisciplinary design optimization of rlv reentry trajectory,” vol. 27, 05 2005.
- [28] Martins, Joaquim and Marriage, Christopher and Tedford, Nathan, “pymdo: An object-oriented framework for multidisciplinary design optimization.” *ACM Trans. Math. Softw.*, vol. 36, 01 2009.
- [29] Balling, R. and Sobiesczanski-Sobieski, J., “Optimization of coupled systems: A critical overview of approaches,” NASA / ICASE, Technical Report 94-100, 1994.
- [30] Balling, R. and Wilkinson, C., “Execution of multidisciplinary design optimization approaches on common test problems,” *AIAA Journal*, vol. 35, no. 1, pp. 178–186, 1997.
- [31] R. Braun, “Collaborative optimization: An architecture for large-scale distributed design,” Ph.D. dissertation, Stanford University, USA, 1996.
- [32] DeMiguel, V. and Murray, W., “An analysis of collaborative optimization methods,” in *8th AIAA/USAF/NASA/ISSMO Symposium on Multidisciplinary Analysis and Optimization*, Long Beach, CA, USA, 2000.
- [33] J. Sobiesczanski-Sobieski, “Optimization by decomposition: A step from hierachic to non-hierachic systems,” NASA, Tech. Rep. CP-3031, 1988.
- [34] Nocedal, J. and Wright, S., *Numerical Optimization*, 2nd ed. Springer-Verlag, 2006.
- [35] J. Holland, *Adaptation in Natural and Artificial Systems*. Ann Arbor, USA: The University of Michigan Press, 1975.
- [36] T. Hidaka and Y. Kawada and N. Noda and T. Fujita and Y. Matsumura, “Outline of 500kg-class small satellite system study,” Tsukuba Space Center, Tsukuba-City, Ibaraki, Japan, 1990.

- [37] Onel, Alexandru-Iulian and Afilipoae, Tudorel and Neculaescu, Ana and Pricop, Mihai, “Drag coefficient modelling in the context of small launcher optimisation,” *INCAS BULLETIN*, vol. 10, pp. 103–116, 12 2018.
- [38] Curtis, Howard D., *Orbital Mechanics for Engineering Students*, 4th ed. Elsevier, 2021.
- [39] A. R. A. Rebelo, “Preliminary design of a micro launch vehicle,” 2018.
- [40] “Carbon Composites.” [Online]. Available: <https://energy.ornl.gov/CFCrush/materials/uou/8552.eu.pdf>
- [41] Rocket Lab USA, Inc., “Electron Payload User Guide - Version 7.0,” 2022.
- [42] Northrop Grumman Corporation, “Antares user’s guide,” 2020.
- [43] Space Exploration Technologies Corp., “Falcon user’s guide,” 2021.
- [44] “Delta IV user’s guide,” 2013.
- [45] ArianeSpace, “Ariane V user’s manual,” 2016.
- [46] ——, “Ariane 6 user’s manual,” 2018.
- [47] U. L. Alliance, “Atlas V Launch Services user’s guide,” 2010.
- [48] “H-IIA user’s manual,” 2015.
- [49] “Starship users guide,” 2020.
- [50] “Vulcan Launch systems user’s guide,” 2023.
- [51] Tudorel-Petronel Afilipoae and Ana-Maria Neculăescu and Alexandru-Iulian Onel and Mihai-Victor Pricop and Alexandru Marin and Alexandru-Gabriel Persinaru and Alexandru-Mihai Cișmilianu and Camelia-Elena Munteanu and Adrian Toader and Adriana Sirbi and Samir Bennani and Teodor-Viorel Chelaru, “Launch vehicle - mdo in the development of a microlauncher,” *Transportation Research Procedia*, vol. 29, pp. 1–11, 2018, aerospace Europe CEAS 2017 Conference. [Online]. Available: <https://www.sciencedirect.com/science/article/pii/S2352146518300012>
- [52] G. P. Sutton and O. Biblarz, “Rocket Propulsion Elements,” 2017.
- [53] Edberg, D. and Costa, W., “Design of Rockets and Space Launch Vehicles,” Reston, Virginia, 2022.
- [54] L. H. Jorgensen, “Prediction of static aerodynamic characteristics for space-shuttle-like and other bodies at angles of attack from 0° to 180°,” 1973.
- [55] E. L. Fleeman, “Tactical Missile Design.”
- [56] L. S. Jernell, “Aerodynamic characteristics of bodies of revolution at Mach numbers from 1.50 to 2.86 and angles of attack to 180°,” 1968.
- [57] E.L. Houghton and P.W. Carpenter, “Aerodynamics for engineering students,” 2003.
- [58] M.N. Rhode and W.C. Engelund and M.R. Mendenhall, “Experimental aerodynamic characteristics of the Pegasus air-launched booster and comparison with predicted and flight results,” 1995.
- [59] D. Pilori, “Multidisciplinary approach of small air launched rocket preliminary design,” 2020.
- [60] Md. Amzad Hossain, Austin Morse, Iram Hernandez, Joel Quintana and Ahsan Choudhuri, “Liquid Rocket Engine Performance Characterization Using Computational Modeling: Preliminary Analysis and Validation.” [Online]. Available: <https://doi.org/10.3390/aerospace11100824>

- [61] Rick Newlands, Martin Heywood and Andy Lee, “Rocket vehicle loads and airframe design.” [Online]. Available: <http://www.aspirespace.org.uk/downloads/Rocket%20vehicle%20loads%20and%20airframe%20design.pdf>
- [62] United Launch Alliance, “Atlas v cutaway,” 2024. [Online]. Available: <https://www.ulalaunch.com/docs/default-source/rockets/atlasv-cutaway.pdf>
- [63] European Space Agency, “Ariane 5 fairing,” 2024. [Online]. Available: https://www.esa.int/Enabling_Support/Space_Transportation/Launch_vehicles/Ariane_5_fairing
- [64] Jianfeng Wang and Chengyang Shi and Na Yang and Haonan Sun and Yiqun Liu and Baoyu Song, “Strength, stiffness, and panel peeling strength of carbon fiber-reinforced composite sandwich structures with aluminum honeycomb cores for vehicle body,” *Composite Structures*, vol. 184, pp. 1189–1196, 2018. [Online]. Available: <https://www.sciencedirect.com/science/article/pii/S0263822317316264>
- [65] C. Dek, J.-L. Overkamp, A. Toeter, and T. Hoppenbrouwer, “A recovery system for the key components of the first stage of a heavy launch vehicle,” *Aerospace Science and Technology*, vol. 100, p. 105778, 2020. [Online]. Available: <https://www.sciencedirect.com/science/article/pii/S1270963819326458>
- [66] Karen L. Bibb, Stephen J. Alter and Ryan McDaniel, “Aerodynamic Analysis of Simulated Heat Shield Recession for the Orion Command Module,” 46th AIAA Aerosciences Meeting and Exhibit, Tech. Rep., January 2008. [Online]. Available: <https://ntrs.nasa.gov/api/citations/20080008345/downloads/20080008345.pdf>
- [67] J. A. Samareh, “Estimating Mass of Inflatable Aerodynamic Decelerators Using Dimensionless Parameters.” [Online]. Available: <https://ntrs.nasa.gov/api/citations/20110014351/downloads/20110014351.pdf>
- [68] A.M. Dwyer Cianciolo, J.L. Davis, D.R. Komar and J.A. Samareh, “Entry, Descent and Landing Systems Analysis Study: Phase 1 Report ,” July 2010. [Online]. Available: <https://ntrs.nasa.gov/api/citations/20110014351/downloads/20110014351.pdf>
- [69] J.C. Berland, J. Barber and B. Gargano, “Autonomous Precision Delivery of 42,000 Pounds (19,000 kg) Under One Parachute ,” May 2009. [Online]. Available: <https://ntrs.nasa.gov/api/citations/20110014351/downloads/20110014351.pdf>
- [70] L. Martin, “Sikorsky S-92.” [Online]. Available: <https://www.lockheedmartin.com/en-us/products/sikorsky-s-92-helicopter.html>
- [71] Marcello Spagnulo and Mauro Balduccini and Federico Nasini, *Elementi di management dei programmi spaziali*. Berlin: Springer Verlag, 2011.
- [72] Stappert, Sven and Wilken, Jascha and Dominguez Calabuig, Guillermo J. and Sippel, Martin, “Evaluation of parametric cost estimation in the preliminary design phase of reusable launch vehicles,” 07 2022.
- [73] John S. Nieroski and Edward I. Friedland, “Liquid rocket engine cost estimation relationships,” in *AIAA Second Annual Meeting*, no. 65-553. San Francisco, California: Aerospace Corporation, Jul. 1965, aIAA Paper No. 65-553.
- [74] I. Billi, “Preliminary discussion cost per rlv,” 2021, supervisor: Matteo Filippi, Erasmo Carrera, Alfonso Pagani.
- [75] P. E. Schabedoth, “Life cycle assessment of rocket launches and the effects of the propellant choice on their environmental performance,” Available at NTNU’s digital repository, 2020, advisors: Johan Berg Pettersen and Noora Partamies. [Online]. Available: <https://hdl.handle.net/11250/2779647>

- [76] J. Blanco Camargo, "Literature review of the environmental impact on the atmosphere of rocket engine emissions during launch, flight and re-entry," Available online, 2020, accessed: 2021-09-20. [Online]. Available: <http://hdl.handle.net/11371/6151>
- [77] F. Mastroddi and S. Gemma, "Analysis of Pareto frontiers for multidisciplinary design optimization of aircraft."
- [78] Franco Mastroddi and Stefania Gemma, "Multi and Single objective Multidisciplinary Optimization for the preliminary design of aircrafts."
- [79] Pempie, Pascal and Gorecki, Hervé, "A-01v high thrust lox-ch4 engine high thrust lox-ch4 engine," 05 2000.
- [80] "Falcon 1 Launch Vehicle Payload User's Guide Rev. 7," SpaceX. [Online]. Available: <http://www.georing.biz/usefull/Falcon1UsersGuide.pdf>
- [81] Harvey A. Wallskog, Roger G. Hart, "Investigation of the drag of blunt-nosed bodies of revolution in free flight at mach numbers from 0.6 to 2.3," NACA, 1953.
- [82] William C. Pitts and Jack N. Nielsen and George E. Kaattari, "Lift and center of pressure of wing-body-tail combinations at subsonic, transonic, and supersonic speeds," 1959.
- [83] F. Teren, "Explicit Guidance Equations For Multistage Boost Trajectories."
- [84] P. M. Sforza, *Manned Spacecraft Design Principles*. Elsevier, 2016.
- [85] Jascha Wilken and Sven Stappert, "Comparative analysis of European vertical landing reusable frst stage concepts," 2024. [Online]. Available: https://www.researchgate.net/publication/379907711_Comparative_analysis_of_European_vertical_landing_reusable_first_stage_concepts
- [86] J. Thornton, W. Fan, E. Ghandehari, M. Stackpoole and J. Chavez-Garcia, "PICA Variants With Improved Mechanical Properties," 2010. [Online]. Available: <https://ntrs.nasa.gov/api/citations/20110014590/downloads/20110014590.pdf>
- [87] ESA. (2012) Margin philosophy for science assessment studies. [Online]. Available: https://sci.esa.int/documents/34375/36249/1567260131067-Margin_philosophy_for_science_assessment_studies_1.3.pdf
- [88] B. P. Anderson and J. Daum, "Textile Material Lessons Learned During the Design and Qualification of the NASA Orion Capsule Parachute Assembly System," 2019. [Online]. Available: <https://ntrs.nasa.gov/api/citations/20190026519/downloads/20190026519.pdf>
- [89] I. I. of Technology, "Parachute Deceleration System Design and Testing." [Online]. Available: https://idr-lib.iitbhu.ac.in/xmlui/bitstream/handle/123456789/2580/09_Chapter%2005.pdf?sequence=9&isAllowed=y
- [90] Shama Rao, N. and Simha, T. G. A. and Rao, K. P. and Ravi Kumar, G. V. V., "Carbon composites are becoming competitive and cost effective," 2020.
- [91] S. Flying, "Boeing 747 operating costs guide," 2024, accessed: 2024-12-11. [Online]. Available: <https://simpleflying.com/boeing-747-operating-costs-guide/#:~:text=A%20newer%20747%2D8%20costs,as%20little%20as%20%2410%20million>
- [92] U. Magazine, "Stratolaunch officially buys virgin orbit's cosmic girl carrier aircraft," 2024, accessed: 2024-12-11. [Online]. Available: <https://universemagazine.com/en/stratolaunch-officially-buys-virgin-orbits-cosmic-girl-carrier-aircraft/>
- [93] N. Atlas, "Virgin galactic's launcherone and cosmic girl," 2024, accessed: 2024-12-11. [Online]. Available: <https://newatlas.com/virgin-galactic-launcherone-cosmic-girl/40744/>

M Authorship Declaration

Bellini Davide: Requirements; Genetic algorithm; Fairing design; House of Quality.

Frassinella Luca: MDO design; structural sizing; KPI definition; Baseline.

Mensi Weingrill Edoardo: Propulsion subsystem; Airborne launchers state of the art; Fairing design; Scenario definition.

Separovic Tomislav Marko: Trajectory and simulation; Loads and FEM analysis; Montecarlo simulation.

Nuccio Gabriele: MDO design; Baseline; Loads; Stability; Pareto definition.

De Marco Mattia: Preliminary masses and dimensions estimation; Centres of mass computations; Integration of structural masses for second iteration.

Modelli Simone: Propulsion subsystem; CAD.

Massini Alessandro: State of the art MDO; MDO design; Loads; KPI definition.

Juvara Matteo Giovanni: Recovery subsystem; Recovery state of the art; Requirements.

Mirri Pietro: Aerodynamics subsystem.